The Säm fold structure: characterization of folding and metamorphism in a part of the eclogite-granulite region, Sveconorwegian orogen

Stephen P. Michalchuk

**Dissertations in Geology at Lund University,
Master's thesis, no 367
(45 hp/ECTS credits)**

**Department of Geology
Lund University**
2013

The Säm fold structure: characterization of folding and metamorphism in a part of the eclogite – granulite region, Sveconorwegian orogen

Master's thesis

Stephen P. Michalchuk

Department of Geology
Lund University
2013

Contents

Cover Picture: Sunset over the Kattegatt at Träslövsläge, Hallands län, Sverige

The Säm fold structure: characterization of folding and metamorphism in a part of the eclogite – granulite region, Sveconorwegian orogen

STEPHEN PAUL MICHALCHUK

Michalchuk, S.P., 2013: The Säm fold structure: characterization of folding and metamorphism in a part of the eclogite – granulite region, Sveconorwegian orogen. *Dissertations in Geology at Lund University*, No. 367, 50 pp. 45 hp (45 ECTS credits).

Abstract: Structural and petrological studies on complexly folded mafic and felsic layered sequences have been mapped in the parautochthonous basement of the Sveconorwegian Province, Sweden. Three deformation phases (D_1, D_2, D_3) involving at least two fold phases (F_2, F_3) and two lineation phases (L_2, L_3) characterize a polyphase fold, which is primarily defined by a migmatized and highly competent garnet amphibolite. This unit was folded and boudinaged into map-scale tectonic lenses during upper amphibolite to granulite facies metamorphism.

Penetrative deformation during D_3 and D_2 created strong, composite fabrics. The oldest, D_1 event is interpreted as simply a deformation phase forming a gneissic S_1. D_2 folded the S_1 into similar-shaped, upright to inclined, closed to isoclinal folds (F_2). L_2 lineations have a bimodal distribution with two distinct clusters trending 37/318 and 26/160. The F_2 folds were subsequently refolded into a NE-plunging, open, Class 1C, Type 3 interference pattern folds (F_3) during D_3. The majority of L_3 lineations align parallel with the F_3 fold axis. L_3 has shallow to moderate plunges all trending NE (mean vectors: 19/052, 29/039 & 08/060). Syn-kinematic shear-sense indicators are consistently top-to-the-east.

Upper amphibolite to granulite facies was achieved in the garnet amphibolite gneiss. The earliest assemblages preserved plagioclase inclusions in clinopyroxene, and orthopyroxene forming coronas around clinopyroxene and Fe-Ti oxides, indicative of high temperatures ~800-850 °C at ~10 kbar. The texturally equilibrated mineral assemblage consists of garnet + clinopyroxene + plagioclase + quartz + hornblende + Fe-Ti oxide + biotite, and is found stable at *P-T* conditions of ~700-800 °C and ~9-14 kbar.

Mineral assemblages studied in the sillimanite-bearing quartz-feldspar gneiss showed a clockwise *P-T-t* evolution. A single grain of kyanite is believed to have been found. Tentatively, the paragneiss travelled through the relatively higher pressure, kyanite stability field; possibly during D_2. A stable mineral assemblage containing quartz + K-feldspar + plagioclase + biotite + sillimanite + garnet + Fe-Ti oxide, suggests *P-T* conditions of ~650-850 °C and ~3-10 kbar. Cordierite was found reacting with garnet in the presence of K-feldspar, which suggested D_3 decompression of ≤5 kbar occurred at high temperatures (≥650 °C).

Tectonic implications relating this structure with deformation observed elsewhere in the Eastern Segment is discussed.

Keywords: anatexis, high-T granulite, interference folds, polydeformation, Sveconorwegian orogen, SW Sweden

Supervisor: Charlotte Möller

Co-supervisor: Jenny Andersson

Stephen P. Michalchuk, Department of Geology, Lund University, Sölvegatan 12, SE-223 62 Lund, Sweden.
E-mail: spmichalchuk@gmail.com

Veckstruckturen i Säm: karakterisering av veckning och metamorfos i en del av eklogit – granulit regionen, Svekonorvegiska orogenesen

STEPHEN PAUL MICHALCHUK

Michalchuk, S.P., 2013: Veckstruckturen i Säm: karakterisering av veckning och metamorfos i en del av eklogit – granulit regionen, Svekonorvegiska orogenesen. *Examensarbeten i geologi vid Lunds universitet*, No. 367, 50 pp. 45 hp.

Sammanfattning: Strukturella och petrologiska studier av komplext veckade mafiskt- och felsiskt varvade sekvenser har genomförts i den paraautoktona delen av Svekonorvegiska provinsen i sydvästra Sverige. Tre deformationsfaser (D_1, D_2, D_3) innefattande minst två veckfaser (F_2, F_3) och två lineationsfaser (L_2, L_3) karakteriserar ett flerfasigt veck i migmatiserad och mycket kompetent granatamfibolit. Denna enhet veckades och boudinerades till tektoniska linser under metamorfos i övre amfibolit- till granulitfacies.

Penetrativ deformation under D_3 och D_2 skapade sammansatta strukturer. Den äldsta, D_1 tolkas som en deformationsfas vilken endast bildar en gnejsig S_1 struktur. D_2 veckade S_1 till likformade, upprätta till lutande, slutna till isoclinala veck (F_2). L_2 lineationen har en bimodal fördelning med två distinkta poler, 37/318 och 26/160. F_2 vecken omveckades därefter till ett NÖ-stupande, öppen, klass 1C, typ 3 interferensmönsterveck (F_3) under D_3. Majoriteten av L_3 lineationerna är parallella med F_3-veckaxeln. L_3 stupar svagt till måttligt i riktning NÖ (medelvärde för vektorerna: 19/052, 29/039 och 08/060). Synkinematiska skjuvindikatorer är genomgående topp-mot-öst.

Metamorfos i övre amfibolit- till granulitfacies kännetecknar granat-amfibolitgnejsen. De tidigaste mineralsällskapen består av plagioklasinneslutningar i klinopyroxen, ortopyroxen med coronabildning runt klinopyroxen samt Fe-Ti-oxider. De indikerar höga temperaturer, ~800-850 °C vid ~10 kbar. Mineralsällskapet i texturell jämvikt, bestående av granat + klinopyroxen + plagioklas + kvarts + hornblände + Fe-Ti-oxid + biotit, är stabilt vid *P-T* förhållanderna ~700-800 °C och ~9-14 kbar.

Mineralsällskapen i den sillimanitförande kvarts-fältspatgnejsen visar en medurs *P-T-t* utveckling. Endast ett korn av kyanit tros ha identifierats. Detta indikerar att paragnejsen har utsatts för högre tryck inom kyanitens stabilitetsområde, eventuellt under D_2. Ett stabilt mineralsällskap bestående av kvarts + K-fältspat + plagioklas + biotit + sillimanit + granat + Fe-Ti-oxider ger tryck och temperaturer kring ~650-850 °C och ~3-10 kbar. Reaktion mellan kordierit och granat i närvaro av K-fältspat, antyder att D_3 dekompressionen till ≤5 kbar skedde vid höga temperaturer (≥650 °C).

De tektoniska konsekvenserna av tolkningen av veckstrukturen i Säm diskuteras i relation till andra deformationsstrukturer i Östra segmentet.

Nyckelord: anatexis, hög-T granulit, interferens-veck, polydeformation, Svekonorvegiska orogenesen, SV Sverige.

Ämnesinriktning: Berggrundsgeologi

Stephen P. Michalchuk, Geologiska institutionen, Lunds universitet, Sölvegatan 12, SE-223 62 Lund, Sverige.
E-post: spmichalchuk@gmail.com

1 Introduction

Cratons are large, coherent regions of continental lithosphere that have remained stable since Precambrian times, which yield bountiful evidence on the geological history of orogenic events from long ago (Hoffman, 1988). Orogenic events are constrained based on geochronological data, geochemical signatures, petrology, and structural frameworks. Reconstructing these orogenic events are tedious endeavors. Often the most recent event is also the best preserved in the rock record; younger orogenies tend to overprint older events.

The Eastern Segment of the Sveconorwegian orogen (Grenvillian-age) exposed in southwest Sweden presents exceedingly ductilely deformed parautochthonous basement rocks, which were subjected to high pressures and temperatures (Johansson et al. 1991; Wang & Lindh 1996; Möller 1998, 1999; Andersson et al. 1999; Harlov et al. 2013). These high-grade rocks have provided insights toward deformation and metamorphism at great depths in the Earth's lower continental crust and upper mantle during continent-continent orogenesis. Ongoing research in the Eastern Segment has shown an isoclinal, non-cylindrical, east-plunging fold nappe that extruded eclogitized crust towards the Fennoscandian foreland (Möller et al. 2013). It is of great interest to correlate this tectonic structure with the surrounding gneisses of the Eastern Segment.

This study investigated a complexly folded mafic and felsic layered sequence initially mapped by Lundqvist (2008), focusing primarily on the structure, petrology, and microtextures to better constrain the spatial tectonic relationship in a region of the granulite to eclogite suite in the Eastern Segment of the Sveconorwegian orogen. Specifically, this study has characterized the 3D geometry of the Säm fold structure, and has characterized each deformation phase including: fold geometry, associated small scale structures, deformation fabrics, melts and segregations, and metamorphic assemblages.

2 Geological background

The Fennoscandian Shield comprises Archean and Proterozoic domains and is situated within the East European Craton (Baltica; Bogdanova et al. 2008). This shield is further subdivided into several tectonic provinces, each reflecting a distinct geological history. The Sveconorwegian orogen (1140-900 Ma) resulted from a continent-continent collision that penetratively reworked the southwestern Fennoscandian rocks (Bingen et al. 2008). This orogeny was associated with the formation of the supercontinent Rodinia (Dalziel 1997; Tohver et al. 2002; Pesonen et al. 2003; Li et al. 2008). The tectonic relationship of the Sveconorwegian orogen and its global counterparts is debated; ongoing research reveals substantial supporting evidence for a connection between the Grenville orogen on the Laurentian craton and the Sunsas orogen on the Amazonian craton with the Sveconorwegian orogen (Li et al. 2008; Johansson 2009).

The Sveconorwegian orogen (Fig. 1) is a 500 km wide mobile belt that is exposed from the southeastern Caledonian deformation front in southern Norway and extends eastward to south-central Sweden. The eastern boundary is marked by the Sveconorwegian Frontal Deformation Zone (SFDZ; Wahlgren et al. 1994). The orogen is bounded in the south by Phanerozoic cover rocks. The

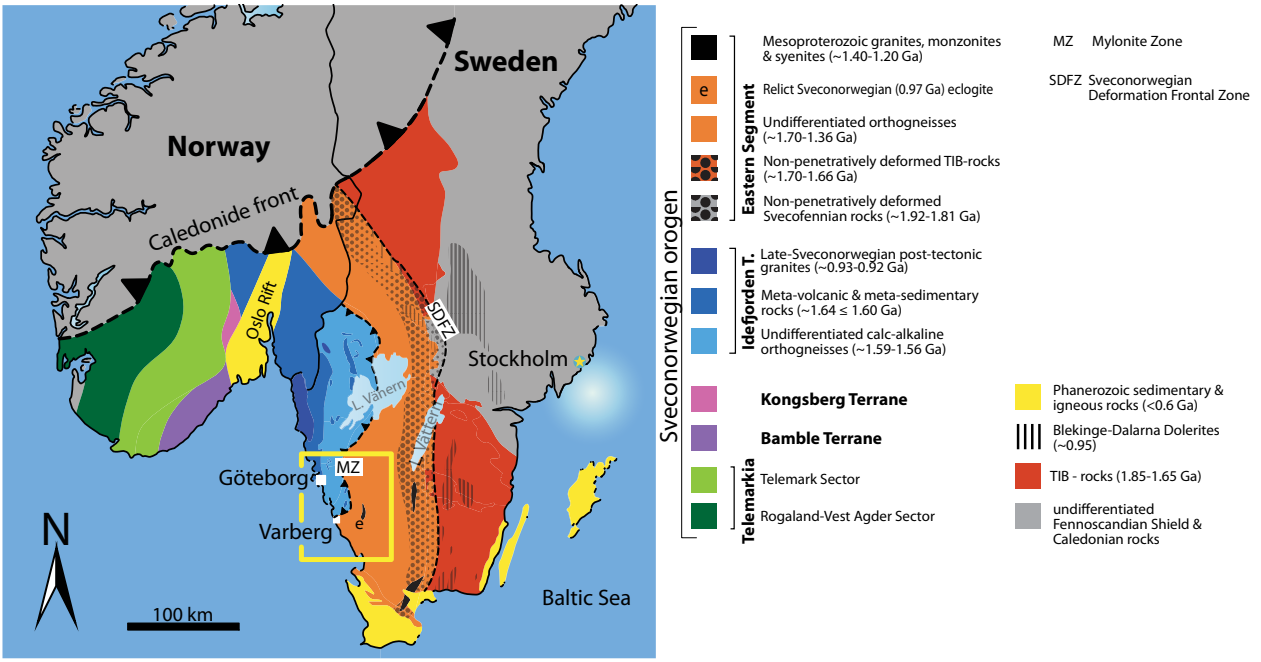

Fig. 1. Sketch tectonic map of the main crustal units comprising the Sveconorwegian orogen in southwestern Scandinavia (modified after Andersson et al. 2002; Bingen et al. 2005; Viola et al. 2011). Major tectonic boundaries located along the Eastern Segment are the Mylonite Zone (MZ) and the Sveconorwegian Deformation Frontal Zone (SDFZ). Yellow rectangle shows the location for Fig. 2.

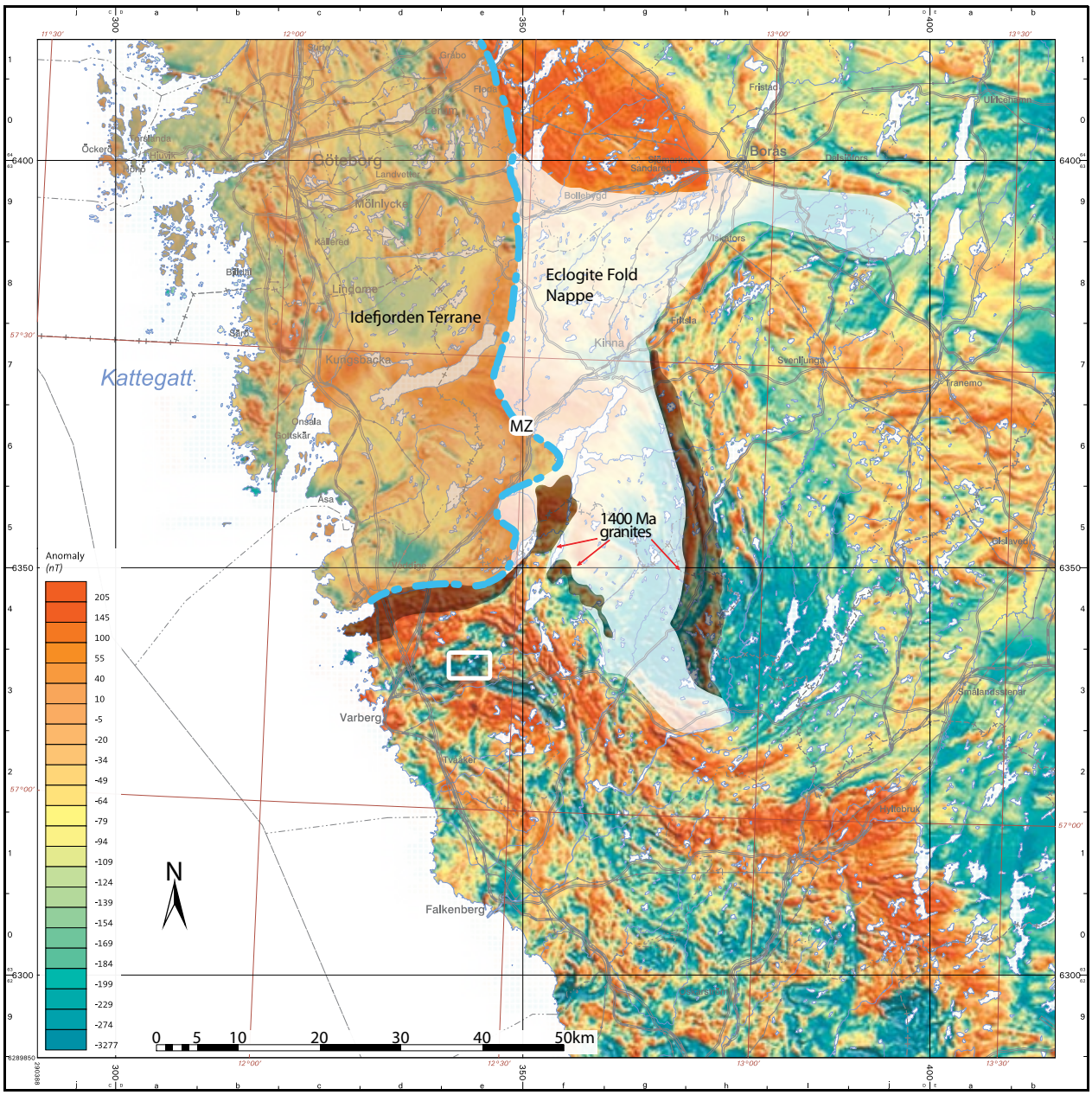

Fig. 2. Airborne magnetic anomaly map over a part of the Eastern Segment and the Idefjorden Terrane. The Idefjorden Terrane is darkened, whilst the Eclogite Fold Nappe, bounded by the deeply darkened ~1400-1370 Ma granites in the Eastern Segment, is highlighted (after Möller et al. 2013). Mylonite Zone (MZ) separates the Idefjorden terrane from the Eastern Segment. The field area pertaining to this study is outlined by the white rectangle. Black grid coordinates are SWEREF 99 TM; brown grid coordinates are SWEREF 99. Data source: Geological Survey of Sweden (SGU).

Sveconorwegian orogen consists of five main lithotectonic segments; each segment is separated by roughly north-south trending crustal scale bounding shear zones (Bingen et al. 2005). They are, from east to west: The Eastern Segment, the Idefjorden Terrane, the Kongsberg Terrane, the Bamble Terrane, and the Telemarkia Terrane. The Mylonite Zone is the crustal scale shear zone separating the Idefjorden Terrane from the parautochthonous Eastern Segment (Andersson et al. 2002).

Two orogenic phases, termed Falkenberg and Dalane by Bingen et al. (2008), reworked the Eastern Segment rocks. The Falkenberg phase (980-960 Ma) marked the final episode of Sveconorwegian convergence, whilst the Dalane phase (960-900 Ma) encompassed the post-collisional crustal relaxation and cooling below ~500 °C (Page et al. 1996; Söderlund et al. 2005, 2008).

Sveconorwegian reworking and metamorphic grade in the Eastern Segment increases from north to south (Johansson et al. 1991). In the southern Eastern Segment, the western rocks experienced deeper crustal environments than those in the east (Johansson & Kullered 1993; Möller 1998, 1999). Temperature and pressure estimates from the southern Eastern Segment are 680-800 °C and 8-12 kbar, reflecting upper amphibolite to high-pressure granulite metamorphic grades (Johansson et al. 1991; Wang & Lindh 1996; Andersson et al. 1999; Harlov et

al. 2013). Penetrative deformation and anatectic melting throughout much of the Eastern Segment, obliterated most of the primary fabrics in the protoliths. There are, however, a few exceptions where primary or older features at particular localities are preserved.

Protoliths are 1810-1660 Ma gneisses that share geochemical similarities with the monzogranitic and alkali-calcic granitic Transcandinavian Igneous Belt (TIB) rocks, ~1570 Ma mafic dolerite dykes, ~1470-1420 Ma mafic and felsic magmatism, and ~1400-1370 Ma granites and monzonites affiliated with the Varberg-Torpa-Charnockite-Granite suite (Hubbard 1975, 1989; Johansson & Kullerud 1993; Wahlgren et al. 1994; Söderlund et al. 1999, 2002; Andersson et al. 2002; Högdahl et al. 2004; Brander & Söderlund 2009). The 1400 Ma granites are variably deformed varieties of orthoclase megacrystic granites, including dark greenish grey varieties commonly termed charnockites. With the exception of the 1400 Ma rocks, relatively undeformed equivalents of the Eastern Segment granitoids and syenites are found east of the Sveconorwegian front, in the Fennoscandian foreland (Gorbatschev & Bogdanova 1993; Högdahl et al. 2004).

Regional deformation during the Falkenberg and Dalane phases in the southern Eastern Segment resulted in upright to southwards overturned folds with E–W to WNW–ESE trending subhorizontal fold axes; stretching lineations trend in a similar direction (Möller & Söderlund 1997; Möller et al. 1997, 2007). An eclogite-bearing large-scale recumbent fold has been located in the western part of the southern Eastern Segment (Fig. 2; Möller et al. 2013). In its southern part the (Ullared-Ätran area), the gneissic layering has been folded by a major fold phase (F_2) characterized by subhorizontal fold axes plunging E or ESE (Möller & Söderlund 1997; Möller et al. 2013; Tual et al. 2013). Farther to the south, near Halmstad, gneissic foliations are orientated NNE-SSW and tight folds plunge SSW, whilst stretching fabrics trend ESE (Möller et al. 2007).

3 Methods

Geological mapping was performed at 1:10000 scale during 4 weeks in September and October 2012. The study area, centred on the farming village of Säm, is located 20 km east of Varberg in Hallands län, SW Sweden. Bedrock maps in the 1:50000 scale published by the Swedish Geological Survey (SGU; Lundqvist 2008) and previous outcrop observations (SGU) facilitated this study's field mapping. Lithology and structures were identified and documented at 107 localities, those referred to in the text are listed in Table A1. Global Positioning System (GPS) data (WGS84 and SWEREF 90 TM) was gathered with a Garmin Oregon instrument along with a Nikon DSLR equipped with Nikon's GP-1 using WGS84 to geo-tag field photographs at time of capture. The attitudes of foliations are expressed using strike/dip following the right-hand rule convention, whilst lineations are expressed using plunge/trend (equivalent to plunge/plunge direction; Marshak & Mitra 1988). Strikes and trends are always expressed using the azimuthal system. Foliations, lineations, and fold axis orientations with dips were plotted on the lower hemisphere of equal area stereographic projections in Cardozo & Allmendinger's (2013) OSXStereonet. Mineral abbreviations follow Kretz (1983). Amphibole and pyroxene nomenclature is according to Leake et al. (1997) and Morimoto et al. (1988) respectively. Anatectic melt terminology (Fig. 4A) follows Sawyer (2008). Foliation boudinage structures (FBS) follow the classification proposed by Arslan et al. (2008).

Thirty-three hand samples representing type-lithologies, microstructures, and textures were selected for polished thin section preparation (Table 2). Polarized microscopy was conducted using a Nikon eclipse E400 POL fitted with a Luminera Infinity1-2CB camera for photomicrographs. High-contrast back-scattered electron (BSE) images were produced from a Hitachi S3400N SEM (scanning electron microscope) fitted with an EDS (Energy-Dispersive x-ray Spectroscopy) and programmed with Link INCA at the Department of Geology, Lund University. An acceleration voltage of 15 kV, counting times between 60 and 80 s, and a focused electron beam examined the carbon-coated thin sections.

4 Results

4.1 Geology of the Säm area

4.1.1 Previous geological map

Previous bedrock mapping in the Säm area conducted by the SGU produced a 1:50000 geological bedrock map containing 3 main lithological types and abundant pegmatitic dykes in a kilometre-scale polyphase fold (Berggrundskartan 5B Varberg NO; Lundqvist 2008). The main lithologies found on the SGU map are gneissic granodiotite, gneissic granite and garnet amphibolite, the latter defining the polyphase fold. Gneissic foliations trend ENE-WSW to NNE-SSW and dip 20-50° N to E.

Lithologies described herein (section 4.3) for the Säm area are slightly modified after Lundqvist (2008). The garnet amphibolite remains unchanged from the SGU map. The gneissic granite is renamed to a quartz-feldspar gneiss unit with pegmatite veins. The gneissic granodiorite remains on the map but was encountered at one locality. A garnet-poor amphibolite, a sillimanite-bearing quartz-feldspar gneiss, and a charnockitized felsic orthogneiss are added.

4.1.2 Rock types

The mapped area surrounding Säm (Fig. 3) is largely composed of five main rock types (Fig. 4), all of which are fine- to coarse-grained: 1) reddish quartz-feldspar gneiss with abundant coarse-grained pegmatite veins, 2) red-grey sillimanite-bearing quartz-feldspar gneiss, 3) grey garnet-poor amphibolite gneiss with local occurrences of calc-silicate / epidote lenses, 4) migmatitic garnet amphibolite gneiss, and 5) charnockitized felsic orthogneiss; the latter of limited exposure. The rocks have been overprinted by anatectic melting and penetrative hetero-

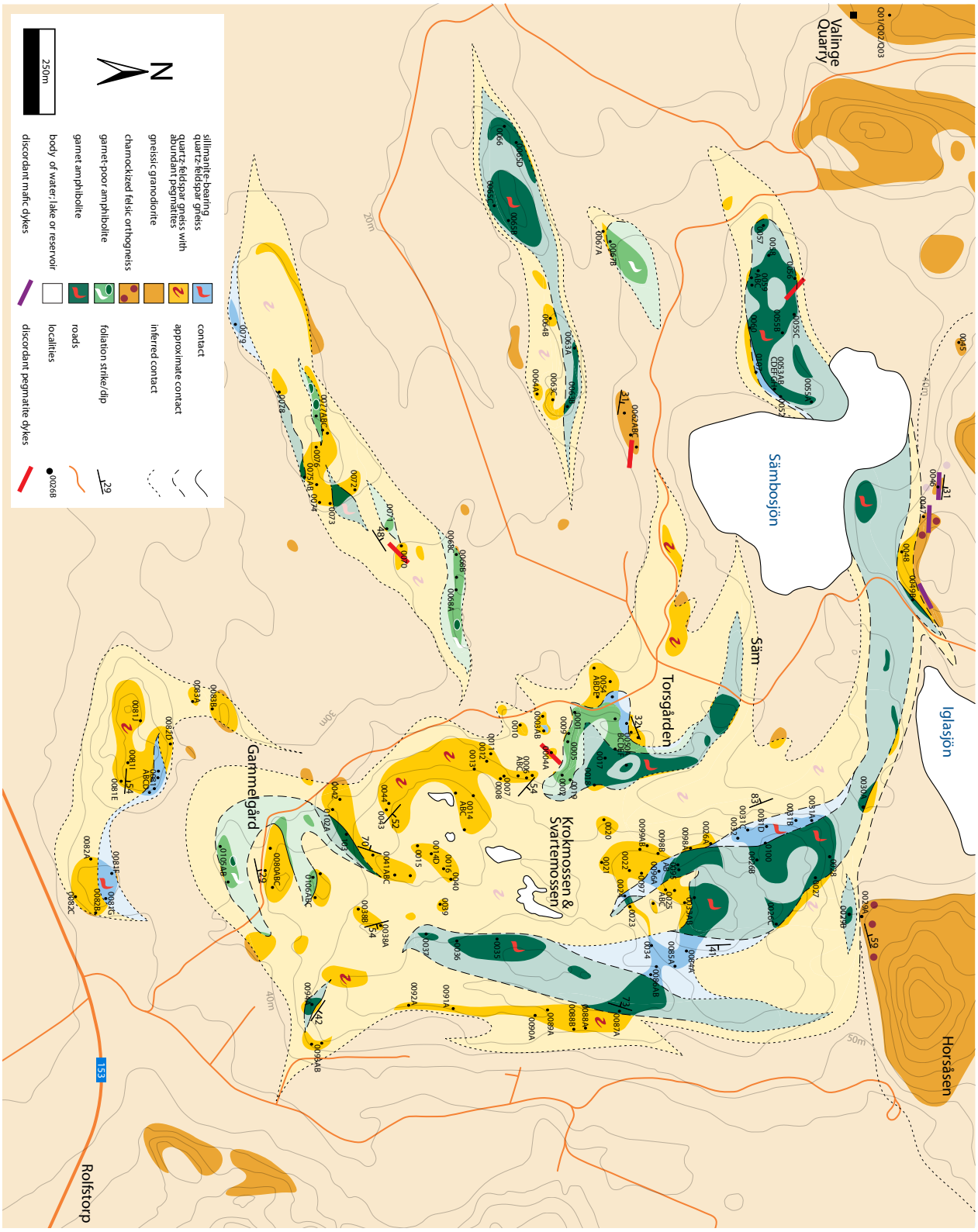

Fig. 3. Lithological map with 107 enumerated localities and select structural observations plotted. Outcrops are brightly coloured whilst covered sections are faded. Topographic contours are 10 m intervals. Colour scheme follows that of C. Möller and J. Andersson for the Eastern Segment.

geneous deformation, hindering precise determination of the original compositions and structures of the protoliths. Strain is qualitatively observed from folds, microstructures, and microtextures. All rocks have undergone a similar deformational and metamorphic history, however they do not all share similar structures and fabrics. Competency contrasts between units dictate the degree of strain and the character of structures and fabrics. Several structurally younger dykes, themselves strongly deformed, locally crosscut gneissic foliations and therefore do not share the full history of the host. Vegetation and unconsolidated glacial deposits and soils limit rock exposure; rock contacts are seldom observed. Elevated topography correlates with the occurrence of weathering-resistant (and competent) rocks such as the amphibolites.

4.2 Structural geology

4.2.1 General structure

Bedrock mapping conducted by Lundqvist (2008) revealed map-scale boudinaged amphibolite tectonic lenses folded into what appeared as two distinct phases. These amphibolite tectonic lenses are often associated with heterogeneously deformed quartz-feldspar gneisses. This study confirms the previously mapped observations.

Results pertaining to the structural study are summarized in the two structure maps; one for foliations and one lineations, with accompanying stereonets (Figs. 5 & 6 respectively). Two interpretative cross-sections (Fig. 7) illustrate the deformation phases interpreted from the field data.

The polyphase fold is primarily defined by the migmatized and highly competent garnet amphibolite. This unit was folded and boudinaged into map-scale tectonic lens-

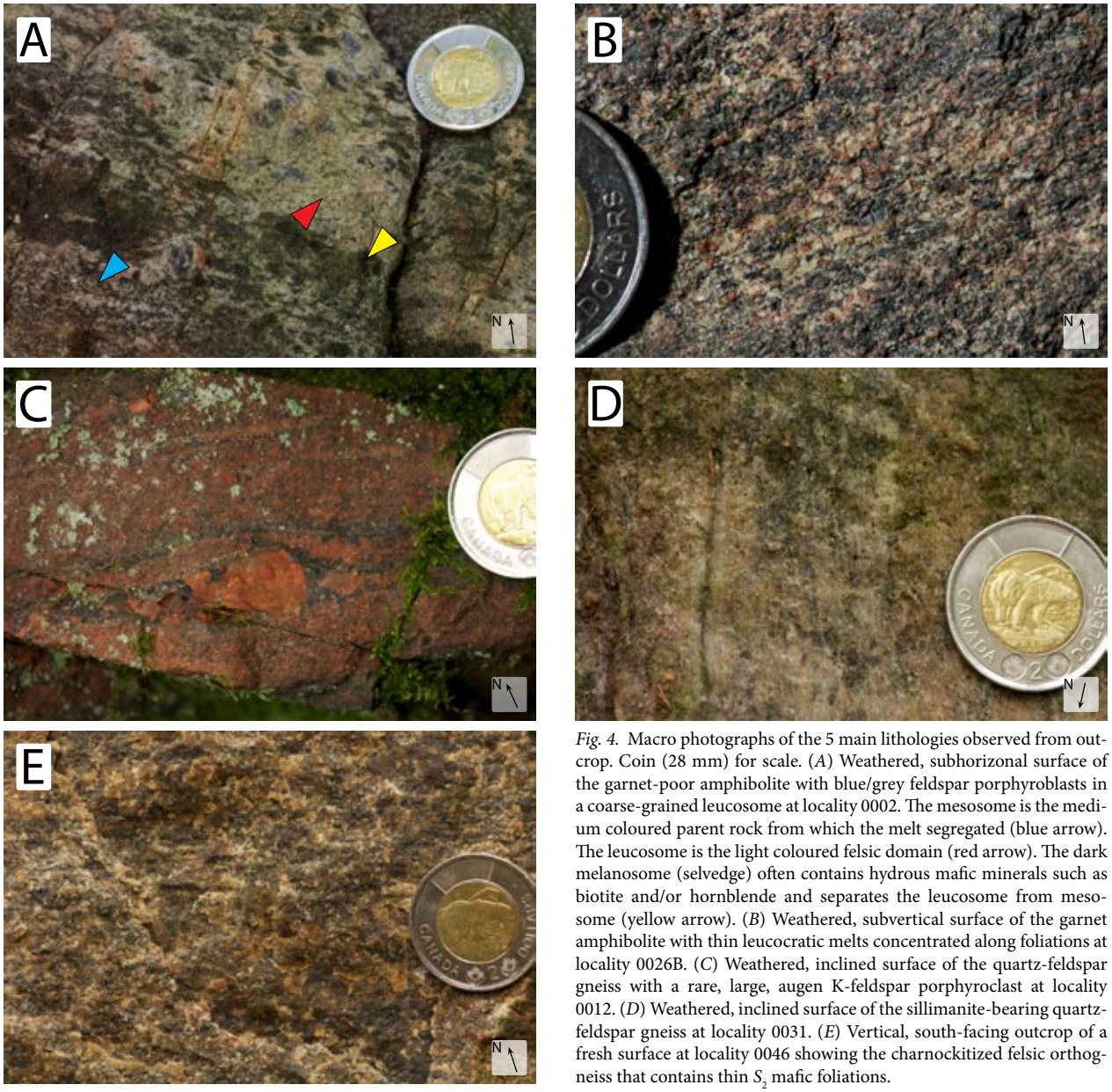

Fig. 4. Macro photographs of the 5 main lithologies observed from outcrop. Coin (28 mm) for scale. (*A*) Weathered, subhorizonal surface of the garnet-poor amphibolite with blue/grey feldspar porphyroblasts in a coarse-grained leucosome at locality 0002. The mesosome is the medium coloured parent rock from which the melt segregated (blue arrow). The leucosome is the light coloured felsic domain (red arrow). The dark melanosome (selvedge) often contains hydrous mafic minerals such as biotite and/or hornblende and separates the leucosome from mesosome (yellow arrow). (*B*) Weathered, subvertical surface of the garnet amphibolite with thin leucocratic melts concentrated along foliations at locality 0026B. (*C*) Weathered, inclined surface of the quartz-feldspar gneiss with a rare, large, augen K-feldspar porphyroclast at locality 0012. (*D*) Weathered, inclined surface of the sillimanite-bearing quartz-feldspar gneiss at locality 0031. (*E*) Vertical, south-facing outcrop of a fresh surface at locality 0046 showing the charnockitized felsic orthogneiss that contains thin S_2 mafic foliations.

es. A major F_2 hinge is defined near Gammelgård, with fold axis orientated 24/029 (plunge/trend). A prominent F_3 hinge is located northeast of Säm, with fold axis orientated 38/025. A minor F_3 hinge is located in Torsgården, with fold axis orientated 36/041. Throughout the study area, object and trace lineations generally trend NE with varying plunges; the mean vector is 19/052 (stereonet α).

4.2.2 Linear structures and fabrics

There are two sets of lineations, L_2 and L_3, in the Säm area. Object lineations form in a variety of rocks from fine-grained, elongate aggregates that were produced by the stretching and recrystallization of previous coarser mineral grains; e.g. grain lineations and aggregate lineations (after Piazolo & Passchier, 2002). Trace lineations (crenulation lineation) are also present at select locations.

The L_2 are observed primarily from object lineations. L_2 have a bimodal distribution with two distinct pole clusters at 37/318 and 26/160 (stereonet β), thus trending in similar orientations although plunging in opposite directions.

The L_3 are observed from both object lineations and trace lineations. The majority of L_3 lineations align parallel with the F_3 fold axis. L_3 has shallow to moderate plunges all trending NE (mean vectors: 19/052, 29/039 & 08/060; stereonets α & γ). The following are examples of object lineations. Aggregate mineral lineations at locality 0001 trend ~058° and are subhorizontal (Fig. 8A). At locality 0077A, grey metallic luster, Fe-Ti-oxides form subhorizontal grain lineations trending ~079° in the folded coarse pegmatites (Fig. 8B).

Symmetrical and asymmetrical lobate structures with an ~80-120 mm wavelength and an ~20-50 mm amplitude were found beneath overhanging ledges of the recrystallized quartz-feldspar gneiss (Fig. 9A). These folds form coarse rods, which are parallel to the fold axis of cuspate-lobate folds. The axes and troughs are L_3 crenulation lineations (mean vector: 08/060; red triangles in stereonet γ). This structure is primarily located in the F_3 hinge zone near Torsgården, and is parallel to the F_3 fold axis.

4.2.3 Planar structures and fabrics

The primary compositional layering (S_0) and subsequent deformation events, D_1 and D_2, have created a composite, strong, planar, and gneissic S_2 fabric. A locally preserved S_0 has yet to be found in the Säm area due to younger penetrative overprinting, therefore the orientation of the S_0 is unknown. S_1 is preserved, and is distinguished from S_2 because S_1 was folded isoclinally during the distinctly characteristic D_2. Therefore, S_1 is commonly intrafolial with respect to S_2. This composite structure allowed for numerous foliation plane measurements at each locality. There is a mineralogically derived anisotropic weakness along folia; surfaces are more easily cleaved (Fig. 9B). The layer thickness varies; a common range is from millimeter to decimetre (lamellar to thick banding). The orientations of the composite S_0, S_1, and S_2 foliations outline the F_3 fold phase, which forms the S_3 foliation.

4.2.3.1 Mylonitic structures and fabrics

Gradational mylonitized zones occur in the quartz-feldspar gneiss appeared in two hinge-zone localities, F_2 (0080; Fig. 10A) and F_3 (0098A; Fig. 10B). Strain partitioning amongst the quartz and feldspar minerals allowed an anisotropic shape pattern to develop. Distributed augen-shaped porphyroclasts and recrystallized lens occur parallel to these major anisotropic planes. A dextral shear-sense was observed at locality 0098A. Whilst the mylonite and the coarse protomylonitic quartz-feldspar gneiss (Fig. 11) at locality 0080 is characterized with short, anastomosing shear bands that are oblique to the shear-zone boundaries, which suggests a *S-C′* fabric with a top-to-the-east shear-sense. At both localities, the mylonites are located close to (within 10's of metres) a large amphibolite lens. Measured widths of the mylonitized shear zones were in the order of several centimetres to metre scale. It is unclear if/how these mylonites are interconnected. In thin section, the mylonite is characterized with discrete, smooth and rough, anastomosing spaced foliation (see section 4.3.3.1). The foliation is defined by very, fine-grained sillimanite aggregates, elongate biotite clusters, with poly- and monocrystalline quartz ribbons. Finer, recrystallized quartz and feldspar grains are found in the microlithons.

4.2.3.2 Crosscutting aplitic and mafic dykes

Planar crosscutting relationships between lithologies were rare, however discordant aplitic and mafic dykes were mapped along two F_3 limbs.

One locality, 0062, exposes a fine-grained granodiorite gneiss where the foliation, defined by pinned quartz and plagioclase crystals against parallel-aligned biotite, is orientated 241/48. This foliation is then crosscut by several fine-grained, pinkish-white, centimetre-decimetre thick, very fine-grained aplitic dykes orientated ~261/32 (Figs. 12, 32D). The gneissic fabric is abruptly truncated at an angle of 22° (dihedral angle measured in OSXStereonet) by the dyke. The aplite dykes pinch and swell along strike, but appear perfectly undeformed. The foliations in the host gneiss do not show a soft or pliable tendency to merge into, or form drag folds near the intrusion. There appears to be a "chilled margin" marked by a finer grain size along the contact between the dykes and the host, suggesting that the gneiss was cool at the time of intrusion. A few metres westward along strike, the aplite dykes are nearly parallel to the gneissic fabric and remain relatively undeformed.

At localities, 0046, 0047, 0048, and 0049B (Figs. 13, 32A-C), several decimetre thick, mafic dykes are orientated parallel with the gneissic foliation of the charnockitic orthogneiss; foliations in the host are orientated between ~278/32 to 256/24 along this transect. There is only one locality that presents the mafic dykes crosscutting the foliations in the host (locality 0049B). The contact between the dykes and the host varies between sharp and grada-

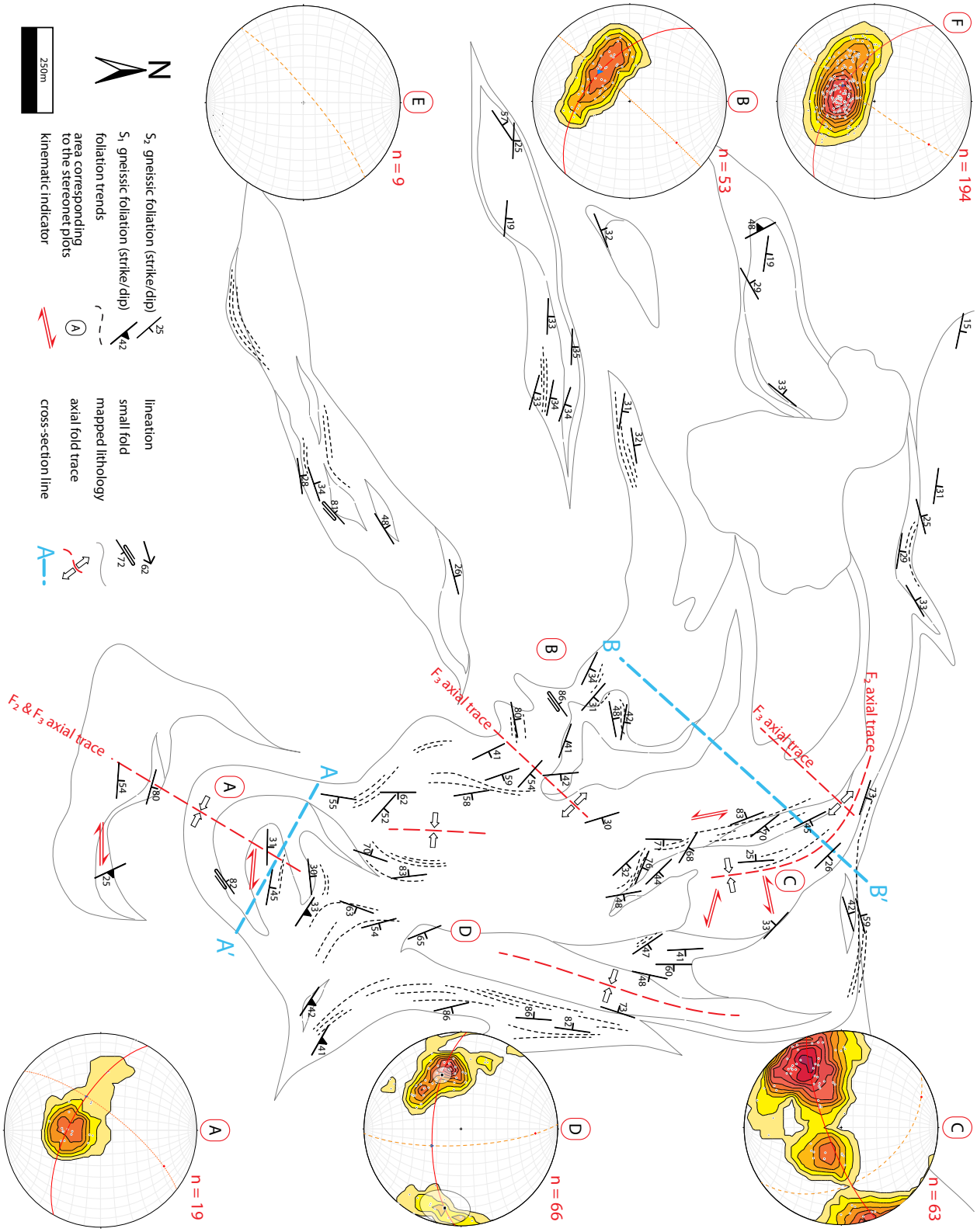

Fig. 5. Structure map with select foliation measurements, foliation trends, axial fold traces, cross-section lines, and letters corresponding to stereonets. Lower hemisphere equal-area (Schmidt) stereonet plots for (A) foliations around Gammelgård, (B) foliations around Torsgården, (C) horizontal to subvertical foliations in the F_3 hinge zone, (D) steeply dipping foliations near Krokmossen & Svartemossen, (E) the axial planes to small, tight F_2 folds, and (F) select foliation measurements throughout the study area defining the F_3 phase. The red solid great circle in the stereonets is the π-girdle, and the orange dashed great circle denotes the axial plane. See appendix (Fig. A1) for enlarged stereonets with supplementary information.

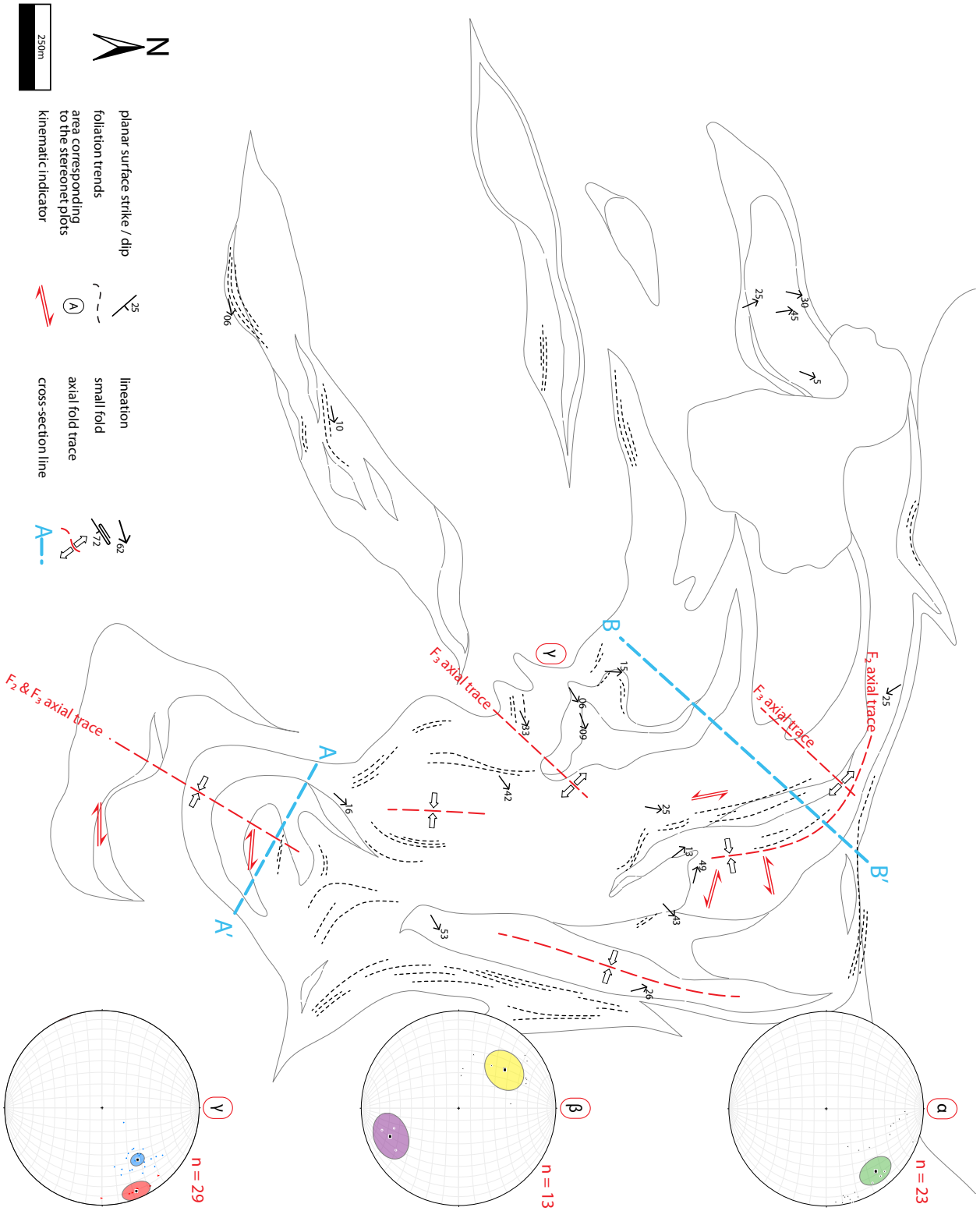

Fig. 6. Structure map with select lineation measurements, foliation trends, axial fold traces, cross-section lines, and letters corresponding to stereonets. Lower hemisphere equal-area (Schmidt) stereonet plots for (α) object lineations orientated parallel to the F_3 fold axis found throughout the study area, (β) object lineations orientated NW-SE found throughout the study area, and (γ) object lineations (blue) with trace lineations (axes of cuspate-lobate folds; red) around Torsgården. See appendix (Fig. A1) for enlarged stereonets with supplementary information.

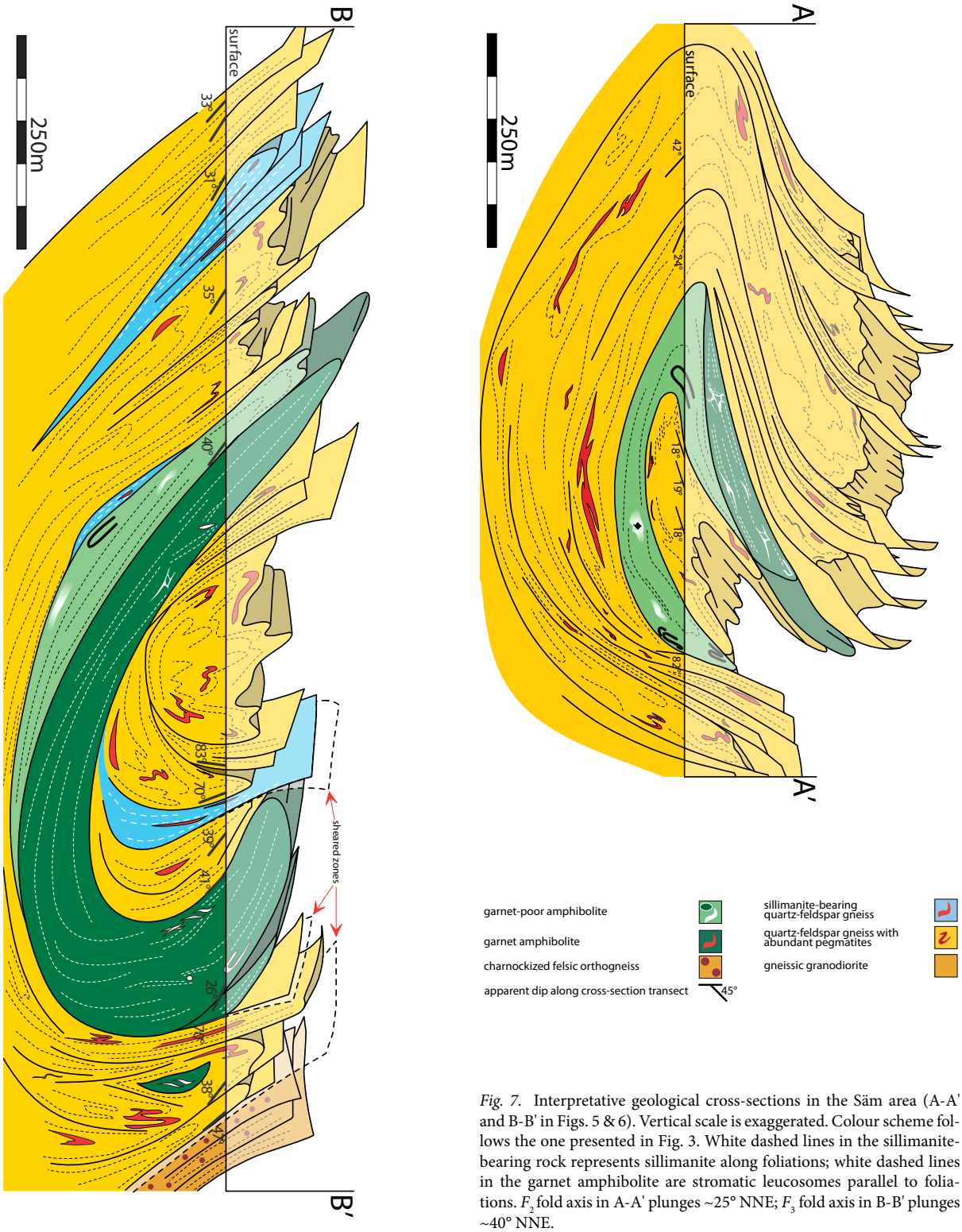

Fig. 7. Interpretative geological cross-sections in the Säm area (A-A' and B-B' in Figs. 5 & 6). Vertical scale is exaggerated. Colour scheme follows the one presented in Fig. 3. White dashed lines in the sillimanite-bearing rock represents sillimanite along foliations; white dashed lines in the garnet amphibolite are stromatic leucosomes parallel to foliations. F_2 fold axis in A-A' plunges ~25° NNE; F_3 fold axis in B-B' plunges ~40° NNE.

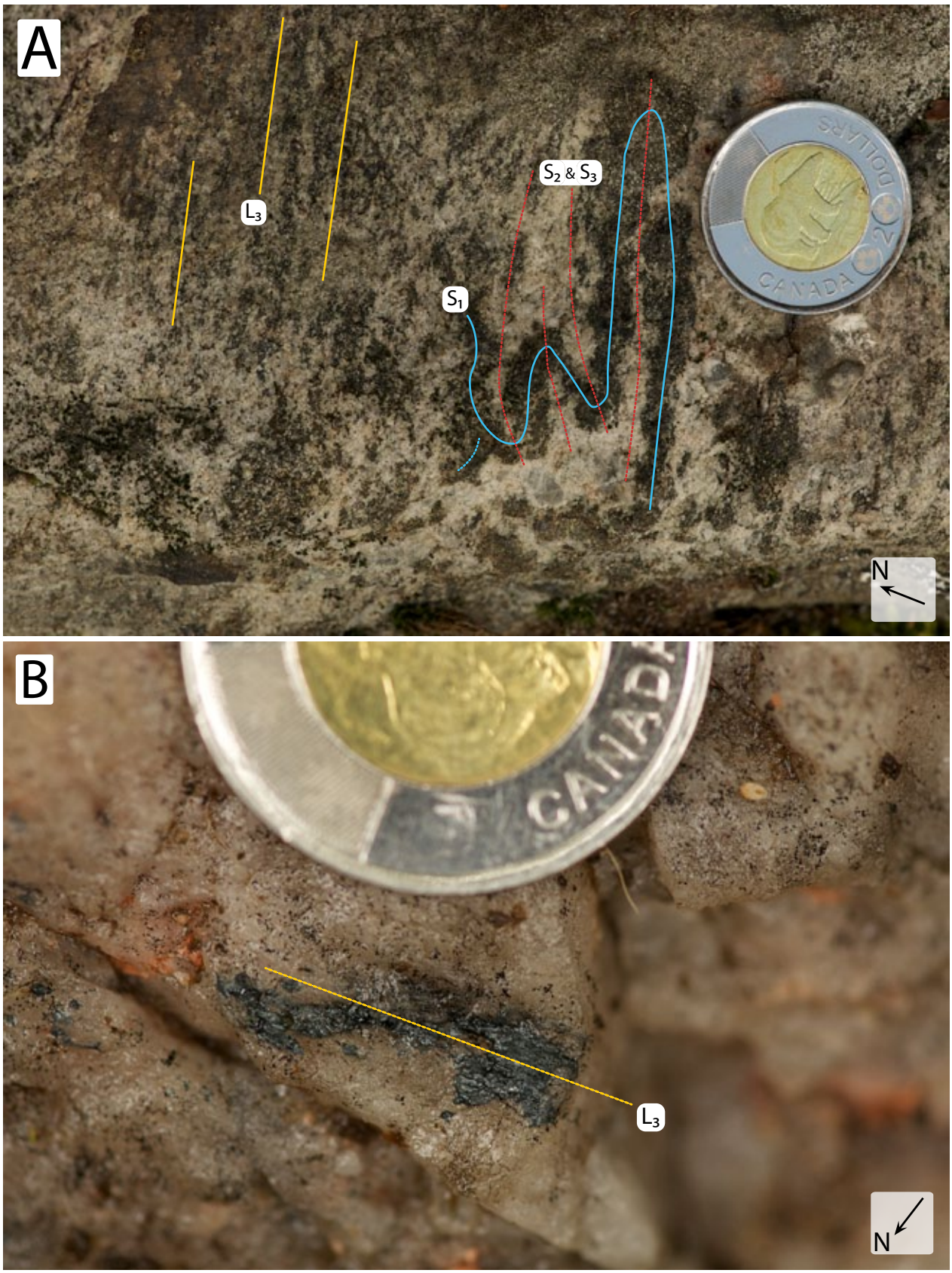

Fig. 8. (*A*) Horizontal surface of upright, isoclinal mafic mineral folds (F_3 overprinting F_2 folds; Ramsay's Type 0 interference fold pattern) in the garnet-poor amphibolite at locality 0001. The folds have a wavelength of ~12 mm. On the right-most half, subhorizonal, gently plunging mafic mineral aggregates create a strong L_3 linear fabric orientated 058°, this fabric aligns parallel with the S_2 and S_3 axial surface. (*B*) Elongated, fine-grained, Fe-Ti oxide opaque aggregate lineation (interpreted as L_3) on a horizontal surface at locality 0077A; azimuth is ~079°. Lineations are dispersed throughout the coarse quartz crystals in the folded pegmatites and quartz-feldspar gneiss outcrop. Coin (28 mm) for scale.

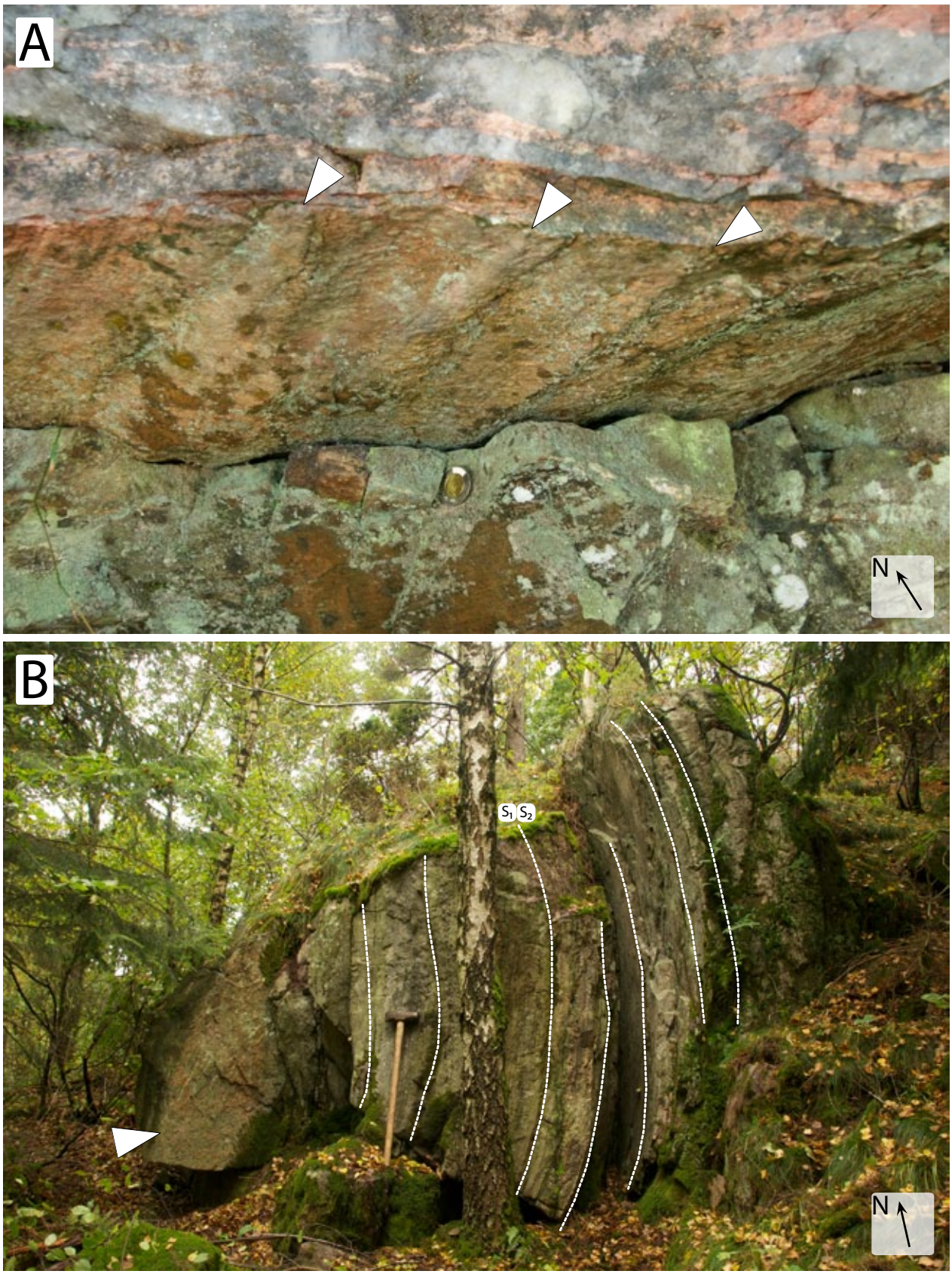

Fig. 9. (*A*) A coarse-grained, pegmatite dyke in the quartz-feldspar gneiss at locality 0007. There are subtle, however persistent lobate "ribs" (white arrows) along the basal surface of the ledge that are created by folding during ductile deformation (D_3) in the compressed F_3 hinge area. The axes of these cuspate-lobate folds create a trace lineation; mean vector is 08/060. Coin (28 mm) for scale. (*B*) Subvertical foliated quartz-feldspar gneiss unit at locality 0100. Folia thicknesses are mm-cm. Stacked packages of several foliations cleave every few dm's. Individual lamella are not laterally extensive and typically die out within a meter. No penetrative lineation fabrics or slickensides along foliation surfaces were observed. Isoclinal folds similar to the ones found at locality 0099A are indicated by the white arrow. A few tens of metres to the west, lies near-vertical, foliated, sillimanite-bearing quartz-feldspar gneiss. A few tens of metres to the east lies the garnet amphibolite unit. Sledgehammer (914 mm) for scale.

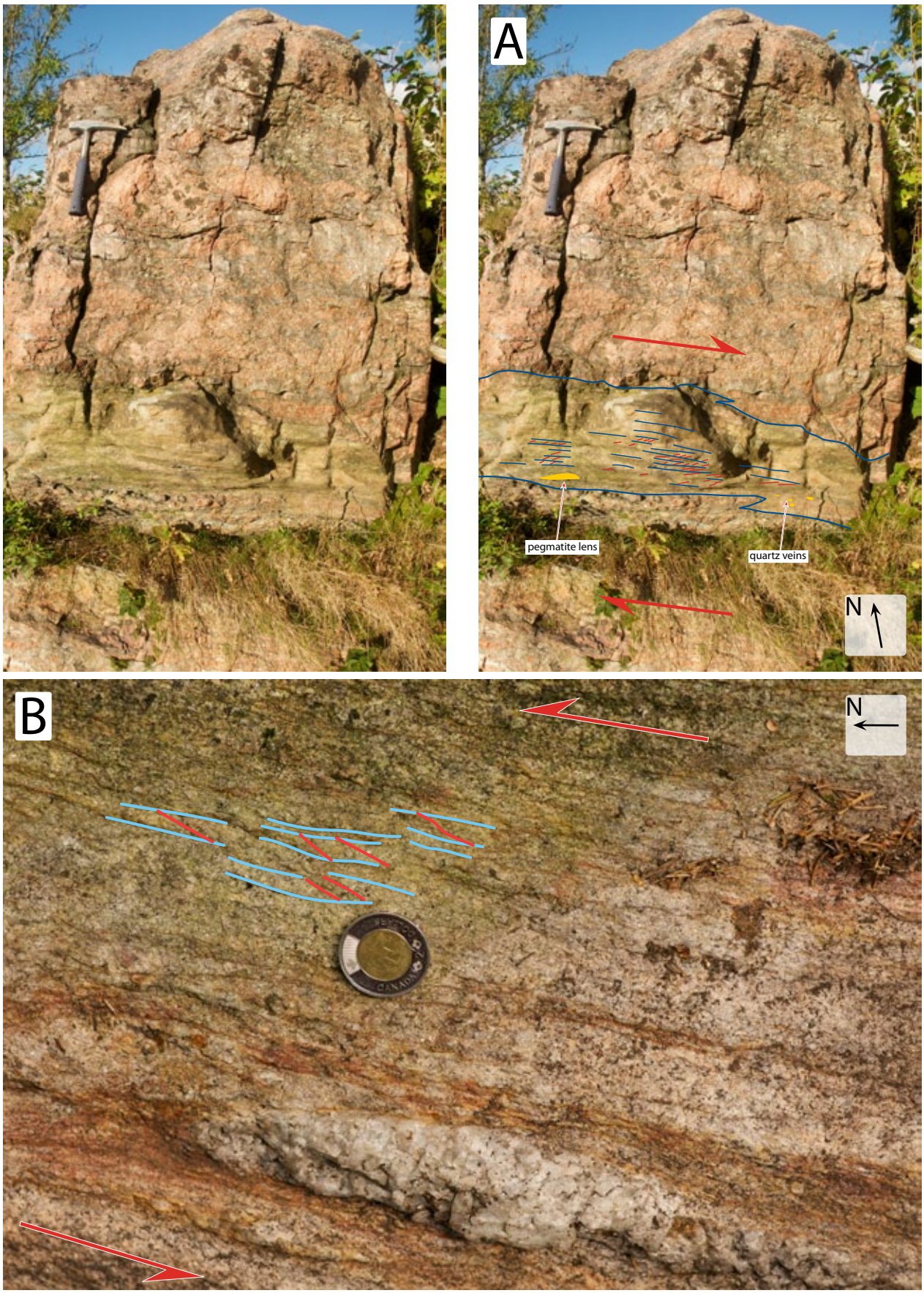

Fig. 10. (*A*) South-facing protomylonitic pegmatite dyke outcrop with a several decimetre thick, fine-grained mylonite zone in the quartz-feldspar gneiss host at 0080. *S-C* fabric is better identified in the mylonitic section than in the gneiss; see Fig. 11 for detail of the gneiss. Blue lines represent *C*-surfaces, whilst the red indicate *S*-surfaces. Shear direction is top-to-the-east. Hammer (330 mm) for scale. (*B*) A perpendicular surface to the finite strain ellipsoid of a mylonitized zone in the quartz-feldspar gneiss at locality 0098A. Shear is interpreted as sinistral. Coin (28 mm) for scale.

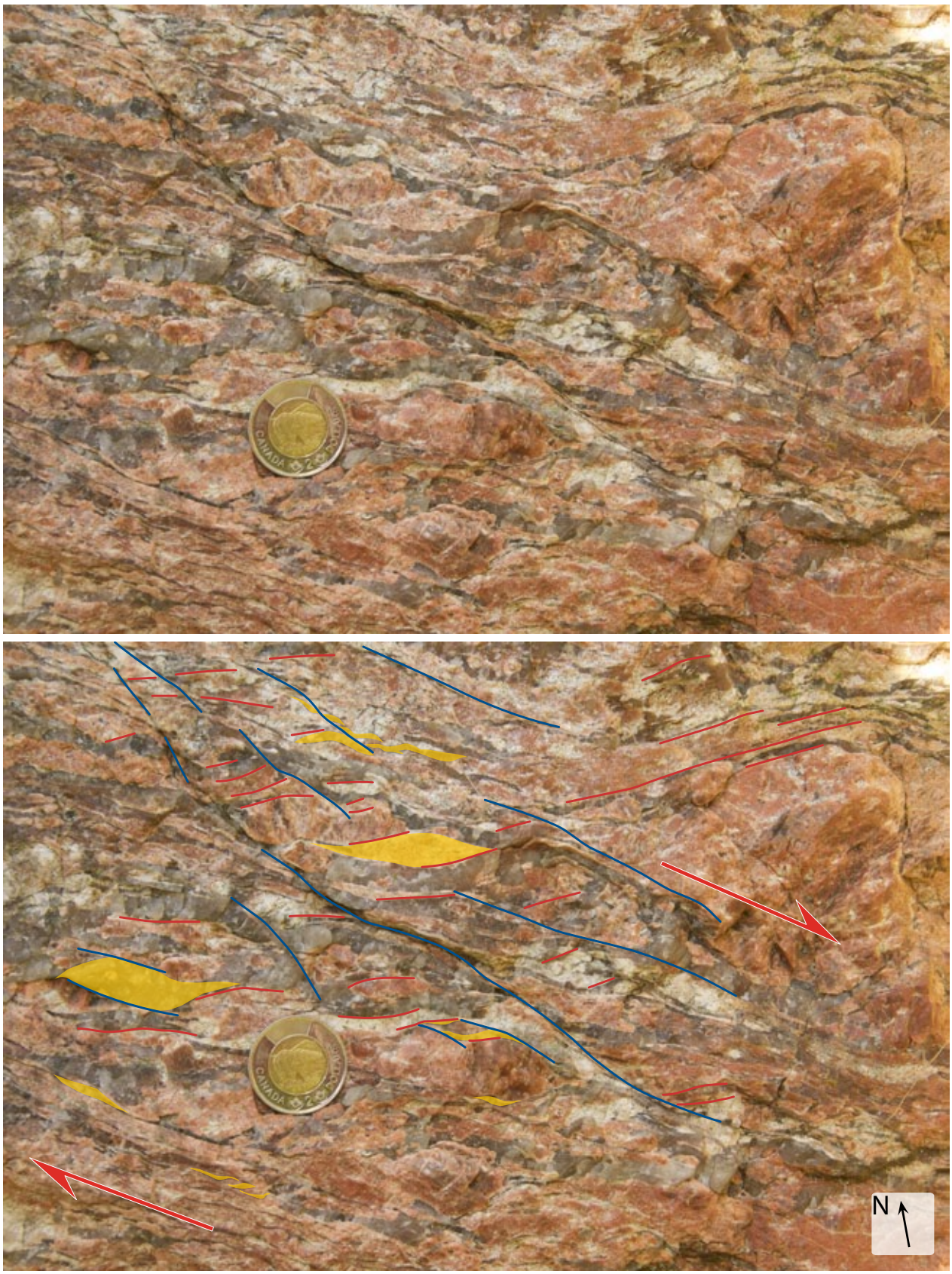

Fig. 11. Close-up of the protomylonitic pegmatite dyke along a south-facing vertical surface at locality 0080. Short, anastomosing shear bands with tapering en-échelon quartz ribbons that are orientated obliquely to the shear-zone boundaries show a *S*-*C*′ fabric. *S*-surfaces are red, whilst the blue lines indicate a *C*′-surface. *S*-surfaces are undulating and not consistently parallel. Laminar flow allows the *S*-surfaces to asymptotically become truncated by the anastomosing *C*′-surfaces. Shear-sense is dextral; top-to-the-east. Coin (28 mm) for scale.

tional; often a centimetre thick biotite or hornblende-rich lamella may be traced along strike for several decimetres, which marks the boundary between the intrusion and the host (Fig. 4E). Thin sections reveal the dykes are well foliated similar to the host charnockitic felsic orthogneiss.

4.2.3.3 Folds and fold-related fabrics

Two different fold phases, F_2 and F_3, have been identified. Folds generally involve one or two foliated layers, are termed single-layer folds, and are widespread in the Säm area. All folds have been subjected to boudinage synkinematically with folding and thus very short segments, typically one or two wavelengths, are preserved.

The F_2 folds are the most commonly occurring fold phase around Säm, and are found in several lithologies: the garnet-poor amphibolite, the garnet amphibolite, and the quartz-feldspar gneiss. The S_1 gneissic foliations were modified and reoriented during D_2 to form NNW-SSE striking, upright to recumbent and tight to isoclinal F_2 folds (stereonet D from Fig. 5; Figs. 8A & 14A). Around Krokmossen & Svartemossen, the corresponding stereonet D (Fig. 5) illustrates the F_2 with a narrow hinge zone, as denoted by the poles from the S_1 gneissic foliations that are segregated into two distinct clusters. The angle between these two clusters is ~114°, thus the supplement angle of ~66° is the dihedral angle (i.e. interlimb angle). The axial plane (S_2) bisects the F_2 limbs with an orientation of 357/76, whilst the axial hinge (L_2) is 24/003.

Small, thin, pegmatitic veins (an earlier generation of intrusions than those presented in section 4.2.3.2) in the quartz-feldspar gneisses were folded during D_2, and developed angular, narrow, and often isolated hinges. Planar limbs are strongly stretched or boudinaged, parallel to the axial plane (S_2 ; Figs. 14B, 15-18). These F_2 folds are best classified as Class 2 similar folds (Ramsay 1967). The pegmatite has a higher competency relative to the quartz-feldspar gneiss host; the quartz-feldspar gneiss typically flows into the tight hinge zones. Most inner arcs of folds are in the form of sharp cuspates, whilst the outer arcs are angular to subrounded. As an example, at locality 0074, the outcrop allowed for 3-dimensional observations and axial planar surface bearings (Fig. 16). The axial plane of the F_2 veins at this locality are orientated 256/81, parallel to the F_3 axial trace. Nearby at locality 0077, the isoclinal F_2 folds (outlined by coarse pegmatite) are recumbent (Fig. 17). A small (~10 cm), open F_3 fold is interpreted from a bulge in the limb of the recumbent F_2 pegmatite.

Younger folds, belonging to F_3, are often too large, with a broad, rounded curvature to be interpreted directly from outcrop, however certain localities reserve exception. At locality 0050C, an F_3 limb and hinge are preserved in a several-metre large quartz-feldspar and sillimanite-bearing quartz-feldspar gneiss (Fig. 19). The upright, tight to isoclinal F_2 folds are refolded during D_3, after which some F_2 folds are upright, whilst others are recumbent. The F_3 is an open fold with a rounded hinge (purple line).

The geometry of the major and the minor F_3 hinge zones, located northeast of Säm and in Torsgården respectively, is interpreted after the structure maps and stereonets. Both stereonets (C & D) concerning the F_3 phase are in agreement; the major and the minor F_3 folds are open with an interlimb angle of ~100°, have steeply dipping NE-SW striking axial planes, and have fold hinges orientated 30/036. The F_3 folds are classified as Class 1C folds (Ramsay 1967), because the curvature of the outer arc is less than the curvature of the inner arc of the fold.

In many places the F_2 folds align parallel with the S_3 axial plane (e.g. localities 0001, 0074, & 0105B; Figs 8A, 16 & 14A). The upright, tight to isoclinal F_2 folds at locality 0001 were further compressed during D_3, hence these are classified as Type 0 interference fold patterns. Therefore, these small folds are both F_2 and F_3 folds. The major F_2 fold hinge zone in Gammelgård is orientated parallel with the minor F_2 // F_3 folds at locality 0001, and with the major F_3 fold around the village of Säm.

4.2.3.4 Anatectic melting and associated structures

All units throughout the study area experienced partial melting. The grey garnet-poor and the darker garnet amphibolite best display the colour contrasts between the lighter leucocratic tonalite-trondhjemite veins and the darker melanocratic minerals.

Short, centimetre to decimetre, parallel-trending leucocratic veinlets are found at numerous localities around Säm (Fig. 20A). At locality 0095B, the veinlets are orientated ~13/038, which is axial-planar to F_3 folds.

En-échelon extension gashes were identified at locality 0033B (Fig. 20B). This garnet amphibolite has two generations of S-shaped tonalitic-trondhjemitic leucosomes. A primary set has been rotated during deformation, whilst the second set is aligned in accordance with the ISA and is superpositioned on the preexisting primary set. Shear-sense is sinistral; top-to-the west. Another example is shown in the garnet-poor amphibolite (Fig. 21).

Small, isolated, patch melts and isoclinal folds (Type 0 interference fold pattern) at locality 0033B showed that the plagioclase crystallographic cleavages appeared to have aligned subparallel with the S_2 // S_3 (~043°; Fig. 22A & B).

Single, competent layers that are disrupted and separated into elongate "sausage-like" segments are termed boudins (Ramberg 1955). Disruptions resulting from planar fracturing into rectangular segments are known as torn boudins, whilst pinched and swelled segments formed by necking are known as drawn boudins (Goscombe et al. 2004). Drawn boudins in association with foliation boudinage structures (Fig. 23) are found in the migmatized garnet amphibolite at localities 0026B & 0103 (Figs. 24 & 25 respectively). The stromatic migmatite structures are defined with numerous thin and laterally extensive leucosome bands trending parallel to the gneissic banding. Net structures are two or more systematic planar melt sets creating a 3-dimensional melt framework formed similarly as foliation boudinage structures

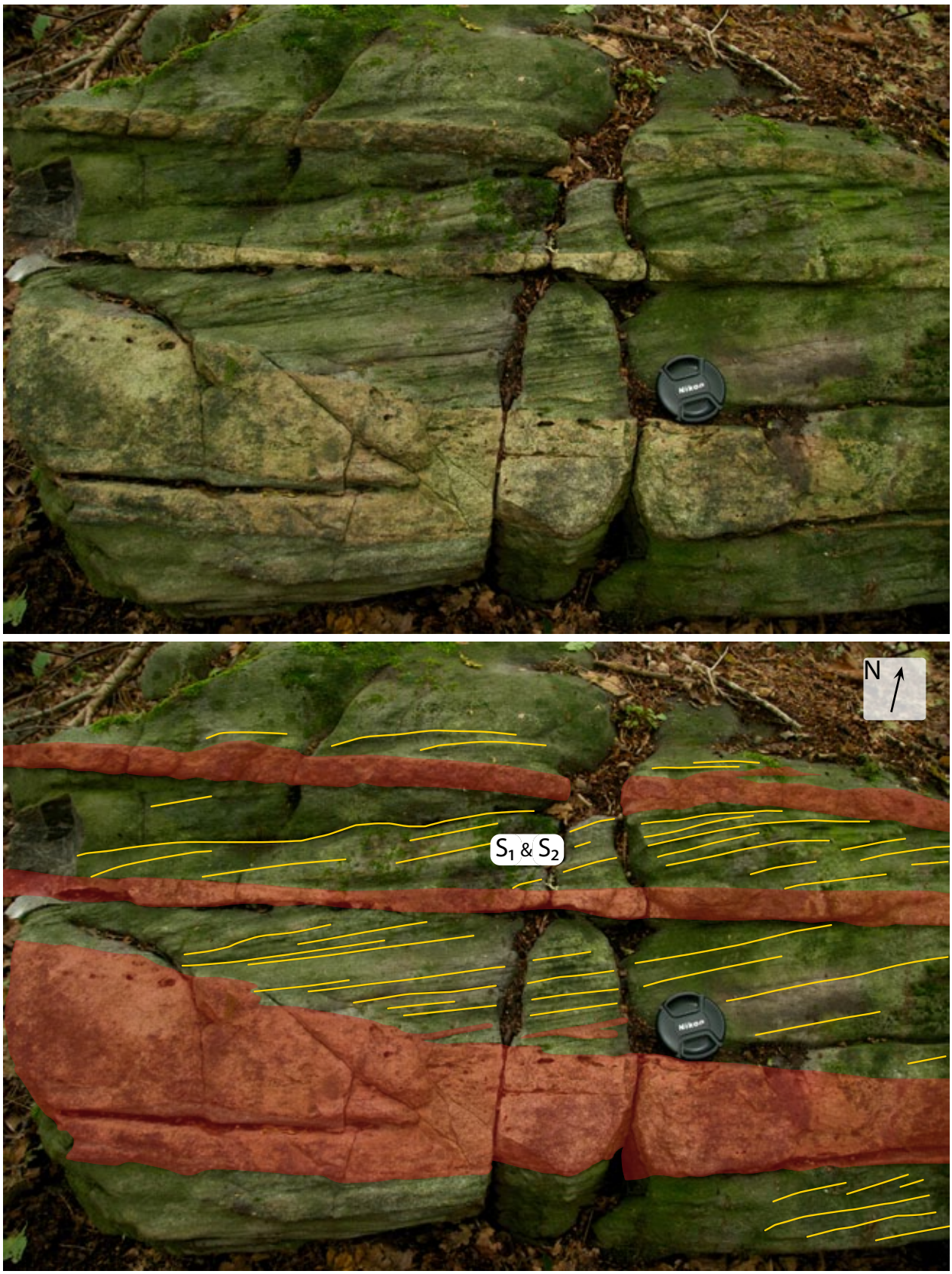

Fig. 12. Located along an east-west trending F_3 limb, locality 0062A is an inclined surface of a fine-grained aplite dyke crosscutting a well-foliated granodiorite gneiss. The foliations do not appear to create flanking folds against the intrusive dyke surface. There also appears to be a "chilled margin" contact between the aplite and the host, suggesting significant cooling of the granodiorite gneiss occurred before the discordant intrusion. Lens cap (74 mm) for scale.

Fig. 13. A well foliated quartz-feldspar gneiss with intrusive, crosscutting parallel to foliation mafic dykes, at the south-facing locality 0049B. It is not well understood if these are multiple repeat injection dykes creating a lit-par-lit feature, or perhaps this is one or two parallel dykes that were deformed into stretched out, recumbent isoclinal folds (sheath folds). Structurally situated below this locality lies a garnet-rich amphibolite tectonic lens. This is the northernmost study locality. Hammer (330 mm) for scale.

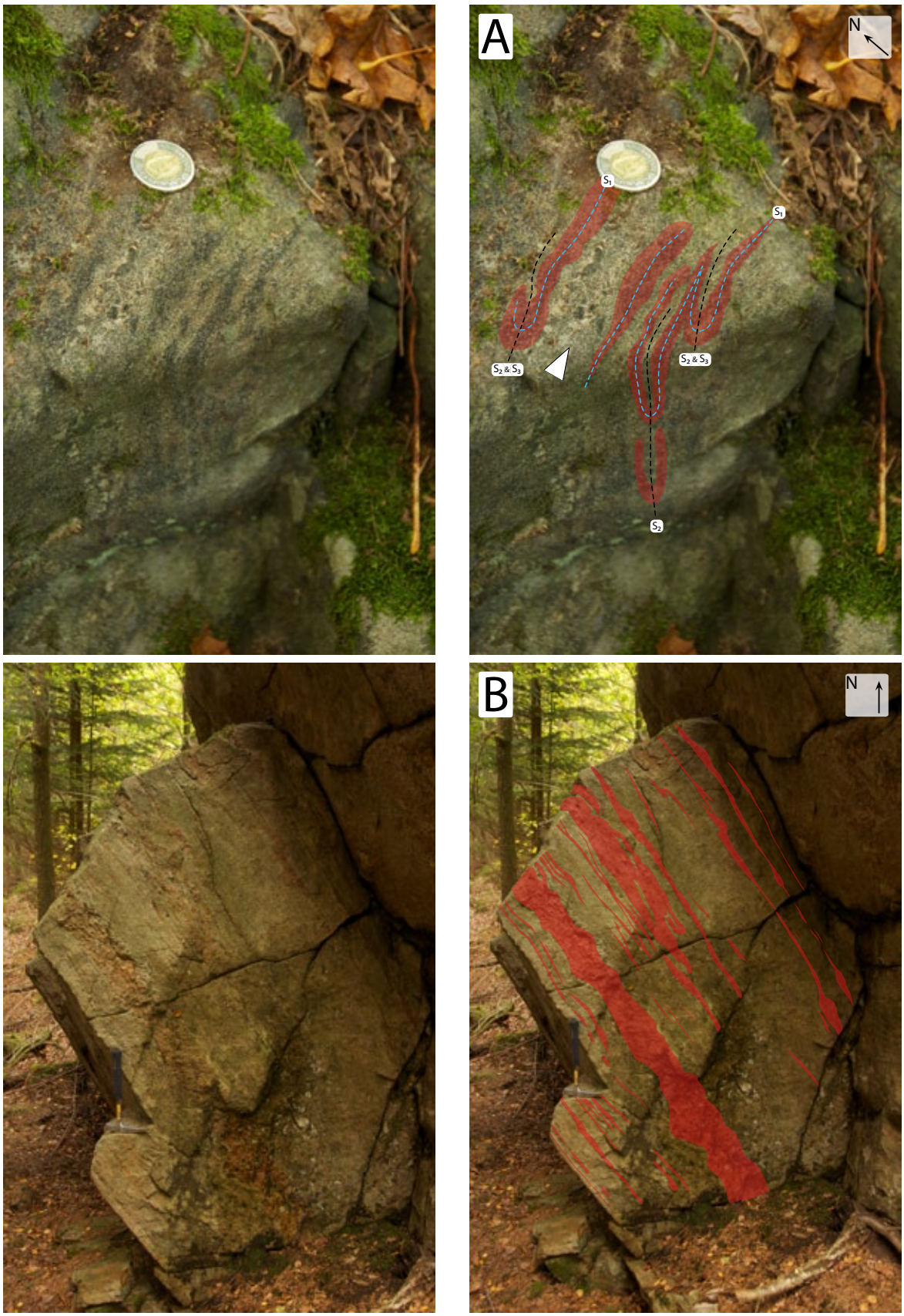

Fig. 14. (*A*) Horizontal and oblique vertical surfaces transecting upright isoclinal folds (234/82) composed of mafic minerals in a migmatized garnet-poor amphibolite lens in the F_3 & F_2 fold hinge at 0105B. This F_3 // F_2 fold hinge zone is tightly compressed, limiting space for rocks to flow. The melanosomes are stretched out and boudinaged. The diffuse nebulite melt domains often contain larger forest-green clinopyroxenes (white arrow) surrounded by plagioclase ± quartz. Coin (28 mm) for scale. (*B*) Pegmatite veins along a north striking, foliated, fine-grained quartz-feldspar gneiss at locality 0099A. The veins are tightly folded (F_2), as well as thinned out and boudinaged parallel to the axial surface (S_2). The host quartz-feldspar gneiss cleaves into massive meter-thick blocks. Hammer (330 mm) for scale.

Fig. 15. Detailed close-up of the folded pegmatite veins in the fine-grained quartz-feldspar gneiss along a vertical southeast-facing surface at locality 0082B. The gneissic (S_1), relatively coarser-grained, pegmatites have been elongated, boudinaged and folded into inclined isoclinal folds (F_2) during D_2. The F_2 axial surfaces (S_2) are roughly parallel with the S_1 fabric. A suitable surface to orientate the S_2 planes was not found at this locality. Coin (28 mm) for scale.

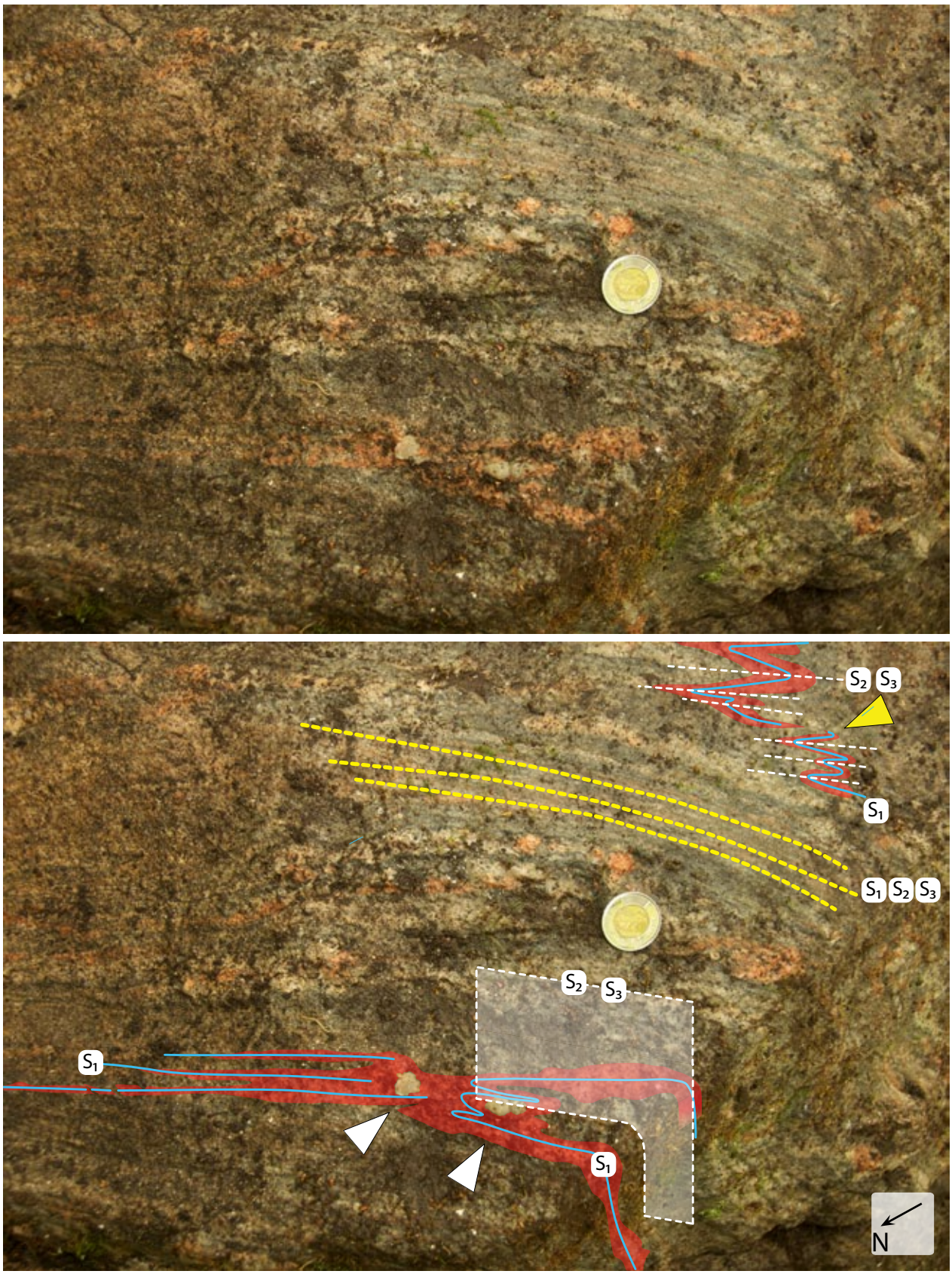

Fig. 16. A horizontal and vertical cut outcrop of pegmatite veins in the quartz-feldspar gneiss folded into F_2 at locality 0074. The axial planes of the F_2 veins (S_2; white plane) are orientated 256/81. The F_2 axial planes (S_2) follow parallel to the major F_3 axial plane (S_3). White arrows draw attention to the larger recrystallized quartz nodules located in the low-stain hinge zones. The pegmatite has a higher competency relative to the quartz-feldspar gneiss host; the quartz-feldspar gneiss flows into the tight hinge zones. Most outer arcs of the folds are in the form of sharp cuspates, whilst the inner arcs are angular to subrounded. Boudinage occurs at the inflection point along the limb between two hinge zones (yellow arrow). Coin (28 mm) for scale.

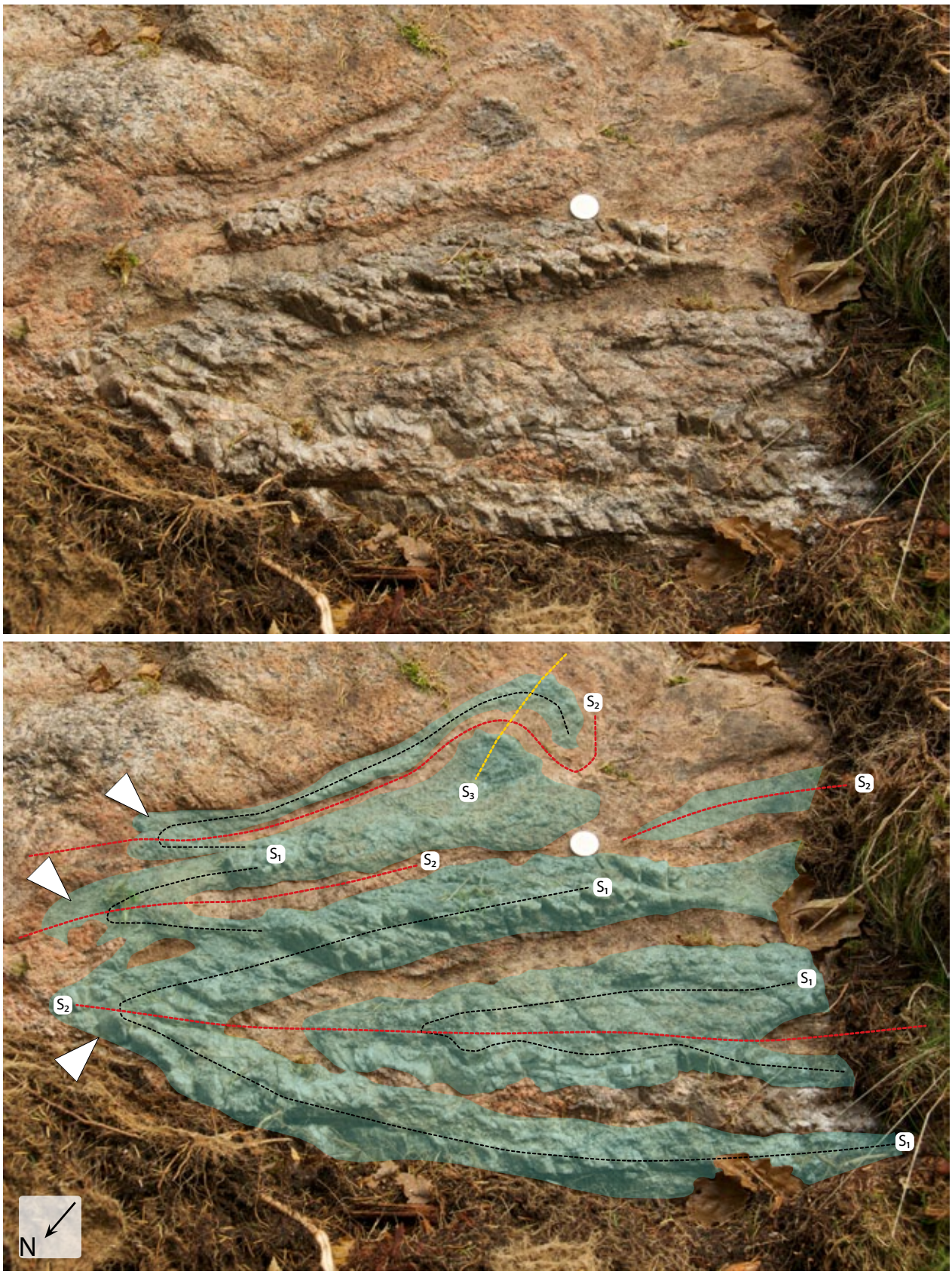

Fig. 17. Inclined surface of an F_2 folded coarse pegmatite veins in a finer-grain quartz-feldspar gneiss host along a roughly east-west trending major F_3 limb at locality 0077A. Although this is an oblique cross-section through the F_2 fold, hinge thickening and limb thinning in these recumbent isoclinal folds is apparent, the hinge-zones are narrow, and resemble to the Class 2 similar folds after Ramsay (1967). The white arrows point to the multiple folds stacked one on top of another. A small ~10 cm F_3 buckle fold is interpreted along the upper F_2 fold. Coin (28 mm) for scale.

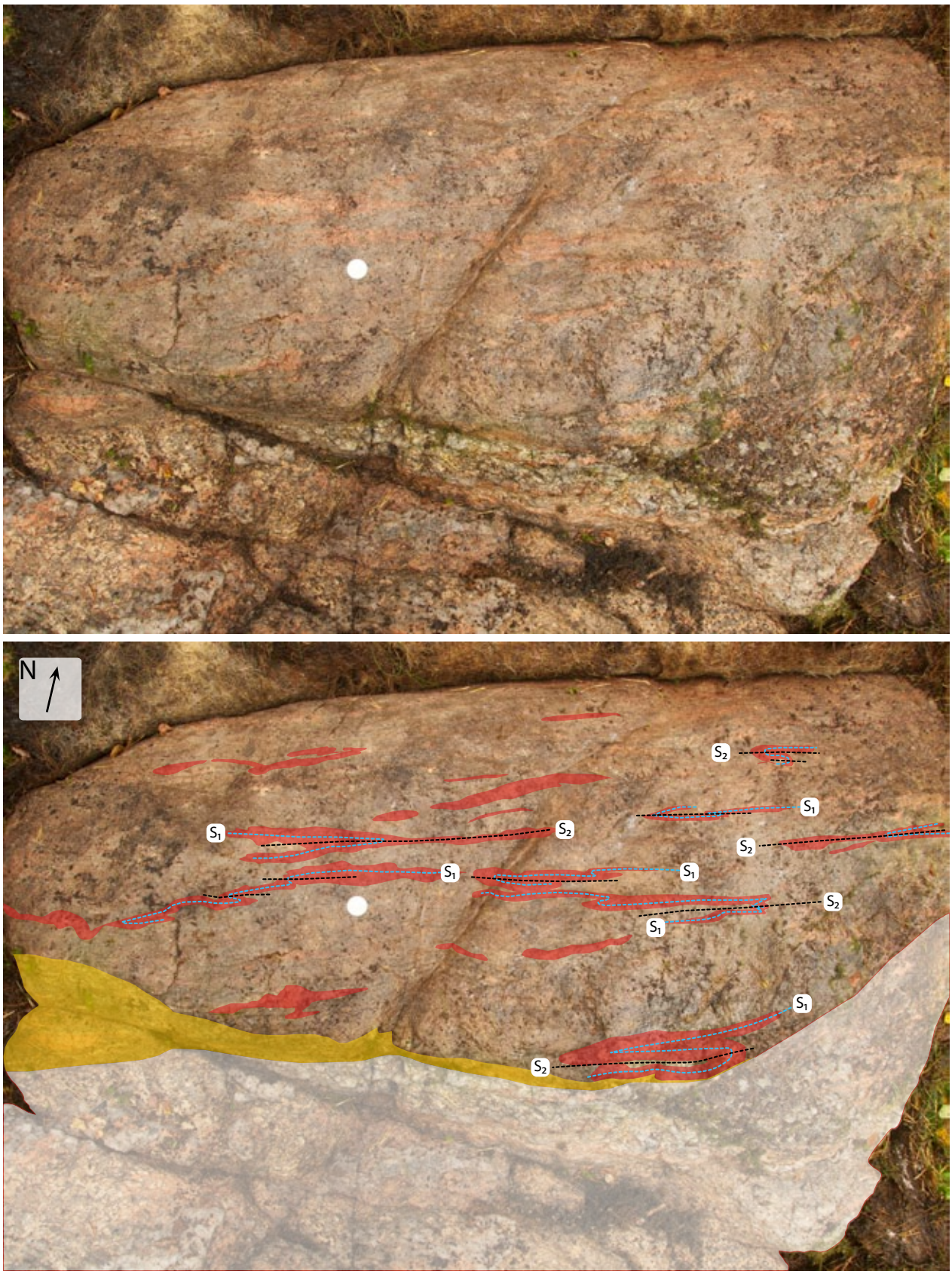

Fig. 18. A wet, inclined surface at locality 0076, along an east-west trending F_3 fold limb. A small shear zone (yellow) marks the boundary between the coarse pegmatite and the folded, fine-grained, quartz-feldspar gneiss; shear-sense is undetermined. The lower, coarse pegmatite body, shaded in white, does not display folds as at 0077A (Fig. 17), however these recrystallized coarse K-feldspar and quartz crystals show some strain. It is important to note that there are varying degrees of partial melting, and varying degrees of strain preserved in an outcrop. Attention is given to the thin, finer-grained pegmatite veins, shaded in red, that are isoclinally fold, and have their fold traces aligned parallel (azimuth: 054°) with the regional S_3. These small folds appear most similar in shape to the ones observed at localities 0099A (Fig 14B) and 0082B (Fig. 15). Coin (28 mm) for scale.

Fig. 19. Two distinct folds sets in a south facing quartz-feldspar gneiss at locality 0050C. The S_1 foliations, defined by the pegmatite veins, are deformed during D_2 to form upright, tight to isoclinal F_2 folds. The subsequent D_3 refolded the F_2, which led to some F_2 folds being upright, whilst others are recumbent in the F_3. Pegmatitic material pinched, swelled, and boudinaged during ductile deformation. The F_3 is defined as a NE-plunging, open Class 1C fold. The orientation for the S_3 at this locality is tentative, because there is only one F_3 limb and a partial F_3 hinge. Coin (28 mm) for scale.

(Arslan et al. 2008). The two melt sets may occur at angles perpendicular or oblique to each other. The shorter set of leucosome, at high angle to the stromatic one, defines the inter-boudin surface (S_{ib}; after Goscombe et al. 2004), and may form curved geometries reflecting crescent-double cresent-type and/or X-type boudin necks (Fig. 23; Guernina & Sawyer 2003; Arslan et al. 2008). Intersections between the melt sets outline and define the margins for lozenge-shaped and/or polygonal-shaped melanocratic drawn-boudins. At locality 0026B (Fig. 24), S_2 gneissic layering is often deflected towards these boudin necks, creating flanking folds (after Arslan et al. 2008). Locality 0103 shows a vertical surface orientated roughly perpendicular to the F_2 // F_3 fold axis of the garnet amphibolite (Fig. 25). A network of inclined, planar boudin necks are bounded by horizontal, planar stromatic leucosomes. Higher angled boudin necks are the thickest leucosomes and are connected to slightly thinner stromatic leucosomes. Single, disconnected stromatic leucosomes are also the thinnest leucosomes.

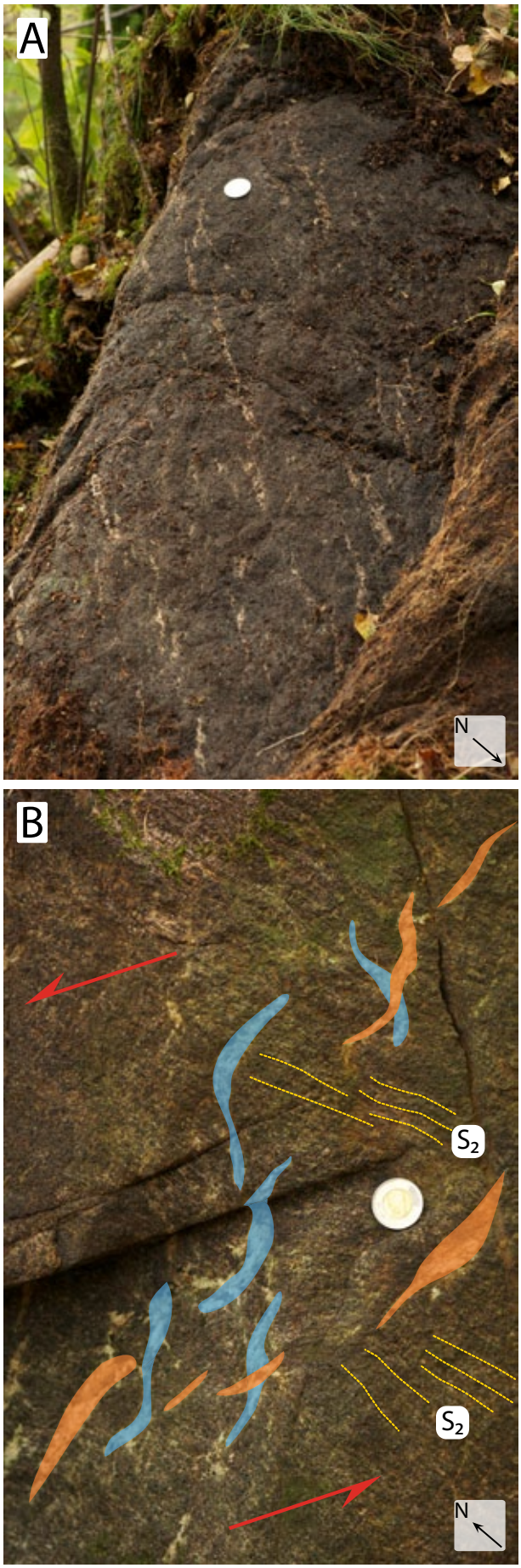

Fig. 20. (*A*) Short, centimetre to decimetre, parallel-trending leucocratic veinlets at locality 0095B, are orientated ~13/038. They trend roughly parallel to the F_3 fold axis. (*B*) Along a south-facing vertical outcrop at locality 0033B, a sigmoidal, en-échelon extension vein array is found in a garnet amphibolite. Shear-sense is sinistral. Foliations in the amphibolite (yellow lines) intersect the tonalitic veins at high angle, and it is parallel along these foliations that the anatectic melt migrated into the lower pressure dilation sites. Coin (28 mm) for scale.

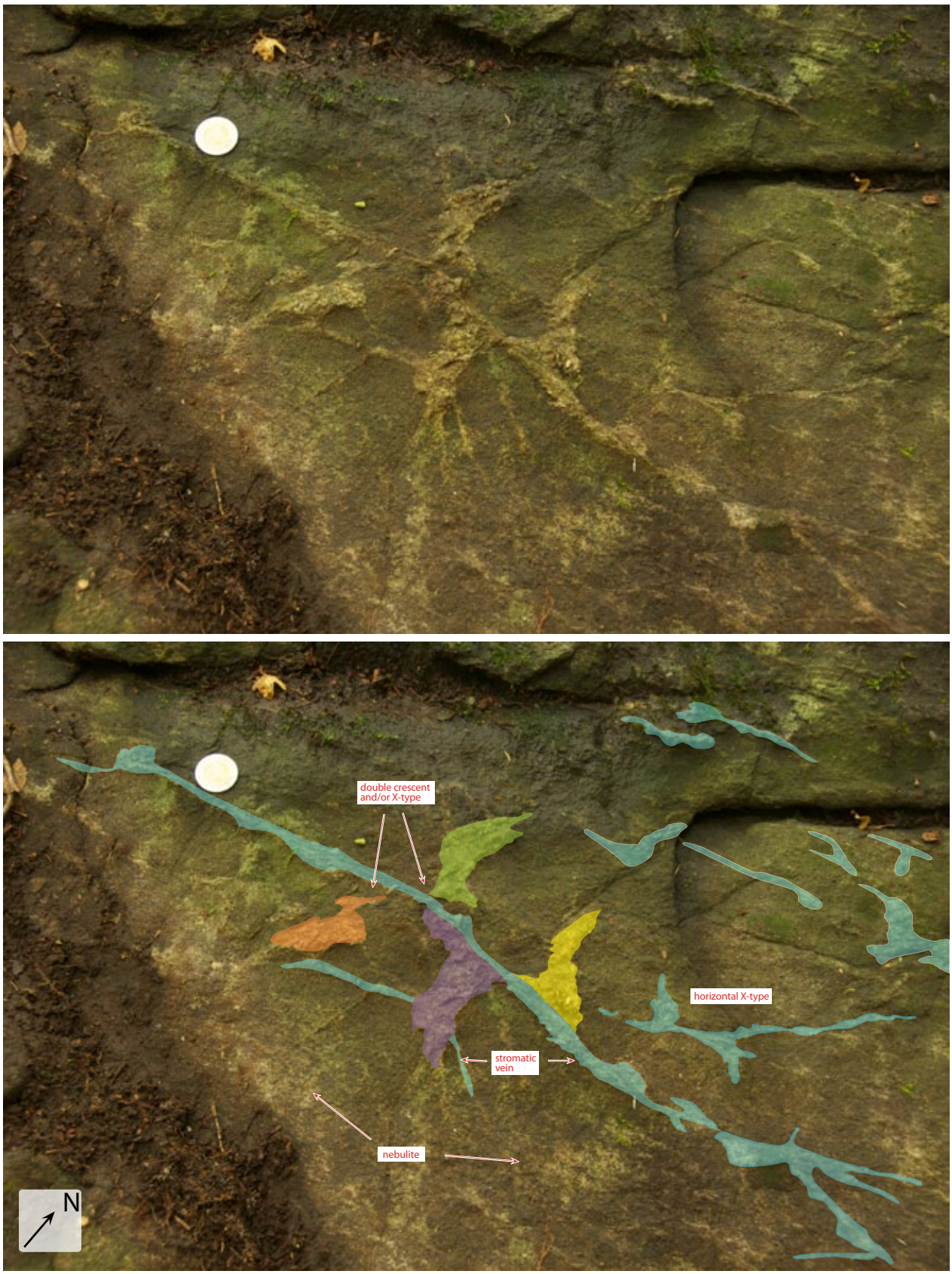

Fig. 21. Along an inclined surface at locality 0068C, leucocratic tension gashes (or foliation boudinage structures) with a bisecting stromatic vein are found in a garnet-poor amphibolite. As this is not a *XY*-section, the precise geometry of the tension gashes (or foliation boudinage structures) is not certain. The leucosome is well segregated in these dilation migmatites; sometimes a thin hornblende selvedge marks the border between the leucosome and the mesosome. Surrounding these dilation veins are diffuse nebulite structures with a poorly segregated neosome. Coin (28 mm) for scale.

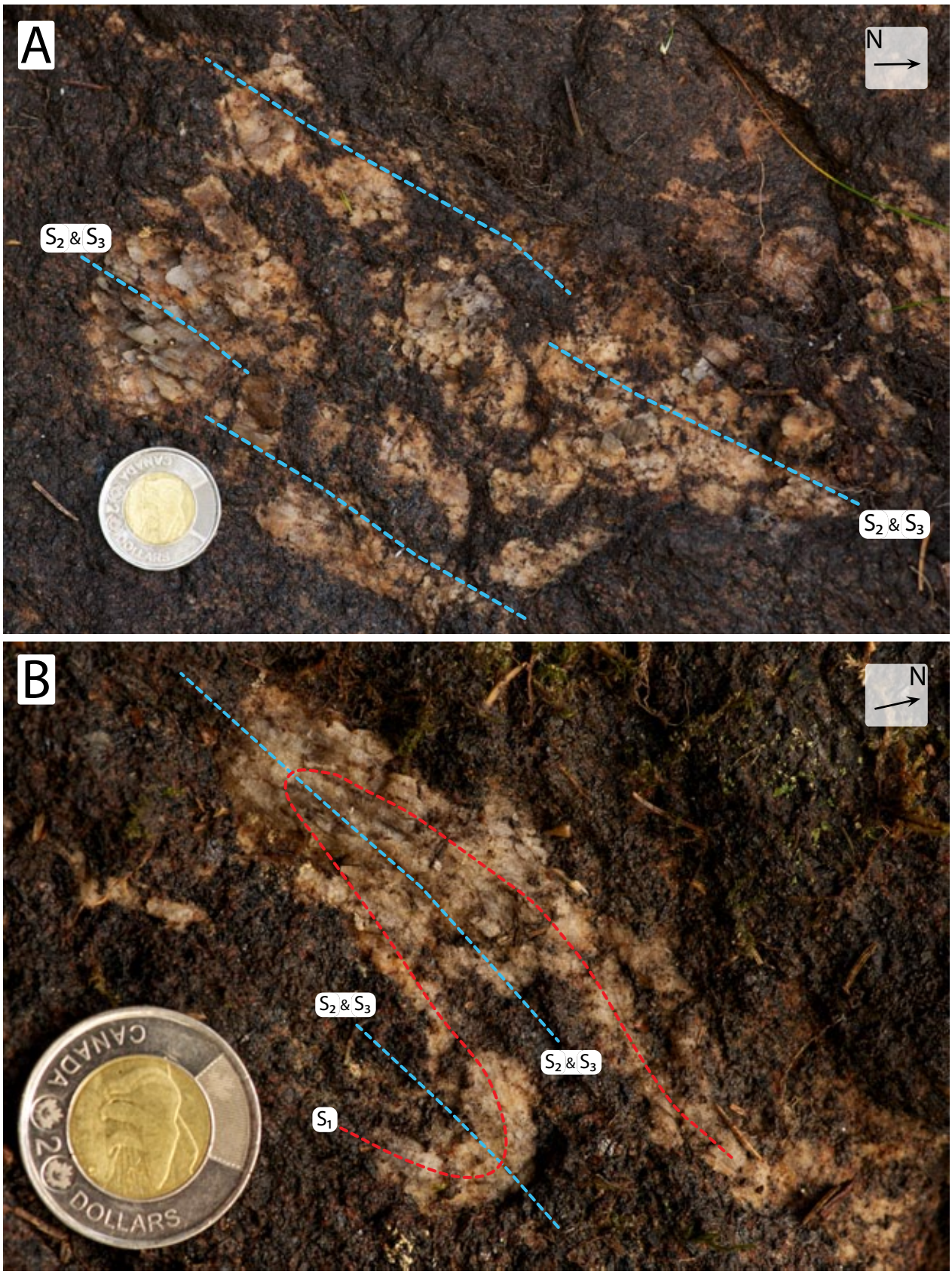

Fig. 22. Migmatites on a wet horizontal surface at locality 0033B. The migmatite is distinctly segregated into the respective tonalitic-trondhjemitic leucosome and pyroxene & amphibole-rich melanosome domains. Coin (28 mm) for scale. (*A*) A patch melt or an oblique surface through interference folds. Plagioclase crystallographic cleavages appear to have aligned subparallel with the S_2 // S_3. It is uncertain from the field if this is new crystal growth or transposition of a leucosome. (*B*) Another close-up, this time of an isoclinal folded (Type 0 interference fold pattern). Again, the coarse leucosome's elongated crystals are subparallel to the axial surface (S_2 // S_3; azimuth ~043°). Melt migrated from high-strain zones along the limbs towards low-strain, dilatent regions such as the hinge zones; limb-thinning and hinge-thickening.

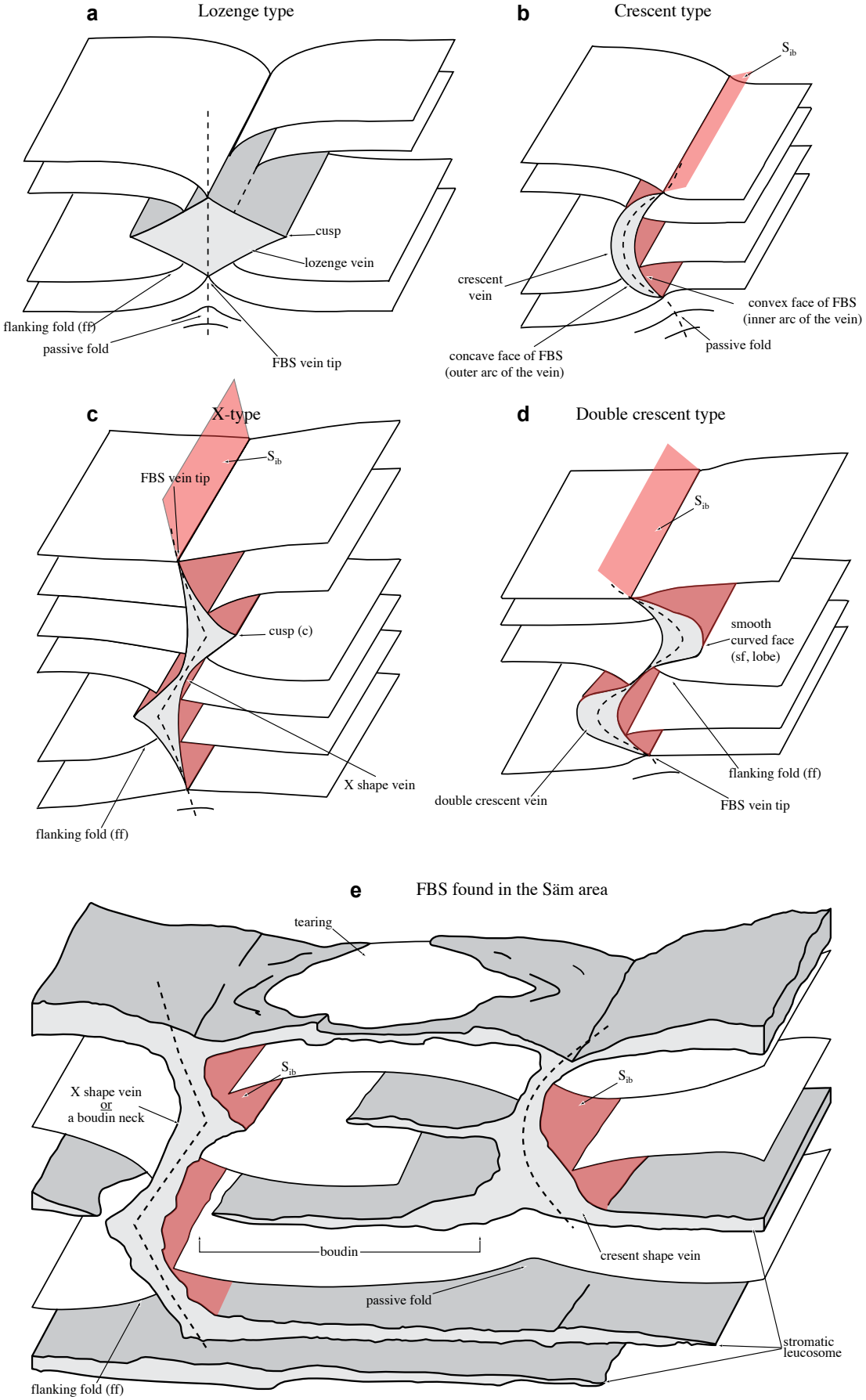

Fig. 23. (*A* to *D*) Idealized geometry and classification of foliation boudinage structures (FBS; Modified after Arslan et al. 2008). (*E*) A realistic block diagram of the foliation boudinage structures interpreted in the Säm area.

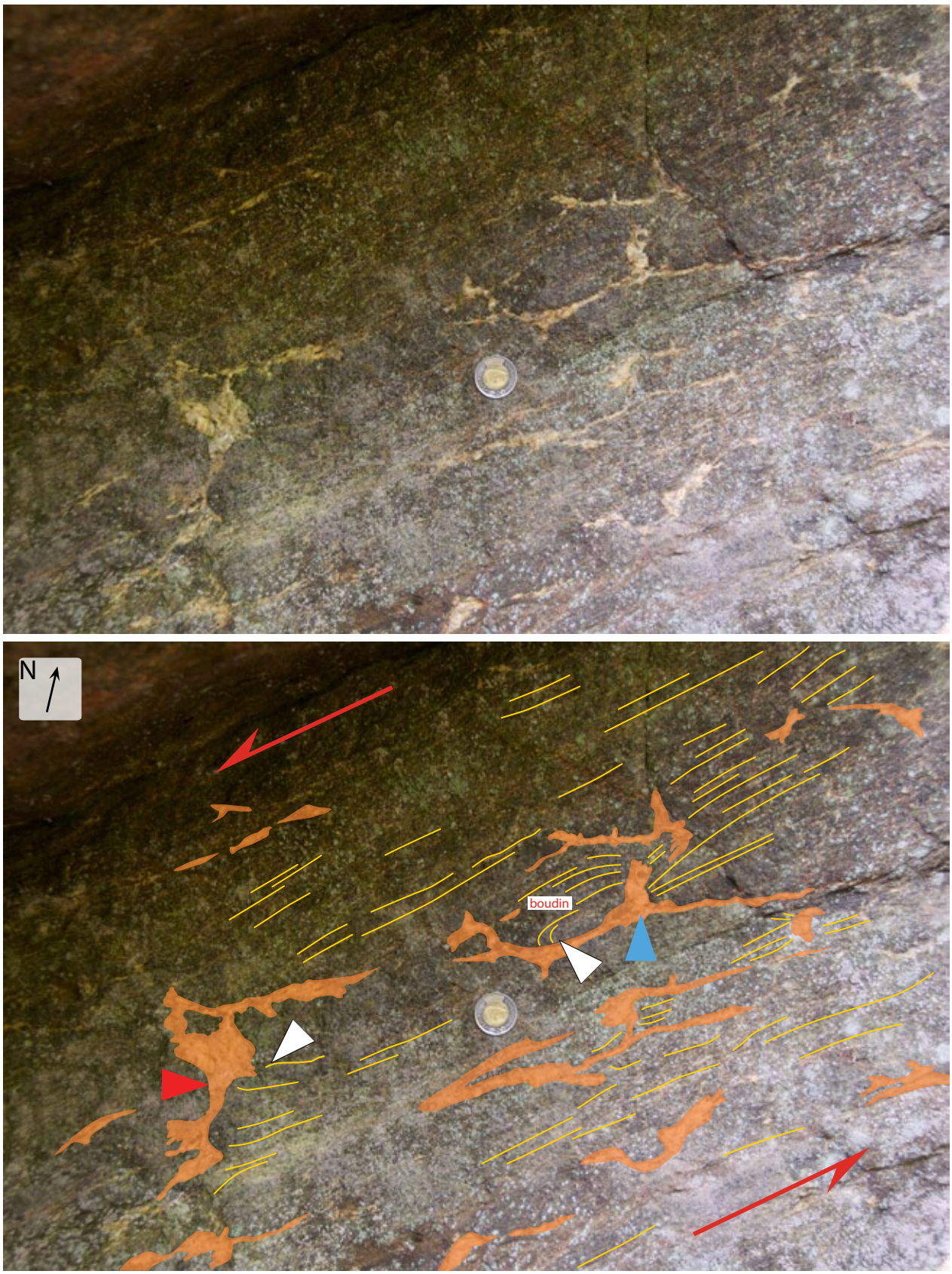

Fig. 24. Locality 0026B is a southern facing garnet amphibolite outcrop near the F_3 hinge zone. This vertical surface is nearly perpendicular to the gneissic foliation which is also nearly normal to the strain ellipsoid. Stromatic migmatites orientate roughly parallel to the gneissic foliation. Perpendicular to the stromatic leucosomes, are the boudin neck veins. These boudin necks are interpreted as X-type (red arrow) and crescent-type (blue arrow). These boudin necks crosscut the foliation and connect with the parallel melts thus creating the lozenge or polygonal shaped melanosomes (boudins). Near the vertical margins of these polygonal melanosomes, the gneissic foliation curves gradually inward, forming flanking folds (white arrow). Shear-sense is top-to-the-west. Coin (28 mm) for scale.

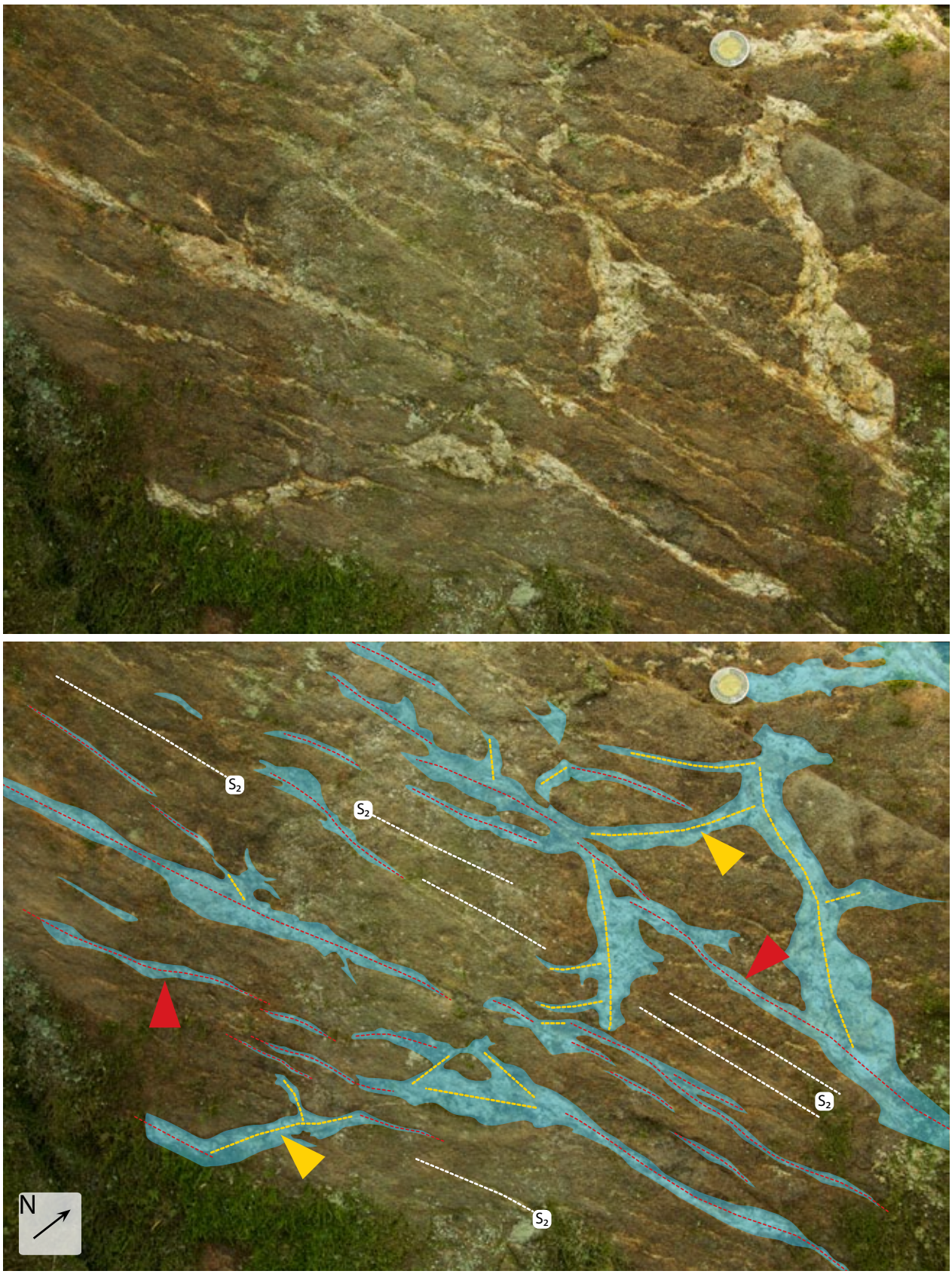

Fig. 25. This is a small vertical, southeasterly-facing surface at 0103A, which is part of a large, tightly folded amphibolite lens near the F_2 // F_3 hinge. The gneissic foliation here is not very well defined in comparison to 0026B, however the metatextite's net structure shown here displays a more connected leucosome network; distinct horizontal stromatic leucosomes and oblique boudin necks / foliation boudinage structures. Coin (28 mm) for scale.

4.3 Petrography including microstructures & mineral chemistry

The present description focuses on the garnet amphibolite, the garnet-poor amphibolite and the sillimanite-bearing quartz-feldspar gneiss from Säm. Less detailed petrographic descriptions are given for the quartz-feldspar gneiss and the intrusive dykes. A general mineralogy overview is provided in Table 1.

4.3.1 Garnet-poor amphibolite

Macroscopic appearance

The garnet-poor amphibolite is a light grey rock dominated by plagioclase and amphibole. Anatectic partial melting is widespread and the leucosome is uneven-grained (coarse- to fine-grained). Partially recrystallized, subhedral, bluish grey plagioclase, megacrysts (~5 mm), occur in the leucosome (Fig. 4A) with clinopyroxene and amphibole megacrysts (>5 mm). The plagioclase megacrysts do not show a distinctly preferred orientation. In contrast, the finer-grained recrystallized minerals commonly align to form lineations and folds. Garnet is rare, but is locally present next to leucosomes, around clinopyroxene or amphibole megacrysts (Fig. 26A).

Microtextures (polarized microscopy and SEM)

The mesosome of the garnet-poor amphibolite is fine-grained, has a granoblastic texture, and is made up of

Table 1. Mineralogy of the Säm samples

locality	description	qtz	pl	kfs	opx	cpx	grt	am	bt	mus	sil	mnz	ap	ilm/hem	rt	other
SM12-0001	grt-poor amphibolite	x	x			x	x	x	x				x	x	x	
SM12-0002	grt-poor amphibolite	x	x			x	x	x	x			x	x	x		sericitization
SM12-0019 ‡	grt-poor amphibolite	x	x			x		x	x				x	x		calcite
SM12-0026A	grt amphibolite	x	x				x		x					x		
SM12-0026B ‡	grt amphibolite	x	x		x	x	x	x	x				x	x	x	
SM12-0032 ‡	sil-bearing qtz-kfs gneiss	x	x	x			x		x		x	x		x	x	
SM12-0033	grt amphibolite	x	x		x	x	x	x	x				x	x	x	
SM12-0046 ‡	mafic dyke	x	x	x	x	x	x		x					x	x	
SM12-0047	charnockitized felsic orthogneiss	x	x	x		x	x	x	x			x	x	x	x	
SM12-0048B	felsic orthogneiss	x	x	x					x			x		x		
SM12-0050	sil-bearing qtz-kfs gneiss	x	x	x			x		x	x	x	x		x	x	
SM12-0054	sil-bearing qtz-kfs gneiss	x	x	x			x		x	x	x	x		x	x	
SM12-0062	gneissic granodiorite crosscut by aplite dyke	x	x	x		x			x	x			x	x	x	
SM12-0077A	pegmatite in a qtz-kfs gneiss	x	x	x					x			x	x	x	x	
SM12-0077C	calc-silicate	x	x			x	x	x					x			titanite, epidote
SM12-0080	pegmatite in a qtz-kfs gneiss	x	x	x						x					x	
SM12-0086A	sil-bearing qtz-kfs gneiss	x	x	x			x		x	x	x	x				
SM12-0086B	grt-bearing tonalite	x	x	x			x		x			x				
SM12-0103	grt amphibolite	x	x		x	x	x	x	x				x	x	x	
SM12-0107B	grt amphibolite	x	x			x	x	x	x				x	x	x	
SM12-Q01	amphibolite	x	x	x		x		x	x	x		x	x	x		
SM12-Q02	tonalite leucosome	x	x					x	x			x	x	x		
SM12-Q03	qtz-kfs gneiss	x	x	x				x	x				x	x		

‡ indicates localities with a thin section examined under SEM

hornblende and plagioclase (in approximately equal proportions) with lesser amounts of biotite and abundant small grains of opaque minerals. In some samples (eg. SM12-0001-01) plagioclase and dark minerals are separated in distinct aggregates. This particular sample shows an equant granoblastic plagioclase and quartz matrix surrounding highly cuspate hornblende and clinopyroxene clasts (blue arrow; Fig. 26B) . Minor phases include apatite and garnet. Garnet commonly forms irregular, fine-grained coronas around Fe-Ti oxide grains separated by a moat of plagioclase (Fig. 26C). The leucosome is made up of plagioclase and quartz, and contains variable amounts of 2-20 mm megacrysts of plagioclase, clinopyroxene and blue-green amphibole. In one thin section (SM12-0019) calcite and scapolite is present. Clinopyroxene form blasts with bleb-like inclusions of plagioclase (up to 30 vol. %) and small grains of opaques (Figs. 26C & D). In some clinopyroxene blasts, the opaque grains are aligned parallel with the host's crystallographic planes. Locally, amphibole has partially replaced clinopyroxene, in particular along grain boundaries and cleavages.

Mineral chemistry (sample SM12-0019)

All analyzed plagioclase grains have sodic-rich compositions of An_{30-35} (andesine; Table A2). Plagioclase is found with hemo-ilmenite inside clinopyroxenes (Fig 26C). Clinopyroxene is a sodium-bearing aluminum diopside (after Morimoto et al. 1988). Jadeite content is low (Jd_{3-5}) and x_{Mg} is 90-93 [x_{Mg} = (Mg/(Mg+Fe)) x 100]. Garnet is absent in the analyzed thin section. Amphibole is a calcic amphibole classified as tschermakite to magnesiohastingsite (after Leake et al. 1997; Hawthorne et al. 2012).

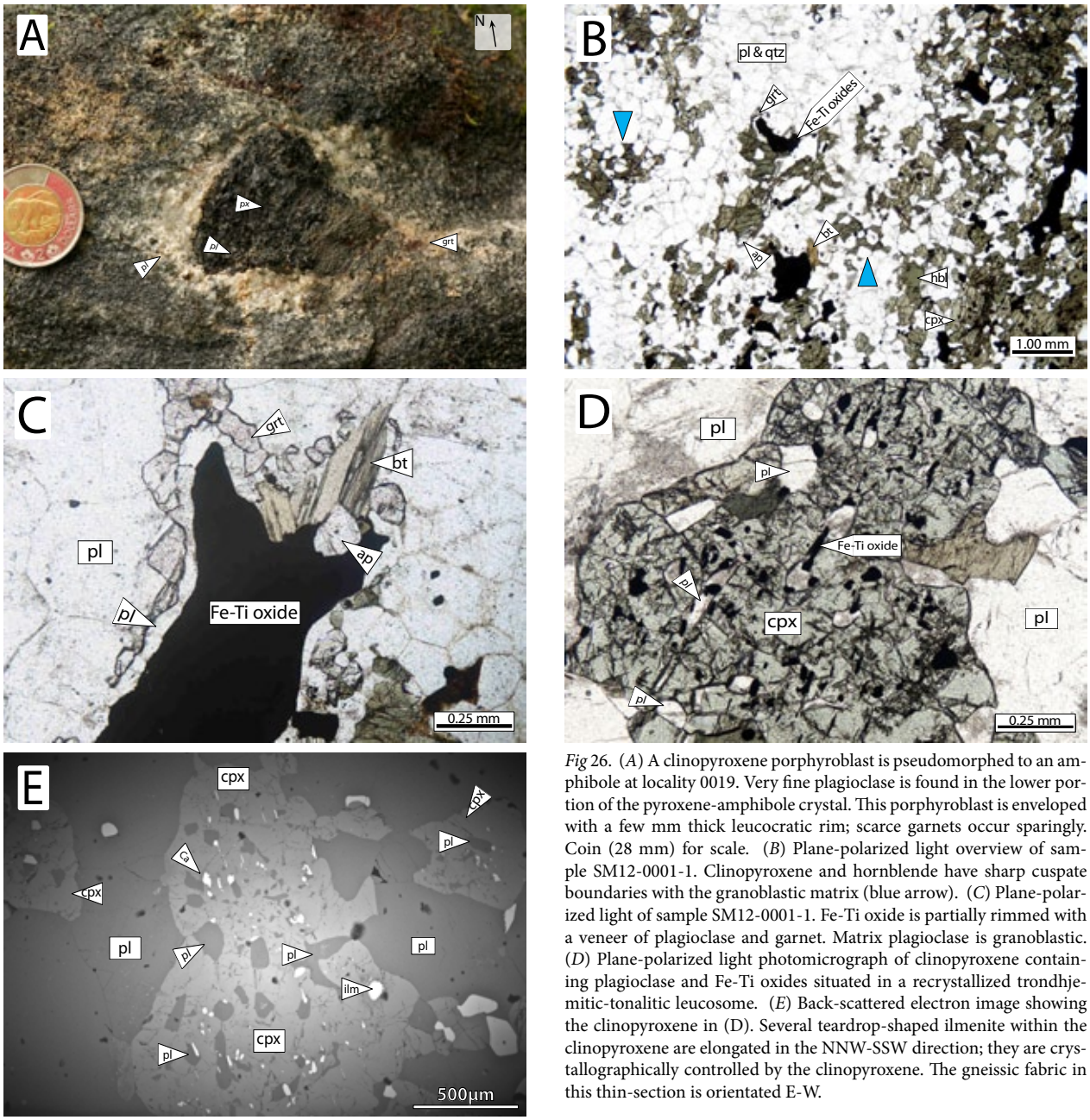

Fig 26. (*A*) A clinopyroxene porphyroblast is pseudomorphed to an amphibole at locality 0019. Very fine plagioclase is found in the lower portion of the pyroxene-amphibole crystal. This porphyroblast is enveloped with a few mm thick leucocratic rim; scarce garnets occur sparingly. Coin (28 mm) for scale. (*B*) Plane-polarized light overview of sample SM12-0001-1. Clinopyroxene and hornblende have sharp cuspate boundaries with the granoblastic matrix (blue arrow). (*C*) Plane-polarized light of sample SM12-0001-1. Fe-Ti oxide is partially rimmed with a veneer of plagioclase and garnet. Matrix plagioclase is granoblastic. (*D*) Plane-polarized light photomicrograph of clinopyroxene containing plagioclase and Fe-Ti oxides situated in a recrystallized trondhjemitic-tonalitic leucosome. (*E*) Back-scattered electron image showing the clinopyroxene in (D). Several teardrop-shaped ilmenite within the clinopyroxene are elongated in the NNW-SSW direction; they are crystallographically controlled by the clinopyroxene. The gneissic fabric in this thin-section is orientated E-W.

4.3.2 Garnet amphibolite

Macroscopic appearance

Dark green to nearly black amphibolite streaked with plagioclase-dominated leucosome is widespread in the Säm area. Outcrops range in size from metre-size exposure to a hill several 100 m long and with significant elevation gain (20 to 30 m). Pyroxene + plagioclase + garnet + amphibole are easily spotted in hand sample. Pyroxene and amphibole grains in or around the coarse grained leucosomes measure up to centimetre-size. Garnet is typically <2-3 mm. Corona textures are relatively rare in the field, however they do exist (Fig. 27A).

Microtextures (polarized microscopy and SEM)

The mesosome of the garnet amphibolite is fine- to medium-grained, granoblastic, and consists of variable proportions of brownish green hornblende and clinopyroxene together with antiperthitic plagioclase, garnet, biotite, opaques, and locally minor orthopyroxene. Accessory minerals are apatite, zircon and rutile. The leucosome is medium- to coarse grained and made up of antipertihitic plagioclase and quartz. Locally, close to or within leucosome, clinopyroxene blasts contain bleb-like inclusions (30-40 vol. %) of plagioclase, opaques, orthopyroxene and hornblende These clinopyroxene and plagioclase intergrowths are generally rare microtextures, the best preserved is Figures 27B-E.

Occasionally coronas consisting of plagioclase and thin (~10-20 μm thick) orthopyroxene rims surround Fe-Ti oxides and/or clinopyroxene (Figs. 27F-G). Thin (~0.1 mm) plagioclase and quartz moats often shield garnet from contact with ortho- and clinopyroxene, however garnet has many mutual contacts with hornblende. Garnet is fine-grained (<1 mm), subidioblastic, and often fractured. Thin plagioclase and quartz rims form sharp cuspates with low- to high- "apparent" dihedral angles against solid grains (Fig. 27G-H). Quartz, abundant fine rutile ± ilmenite needles, some zircon grains and other undifferentiated needles are common inclusions in garnet. Much of the plagioclase in the leucosome is recrystallized however some crystals show undulatory-zoned extinction. Irregularly shaped antiperthite exsolution blebs within grains and very fine-grained myrmekite along grain boundaries are additional microtextures characterizing plagioclase in the leucosomes (Fig. 27G). Olive-green to light-green pleochroic hornblende is found along the margins of clinopyroxene. Some hornblende crystals show a well-defined 60°-120° cleavage. Foxy brown biotite is typically in contact with the Fe-Ti oxides, and forms randomly orientated crystals.

Mineral chemistry (sample SM12-0026B-1)

The plagioclase (An_{10-30}; oligoclase) intergrown with the clinopyroxene (Figs. 27B-E) is of similar An-composition to the coarse plagioclase in the surrounding leucosome (Table A3). Plagioclase from the leucosome showing zoned extinction are also compositionally zoned; core to rim profiles are An_{14-24} (Fig. 28A). Clinopyroxene is Ca-rich diopside (Morimoto et al. 1988) with jadeite (Jd_{2-4}) and x_{Mg} = 78-81. Orthopyroxene forming rims around ilmenite is enstatite (x_{Mg} = 59-65). Amphiboles are unzoned calcic-amphiboles with variable x_{Mg} (59-69); ferric iron varies. Garnets are generally almandine dominated (50-60 %), with pyrope (15-30 %), grossular (15-25 %) and minor spessartine (0-3 %). Larger grains (>0.5 mm) with minimal fractures surrounded by plagioclase and quartz were chosen for compositional profiles. Two compositional patterns are shown: the largest grains (>1 mm) are zoned whilst the smaller grains are unzoned. Zoned profiles display smooth increasing almandine and pyrope content synchronous with a smooth decreasing grossular content from core-rim (Fig. 28B). x_{Fe} and spessartine profiles remain relatively flat.

4.3.3 Felsic gneisses

The quartz-feldspar and the sillimanite-bearing quartz-feldspar gneisses have been mapped separately (Fig. 3). However sillimanite in many outcrops may be too fine-grained to observe in hand sample and a microscope is required for proper identification. In addition, these two units have been massively intruded by pegmatite dykes. All three felsic rocks have experienced similar deformation histories.

Fig. 27. (A) A pyroxene or amphibole porphyroblast (partially covered in wet soil) is mantled with pyroxene, garnet and plagioclase at locality 0029B in the garnet amphibolite unit. Garnet with pyroxene, amphibole and Fe-oxides are the main melanocratic minerals surrounding this mantled porphyroblast. Coin (28mm) for scale. (B-G) Microphotographs and back-scattered electron images showing representative microtextures in the garnet amphibolite. (*A-F*) are from sample SM12-0026B-1, (*G*) is from sample SM12-0107, and (*H*) is from sample SM12-0077C. (*B*) Plane-polarized light microphotograph representative of the overall mineralogy and textures seen in the garnet amphibolite. The mid to lower right-hand side of the image is the margin of a plagioclase-rich leuocosome. (*C*) Cross-polarized light microphotograph showing a clinopyroxene with plagioclase intergrowths, surrounded by a tonalitic-trondhjemitic leucosome. Top-left corner in the leucosome shows thin, tapered twins in a plagioclase crystal. (*D*) Back-scattered electron image of the clinopyroxene in (C) with plagioclase bleb-like intergrowths. Some intergrowths are elongate, whilst others are subrounded. (*E*) Detailed back-scattered electron image of the clinopyroxene and orthopyroxene amongst the intergrown plagioclase. Orthopyroxene contains a thinly striped texture along small micro-fractures (red arrow); this is *possibly* calcic-amphibole. Hemo-ilmenite has a zebra-print pattern. (*F*) Back-scattered electron image depicting a ilmenite grain with a hematite domain partially surrounded with an orthopyroxene rim. The orthopyroxene again contains the thinly striped texture (red arrows) along the margins and microfractures. (*G*) Plane-polarized light microphotograph of thin (~10-20 μm thick) orthopyroxene rims around Fe-Ti oxide and clinopyroxene. Irregularly shaped plagioclase and quartz with high surface to volume ratio fill in the pores between the mafic minerals. (*H*) Cross-polarized light photomicrograph of a plagioclase-rich leucosome in sample SM12-0033B showing remnants of a melt; blue arrows point to thin irregularly shaped quartz films, forming sharp cuspates around recrystallized plagioclase. Yellow arrows point to very fine-grained myrmekite along the boundary of a plagioclase with coarse-grained, vermicular, antiperthite exsolution (red arrow).

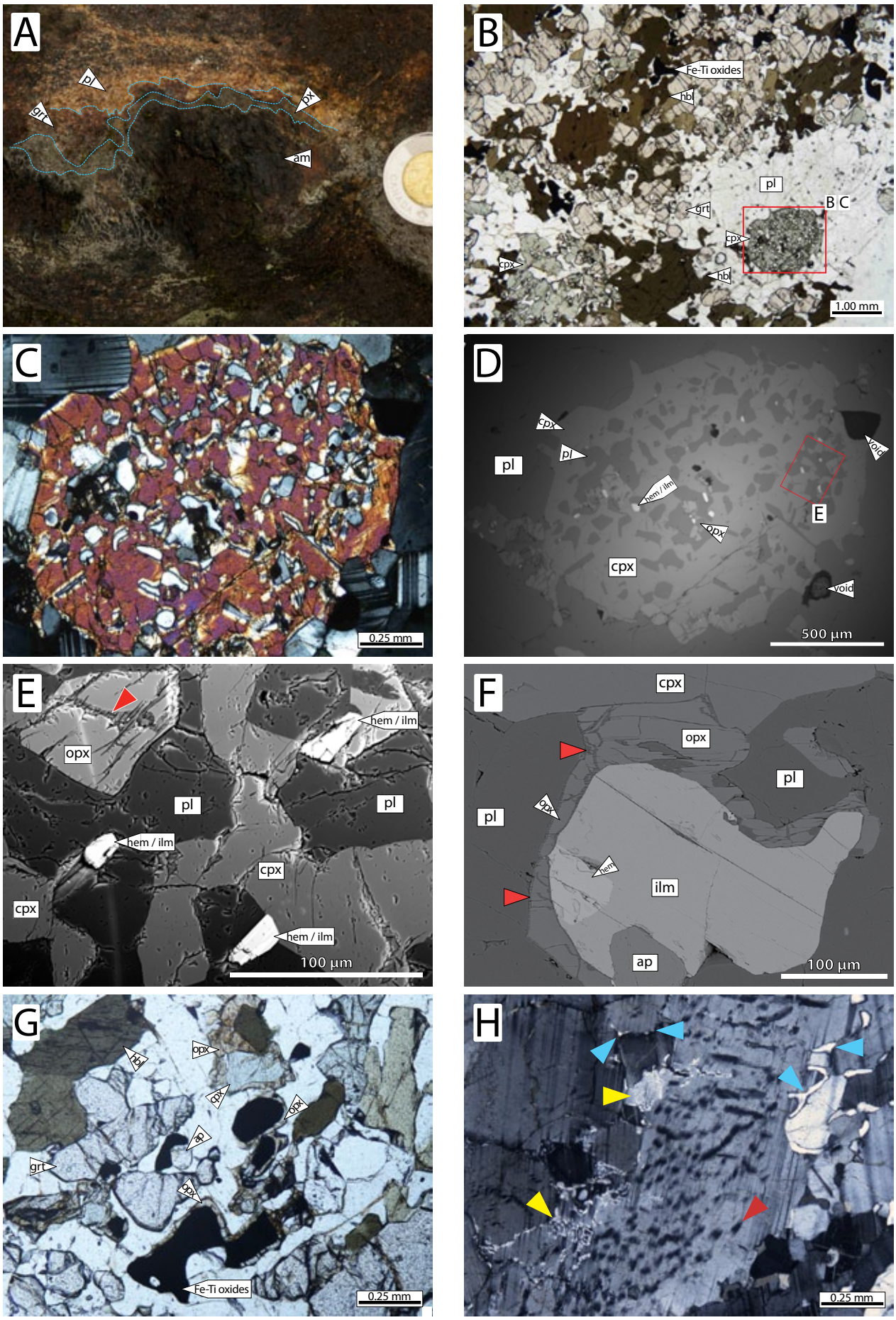
A
pl
grt
px
am
B
Fe-Ti oxides
hbl
pl
B C
grt
cpx
cpx
hbl
1.00 mm
C
0.25 mm
D
cpx
pl
pl
hem / ilm
void
E
opx
cpx
void
500 µm
E
hem / ilm
opx
pl
pl
hem / ilm
cpx
cpx
hem / ilm
100 µm
F
cpx
opx
pl
pl
opx
hem
ilm
ap
100 µm
G
hbl
opx
cpx
opx
ap
grt
opx
Fe-Ti oxides
0.25 mm
H
0.25 mm

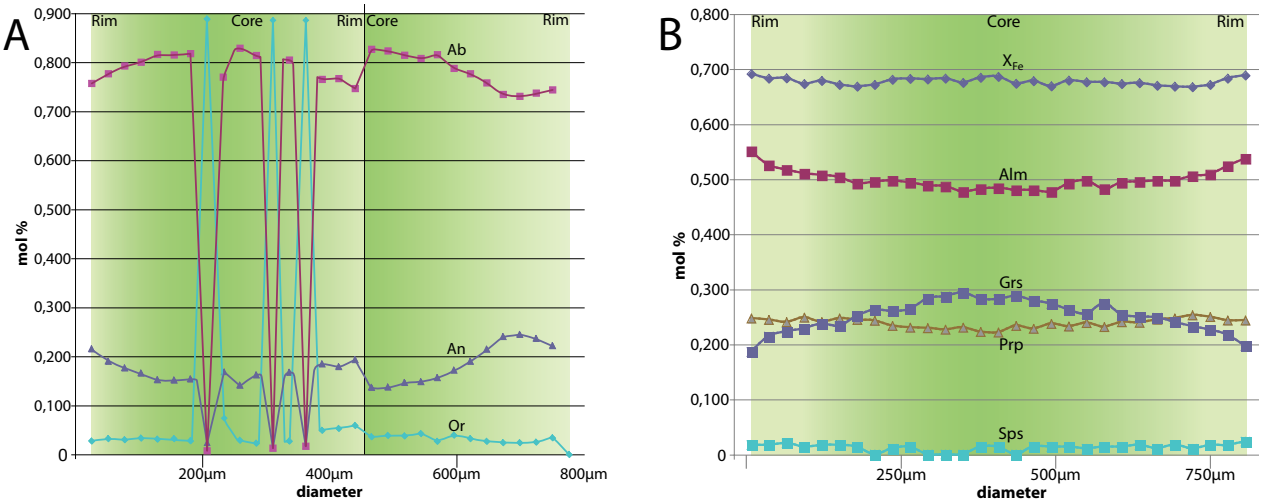

Fig. 28. Representative compositional profiles in sample SM12-0026B-1. (*A*) Profile through two zoned plagioclase crystals (one crystal is truncated) found in the leucosome of Fig. 27A. Antiperthitic exsolution lamellae are indicated by the breaks in the profiles. (*B*) Profile through a zoned, 800 µm garnet grain surrounded by plagioclase.

4.3.3.1 Quartz-feldspar gneiss

Macroscopic appearance

The major minerals composing the quartz-feldspar gneiss is quartz + K-feldspar ± plagioclase. Quartz may appear clear to smoky grey and form thin (<20 mm) elongate (centimetre-scale) ribbons. These ribbons tend to flow around the more competent K-feldspar porphyroclasts and augens (~10 mm; Fig. 4C). K-feldspar is generally pinkish-red whilst plagioclase is milky (on weathered surfaces), greyish-white. All outcrops are heterogeneously deformed and heterogeneously recrystallized (e.g. Figs. 9A, 10, 16, 17, 18).

Microtextures (polarized microscopy)

Quartz and K-feldspar are ubiquitous in thin section, with subordinate plagioclase. Biotite, hornblende, garnet, and Fe-Ti-oxide occur in varying amounts (Figs. 30A & B). Sillimanite is absent. Quartz forms long polycrystalline ribbons; quartz crystals within the ribbon form irregular grain boundaries and some show undulose extinction. Coarse porphyroclasts of K-feldspar generally show blebby, perthitic exsolution with undulose extinction and may be partially recrystallized along the grain margins. Very fine-grained, microcline with tartan twins (several with perthitic exsolution), plagioclase with polysynthetic twins, and quartz form the anhedral to euhedral, granoblastic matrix. K-feldspar and plagioclase are heterogeneously altered with late sericite.

There are several highly sheared localities in the Säm area (Figs. 10A & B). Thin sections were made from a mylonitic gneiss sample collected from the Valinge quarry (sample SM12-Q03; Fig. 30B). Thin (<2 mm) mylonites are characterized with sharp boundaries and strong, internal ductile deformation. Very thin (<0.1 mm), dark margins composed of biotite and an unidentifiable opaque material (white arrow), bound the strained-softened quartz from the recrystallized quartz, K-feldspar, and plagioclase granoblastic matrix. Strained quartz within the mylonitic microdomain is slightly to strongly elongate, very fine to *relatively* coarse grained, and is truncated by the dark horizontal bounding margins (white arrows) at ~20°. Undulose extinction and highly irregular, cuspate and lobate grain boundaries (grain boundary migration) also characterize the mylonitic quartz. Garnet, biotite, and hornblende are found in unstrained microdomains.

4.3.3.2 Sillimanite-bearing quartz-feldspar gneiss

Macroscopic appearance

Composed of quartz + K-feldspar + plagioclase + sillimanite + garnet + biotite. Fine- to medium-grained varieties with concordant, folded pegmatitic veins occurred at several localities (e.g. Fig. 16). A migmatized variety, which developed a parallel trending planar fabric, composed of millimetre-wide and centimetre- to several centimetre-long quartz ribbons with pink K-feldspars, milky grey plagioclase and yellowish sillimanite (Figs. 4D, 29A & B). Biotite and sillimanite are much too fine-grained in most outcrops and therefore rarely observed in the field. However there are excellent localities with long sillimanite prisms or faint yellowish streaks trend along thin foliations in highly sheared zones. They are differentiated in the field by means of colour from the elongated, clear-smoky, ribbon quartz and the recrystallized pink-greyish K-feldspars.

Microtextures (polarized microscopy and SEM)

The following minerals have been observed in thin section: quartz + K-feldspar (moderately to highly sericitized) + plagioclase + sillimanite + garnet + biotite ± cordierite (Fig. 30C). Fe-Ti oxide, Fe-sulphide, muscovite, rutile, and monazite are common accessory minerals. A small grain which may be kyanite has been found in one thin section. Quartz and K-feldspar are ubiquitous in all samples and show similar microstructures as in the

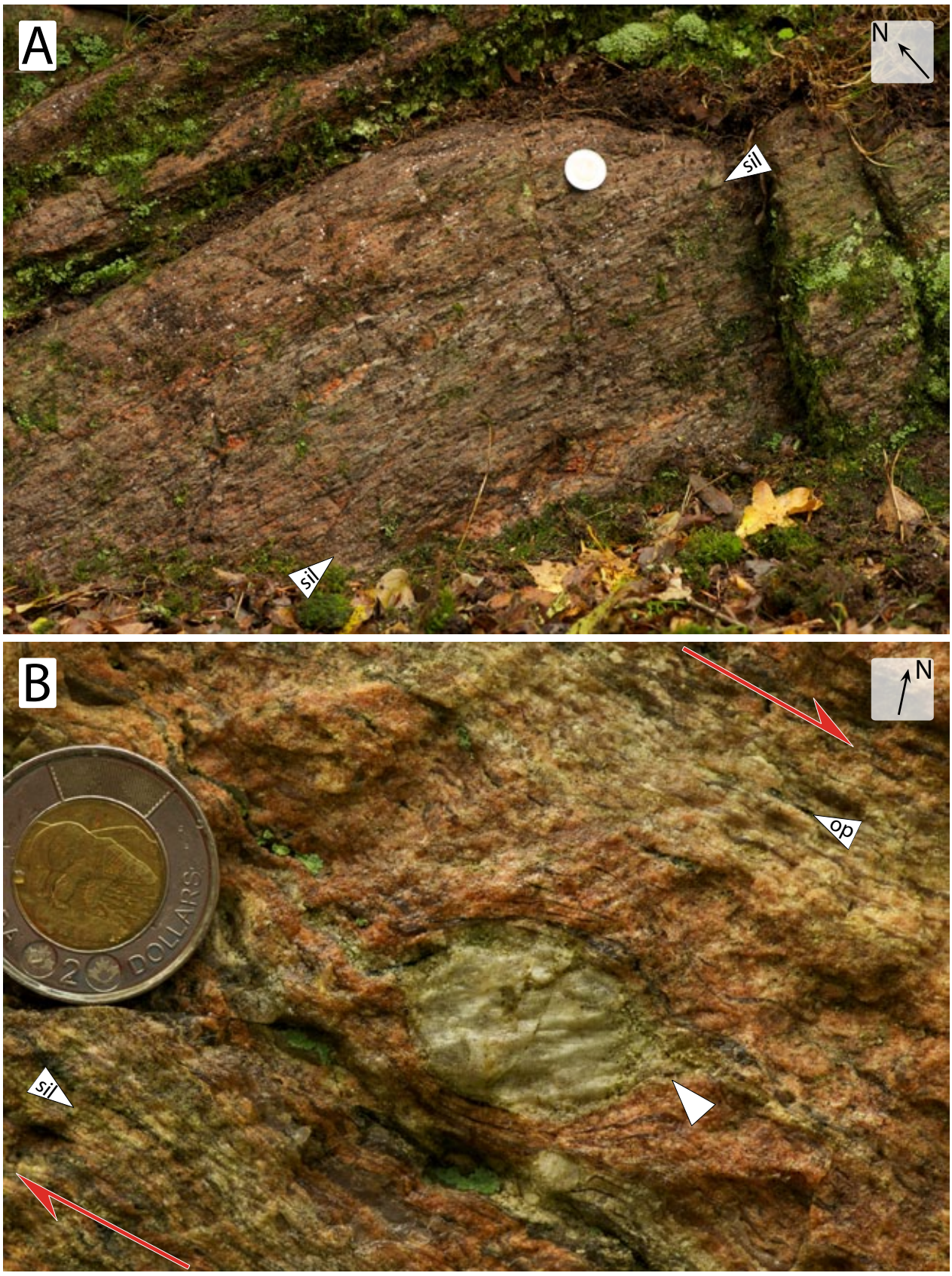

Fig. 29. Migmatized and highly sheared sillimanite-bearing quartz-feldspar gneiss outcrops with coarse ribbon quartz, K-feldspar, and plagioclase. (*A*) S_2 foliations of deformed K-feldspar in a minor F_3 hinge at locality 0050B. Quartz ribbons are clear to smoky grey, and sillimanite is opaque and yellow. (*B*) A large feldspar porphyroclast at locality 0081G is surrounded by finer-grained aggregates - mortar structure, which outlines a δ-structure. Shear directions is top-to-the-east. Coin (28 mm) for scale.

quartz-feldspar gneiss. Coarse K-feldspar contains bleb-by perthitic exsolution, whilst coarse plagioclase with polysynthetic twins frequently contains antiperthite (K-feldspar exsolving out from albitic plagioclase). In general, the perthitic and antiperthitic blebs are irregularly shaped, with no significant variation in lamellae width, and do not show a preferred crystallographic orientation. Garnet is generally anhedral, fine-grained and accumulate into clusters along foliations. Quartz and rutile are common inclusions in garnet, however one elongate garnet orientated parallel to S_2 contained sillimanite and other fine-grained inclusions that were also orientated parallel to the S_2 fabric (Fig. 30D). Relatively large 50-200 μm, rounded, clear, high relief, monazite grains are found sporadically throughout the samples. In cross-polarized light, some monazite grains show concentric banded 2-3rd order interference colors, whilst others show interference colours in discrete microdomains. Monazite grains are found typically along foliations with sillimanite, biotite and garnet, although grains are also scattered amongst the recrystallized quartz and K-feldspar.

The modal distribution for sillimanite is variable; this mineral may represent a minor phase in some samples, and a major phase in others. Depending on the locality, sillimanite may be fine-grained, subrounded prisms (rarely single acicular needles), that collect along foliations. These sillimanite aggregates along with foxy brown biotite, define the smooth, anastomosing foliation (Fig. 30C). In other samples, sillimanite may be a major phase alongside quartz and feldspar, forming larger (>0.5 mm wide), highly fractured, prismatic crystals. Occasionally, the coarse-grained sillimanite forms sigmoids (Fig. 31E).

Sillimanite is often associated with yellowish (ppl) Fe-Al-Si mineral, cordierite, and clear-grey-brown (ppl) biotite (Figs. 30F). The yellowish Fe-Al-Si mineral is interpreted as a late alteration product. Cordierite, when found, is inclusion-rich; most inclusions are very fine-grained sillimanite, biotite, quartz and some other unidentifiable grains in thin section (Figs. 30G). The clear-grey-brown biotite has a wispy, frayed and kinked appearance when contacting the Fe-Al-Si alternation product, Fe-Ti oxides, Fe-sulphides, ± cordierite (Figs. 30F & G).

Clearly distinguishable kyanite with good step-like cleavage is rare (Fig. 30G); it is only found in one thin section. The grain is enveloped by foxy brown biotite, which is located within the same microdomain as cordierite forming a partial rim around garnet. Sillimanite is present as subrounded prisms in the quartzofeldspathic matrix.

Mineral chemistry (sample SM12-0032-1)

Mineral chemistry is compiled into table A4. K-feldspar is K_{90} and sodic-plagioclase is An_{25} (oligoclase). Fine-grained, unzoned garnets have compositions of Alm_{58}, Sps_3, Pyp_{36}, Grs_3, and $x_{Fe} = 68$. One relatively large, elongate garnet porphyroclast contains small, rounded Fe-Al-Si inclusion trails (Fig. 31D). Rounded rutile, apatite and biotite are other inclusions in garnet. Monazite (~100-200 μm) found in the matrix show concentric and sector compositional zonation. Rounded zircons measure ~5-10 μm, whilst slightly prismatic zircons measure between ~30-100 μm. Fe-sulphide cores with Fe-oxide rims containing zinc, and hemo-ilmenite constitute the opaque minerals. Cordierite was not analyzed.

4.3.3.3 Pegmatite dykes

The pegmatite dykes are composed of quartz + K-feldspar ± plagioclase. The primary distinguishing characteristic is that the dykes are always coarser-grained than the (± sillimanite) quartz-feldspar gneiss host, and that the dykes do not contain any mafic minerals. Quartz regularly forms elongate, coarse-grained ribbons around elongated and recrystallized K-feldspar porphyroclasts (Figs. 9A, 10A, & 11).

In thin section, most quartz ribbons are monocrystalline; grains within the ribbon have smoother boundaries and appear less strained than described in the quartz-feldsoar gneiss, suggesting annealing processes such as grain-boundary area reduction (GBAR), whilst others show *some* undulose extinction (Fig. 30H). Coarse, augen-shaped K-feldspar porphyroclasts show undulose extinction. Plagioclase showing polysynthetic twins is restricted to the fine-grained, equant, granoblastic matrix alongside quartz and K-feldspar.

Fig. 30. Photomicrapths and back-scattered electron images (BSE) depicting representative petrology and microtextures for the felsic gneisses and pegmatite dykes. (*A*) Cross-polarized light with inserted gypsum plate (γ = 530 nm) of quartz-feldspar gneiss (SM12-0048B). Coarse quartz has been annealed upon having undergone GBAR, whilst K-feldspar shows undolose extinction and fine-grained recrystallized grain margins. (*B*) Cross-polarized light with inserted gypsum plate (γ = 530 nm) of a mylonitized quartz-feldspar gneiss collected from the Valinge quarry (sample SM12-Q03-1). Dark opaques and biotite outline (white arrows) the microdomain that contains crystal-plastic deformed quartz showing undulose extinction, irregular grain boundaries, and subgrains. (*C*) Plane-polarized light photomicrograph of fine-grained sillimanite prisms in sample SM12-0032-1 aligning parallel with biotite laths; this defines the S_2 foliation. Quartz is recrystallized to elongate shapes with lobate grain boundaries. (*D*) BSE image of sample SM12-0032-1 showing an elongated garnet with aligned inclusion trails orientated parallel to S_2. The inclusions are comprised of an Fe-Al-Si mineral and sillimanite. Monazite is found on the upper right-hand-side of the garnet grain boundary. (*E*) Sigmoid sillimanite porphyroclasts in sample SM12-0054E-2 surrounded by recrystallized K-feldspar, quartz, and some plagioclase. Biotite and Fe-Ti oxides are found sporadically throughout. (*F*) Close-up image of sample SM12-0032-2 showing the Fe-Al-Si mineral in association with the brown-grey-clear wispy primary biotite, sillimanite and an Fe-sulphide mineral. (*G*) Plane-polarized light photomicrograph of a microdomain in SM12-0032-2 containing garnet, biotite, cordierite, kyanite, sillimanite along the cleavage foliation. Kyanite is enveloped with biotite, which is located adjacent to cordierite forming a partial rim around an euhedral garnet blast. (*H*) Cross-polarized light with inserted gypsum plate (γ = 530 nm) of ribbon quartz wrapping around a K-feldspar, augen-shaped porphyroclast in a protomylonitic pegmatite (SM12-0080). Quartz grains in the ribbon have irregular to smooth grain boundaries. Sericite has altered some of the feldspars in the matrix and portions of the augen clast. The matrix is recrystallized to fine-grained granoblastic texture; grains nearest to the quartz ribbon tend to be finer and more elongated (white arrow).

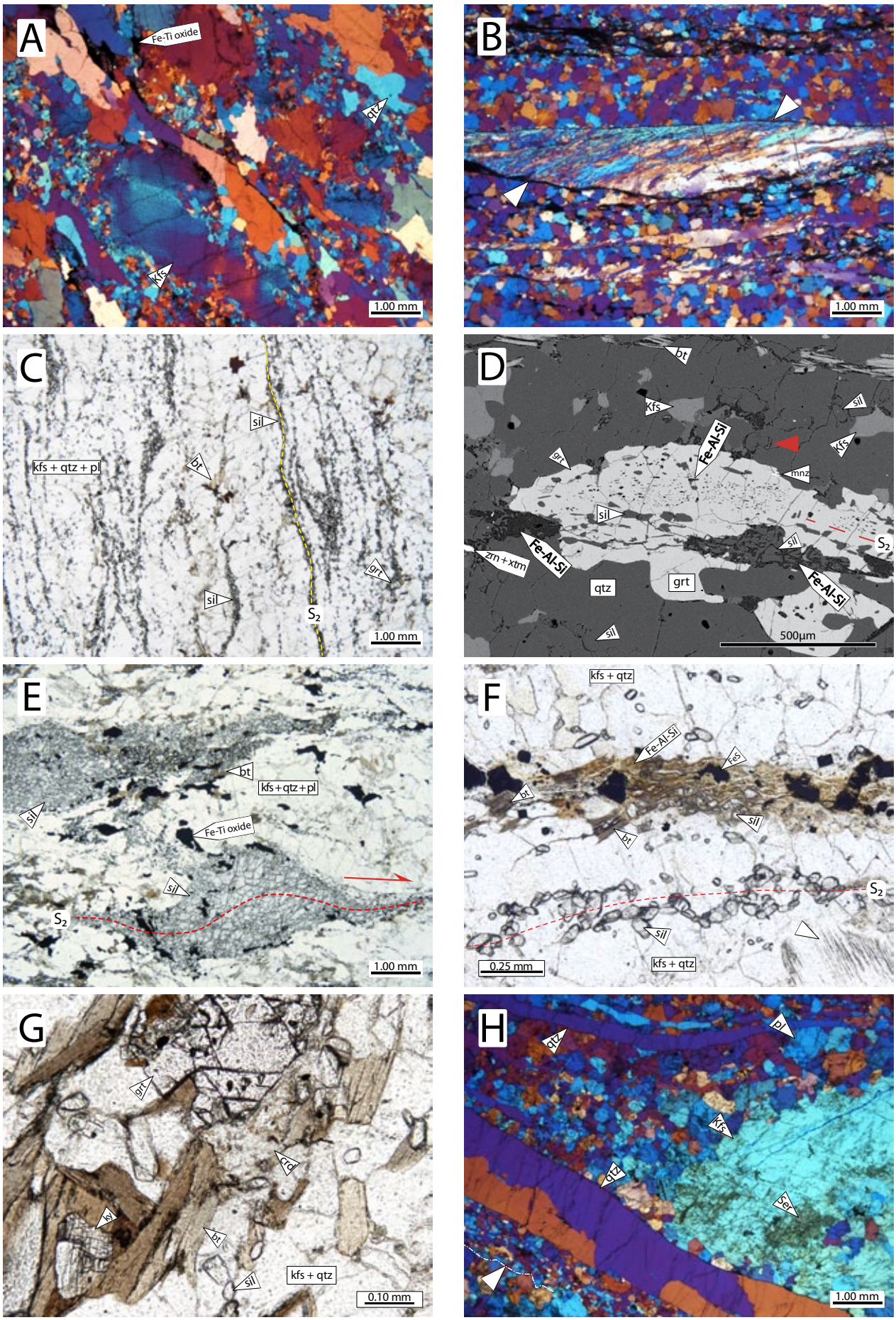
A
Fe-Ti oxide
qtz
Kfs
1.00 mm
B
1.00 mm
C
kfs + qtz + pl
sil
bt
grt
sil
S2
1.00 mm
D
bt
Kfs
sil
Fe-Al-Si
grt
Kfs
mnz
sil
S2
Fe-Al-Si
zrn + xtm
sil
qtz
grt
Fe-Al-Si
sil
500µm
E
bt
kfs + qtz + pl
sil
Fe-Ti oxide
sil
S2
1.00 mm
F
kfs + qtz
Fe-Al-Si
Fe-Si
bt
sil
bt
S2
sil
0.25 mm
kfs + qtz
G
grt
crd
ks
bt
sil
kfs + qtz
0.10 mm
H
qtz
pl
Kfs
qtz
Scp
1.00 mm

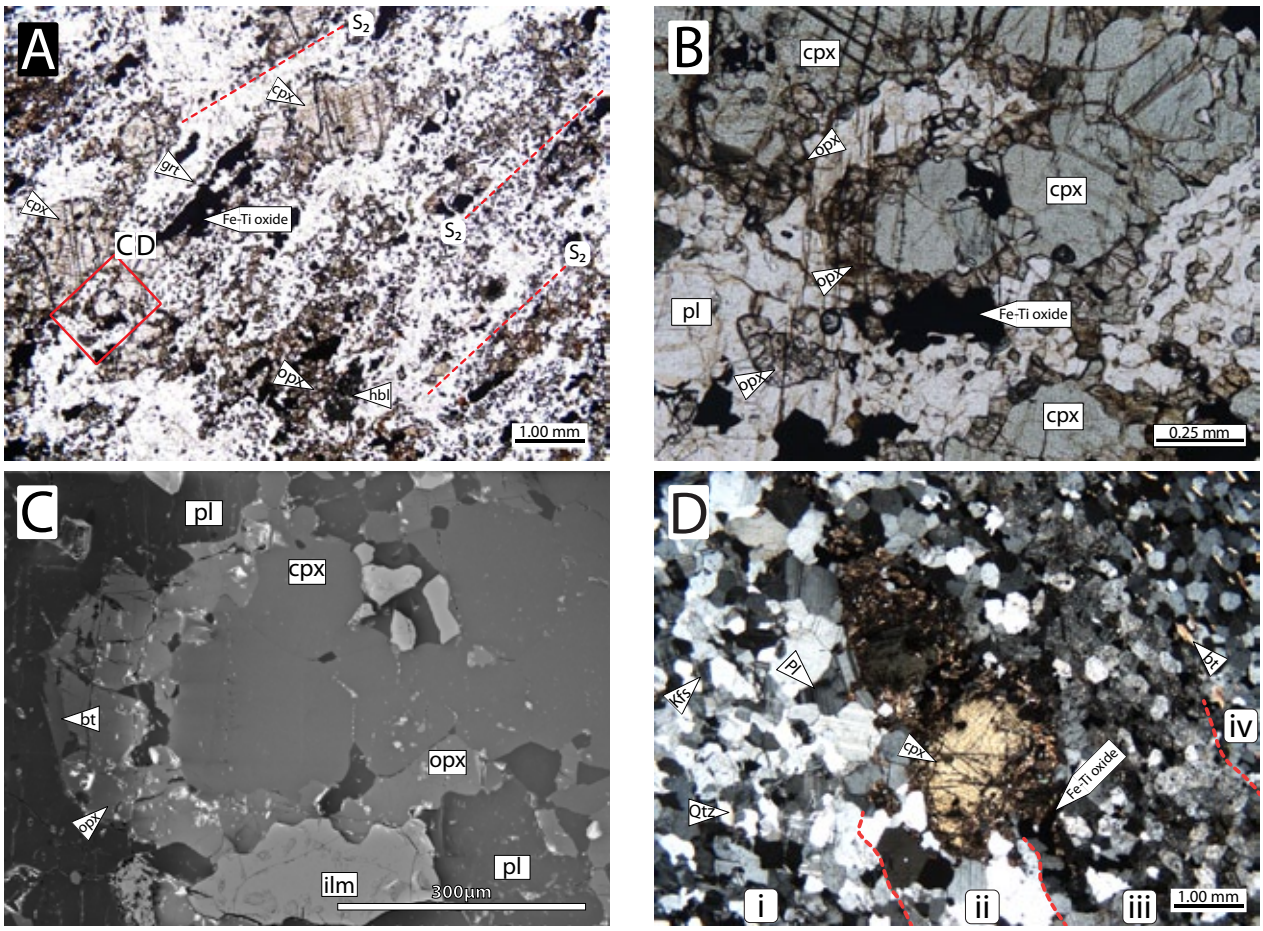

Fig. 31. (*A*) Plane-polarized light photomicrograph of a mafic lens from locality 0046. Large clinopyroxene with elongated Fe-sulphide (not shown) and Fe-Ti oxide minerals trend parallel to S_2 in a mesocratic matrix consisting of granular orthopyroxene and recrystallized plagioclase. Fine-grained garnet and plagioclase mantle the sulphide and oxide minerals. (*B*) Plane-polarized light photomicrograph of a clinopyroxene mantled with orthopyroxene. Fe-Ti oxides are found both internally and externally with respect to the clinopyroxene grain. (*C*) Back-scattered electron image of the identical clinopyroxene in (B). (*D*) Cross-polarized light photomicrograph of a section across the contact surface between the aplite dyke and the host granodiorite gneiss at locality 0062. Zones i-iv indicate textural transitions between the intrusion and the host. (i) Fine-grained aplite consisting of quartz, K-feldspar, & plagioclase. (ii) Coarser grains lie adjacent to the contact. (ii/iii) is the contact surface. Clinopyroxene xenocrysts with altered margins are aligned along the contact surface with the Fe-Ti oxides. (iii) The hydrous fluids accompanied the aplite dyke and altered the host gneiss, such that there is a zone of sericitization adjacent to the intrusion. (iv) The host is a very fine-grained granodiorite gneiss; quartz, K-feldspar and plagioclase are pinned against the foxy brown biotite and opaque minerals.

4.3.4 Localized dykes

Mafic dyke

Brownish-orange charnockitized felsic orthogneiss at localities 0046 & 0047 contain multiple mafic dykes and lenses (Fig. 4E). Charnockitized felsic orthogneisses are also found at locality 0029A. A preliminary observation is that these brownish-orange gneisses appear bounded to the north by an east-west-trending shear zone. The gneiss is composed of medium to coarse-grained K-feldspar, quartz, and plagioclase; forest green hornblende, foxy brown biotite, clinopyroxene with subordinate garnet and severely altered orthopyroxene are found in thin section. The medium to coarse quartz, K-feldspar, and plagioclase have annealed and grown by grain-boundary area reduction (GBAR), however the same minerals are also found in the fine-grained matrix. Much of the K-feldspar contains perthitic exsolution, whilst the plagioclase is antiperthitic.

The mafic dykes tend to be concordant to the foliation in the host gneiss. The dykes are plagioclase-rich; both clino- and orthopyroxene are present, along with forest green hornblende, Fe-Ti oxides and Fe-sulphides; garnet is minor (Fig. 31A). Locally, plagioclase shows strain characterized from curved polysynthetic twins, and undulose extinction with some deeply cuspate margins due to grain boundary migration; blebby anti-perthitic texture is common. The matrix constitutes recrystallized plagioclase, which forms a fine-grained granoblastic texture. Orthopyroxene is very fine-grained and often accumulates into clusters. Orthopyroxene also forms partial rims around larger clinopyroxene (Figs. 31B & C). Clinopyroxene porphyroclasts are comparatively larger (~2 mm) compared to the (~0.1 mm) recrystallized plagioclase matrix. Very fine-grained garnet forms partial rims around Fe-Ti oxide, with thin, 10-50 µm plagioclase moats separating garnet from the Fe-Ti oxide.

Aplite dyke

Light pink, fine-grained, unfoliated aplite dykes crosscut the well-foliated gneissic granodiorite at locality 0062 (see section 4.2.3.2; Fig. 12). Fine-grained K-feldspar and quartz form the centimetre to decimetre thick pink dykes. Small elongate pits along the upper margin of the thickest dyke indicate that relatively larger xenocrysts have weathered away.

In thin section, the aplite dyke is composed of fine-grained, anhedral-subhedral, relatively unstrained K-feldspar and quartz with subordinate plagioclase (Fig. 31D). Elongate clinopyroxene xenocrysts with partially replaced margins align parallel to the strike of the intrusion. The host gneissic granodiorite is finer-grained and has an equant granoblastic texture compared to the dyke. Reduced grain-size is due to fine-grained, recrystallized quartz, plagioclase, K-feldspar, and opaque minerals pinned against biotite. Biotite is foxy brown and aligns with the strike of the gneissic foliation.

5 Interpretations

5.1 Structure

5.1.1 Fold phases, high-strain zones, and the role of competency contrasts

The interference of two fold phases, F_2 and F_3, characterizes the structures of the Säm area. Both phases are fitted to a π-girdle along a great-circle in the stereonets (Fig. 5). However only the youngest fold phase, the F_3 folds are geometrically congruent to a cylindrical fold throughout the *entire* study area. Both the axial surface and the fold axis vary in attitude throughout the *entire* study area for the F_2 folds, which reflects a nonconical noncylindrical fold. The concentration of poles from planes in a particular domain in the stereonets should be regarded as a sampling bias along one particular fold limb due to outcrop availability rather than an indication of fold symmetry (Marshak and Mitra 1988).

Locally, the S_2 axial planes of the upright to recumbent isoclinal F_2 folds are aligned roughly parallel with the F_3 axial plane (S_3). The small tightly folded F_2 axial planes for the area (stereonet E; Fig. 5) show an S_2 axial plane resembling the S_3. This suggests D_3 reworked and transposed the F_2 folds to their present NNE trend; hence the S_2 trends subparallel with the S_3. Coeval with transposition, additional flattening and/or a coaxial deformational pure shear component applied during D_3 to the earlier developed F_2 folds, tightened and narrowed the F_2 hinge zones (stereonets C & D). This deformation event yielded F_3 folds superimposed onto F_2 folds thus creating Type 0 interference patterned similar folds with true-axial planar cleavages along the limbs of the F_3 folds (e.g. Figs. 8A, 14A & 22).

Younger folds are often interpreted from the folded cleavage of an older fold phase generation (e.g. Viola & Mancktelow 2005). In the Säm area, refolded S_2 from F_2 folds during D_3, formed Type 3 interference pattern, NE-plunging, open Class 1C F_3 folds (e.g. locality 0050C; Fig. 19). Locality 0050C is the best example that distinctly displays all three deformation phases in one outcrop. Some of the F_2 folds are in a recumbent position, whilst others are inclined to upright. Many of the recumbent F_2 folds show multiple folds stacked one on top of another (Figs. 17 & 19). The various orientations of the small, isoclinal F_2 folds and the curvilinear S_2 that defines the open similar-shaped F_3 fold, may suggest that F_3 is a sheath fold. However, it should be clearly stated, that this study has not discovered any definitive sheath folds (*y-z* sections may reveal eye-folds; e.g. Searle & Alsop 2007; Alsop & Holdsworth 2012). Detailed small-scale folds are best observed in rocks with a fine-scale compositional layering; much of the Säm area lacks these types of rocks. The absence of data does not necessarily discredit a sheath fold hypothesis.

Garnet amphibolite exhibits some small, tight to isoclinal D_2 folds outlined by the trondhjemitic-tonalitic leucosomes (Fig. 22B). The grains in the outer arc of the fold hinge form a smooth margin, however the inner arc is formed with angular grains. It is interpreted the coarse-grained leucosomes were deformed in the solid state synchronously with F_2 folding to form the thick hinge zones and thin limbs and to orientate the plagioclase's crystallographic cleavage to align subparallel with the F_2 axial plane (S_2). D_3 refolded the F_2 in the ductile to solid state to form the F_3 fold; hence the occurrence of both the recrystallized and strained coarse-grained quartz and plagioclase.

The interpretive cross-sections (Figs. 7A & B) are displayed in a three dimensional block diagram with the intent to emphasize that the structure style, based on field observations and stereonet plots in the Säm area, is characterized partially by active but mostly by passive folding. Active buckle folding is restrained to the F_3 hinge zones (e.g. Fig. 9A & 19), whilst passive folding is associated with shearing in the F_3 limbs to form the isoclinal F_2 folds (e.g. Figs. 10B & 16). Mineral assemblages suggest conservative peak *P-T* conditions were ≥ 8 kbar and ≥ 700 °C (see section 5.2). Therefore highly competent mafic tectonic lenses were ductile enough at peak metamorphism to contort into various fold orientations and geometries in response to a dynamic stress field. Shear zones are concentrated in the sillimanite-bearing quartz-feldspar gneisses, quartz-feldspar gneisses, and pegmatite dykes, which are located adjacent to the mafic tectonic lenses. It is apparent that these less competent felsic rocks accommodated much deformation in the Säm area.

To summarize, the F_2 folds are NNE-SSW trending upright to recumbent isoclinal folds with sharp, angular, and often isolated hinges and thin, stretched, and boudinage limbs (Figs. 8A, 14A, 15, 16, & 17). Near the NE quadrant of the study area, the F_2 axial trace begins to curve; striking from NNE-SSW to NNW-SSE to form the map-scale Type 3 interference pattern. It is interpreted the D_3 event refolded the F_2 folds into broad, open, Class 1C F_3 folds (Figs. 17 & 19). This D_3 event formed a Type 0 interference pattern with the F_2 folds in the F_3 limbs,

and a Type 3 interference pattern with the F_2 folds in the F_3 hinge.

5.1.2 Origin of linear structures

Anatexis and deformation were prevalent in the Säm area. Recrystallization strongly affects linear fabric development during metamorphic events. When the original large grains are heterogeneously deformed and recrystallized to a finer grained matrix, aggregate lineations may develop (Piazolo & Passchier 2002). Concerning mineral grain lineations, the crystallographic growth habit of a mineral in a mono- or polymineralic rock determines if strong lineations form (Vernon 1987). Late recrystallisation and grain growth can diminish the appearance of structures formed earlier during dynamic recrystallisation. This late recrystallisation often succeeds high-temperature deformation, which is favourable for producing grains (Evans et al. 2001). Therefore, macroscopic sillimanite lineations are apparent at certain localities with high-flow stress, and absent at localities dominated by late recrystallisation. Alternatively, sillimanite grain-size variability is exceedingly dependent on a heterogeneously distributed Al_2O_3 wt. %, on nucleation rate in relation to growth rate, and on cation diffusion rates.

Cuspate-lobate folds are restricted to the F_3 hinge zones (fold axis: 08/060; red triangles in stereonet γ) in the very coarse quartz-feldspar gneiss. They are a type of trace lineations (after Piazolo & Passchier 2002; Passchier & Trouw 2005), because the cusps and lobes are essentially buckle folds that formed due to compressional strain during D_3. The trough of the cusp and the crest of the lobe in 3-dimensions create an intersection between an axial planar surface and a planar foliation. Two intersecting planes create a trace lineation. These particular trace lineations are parallel to the S_3, therefore it is interpreted they are related to F_3 folding.

Relationships between folds and lineations can be inferred based on orientations. The two sets of lineations, L_2 and L_3 are aligned approximately orthogonal to each other. L_2 is orientated 37/318 and 26/160 (stereonet β) whilst L_3 is orientated 19/052 (stereonet α), and 08/060 & 29/039 (stereonet γ). The NNW-SSE trending L_2 aligns parallel with the F_2 folded axis (stereonet C). The NE trending L_3 aligns parallel with the F_3 fold axis (stereonets A, B, and F). Lineations are commonly interpreted as the direction of mass transportation (Ellis & Watkinson 1987; Alsop 1992; Wahlgren et al. 1994; Piazolo & Passchier 2002). Fold axes generally align parallel with stretched mineral lineations and shear direction in ductilely deformed rocks (Bell 1978; Alsop 1992; Carreras et al. 2005). It is believed that the L_2 lineations were originally broadly orientated along a NNW-SSE trend after the D_2 event. Subsequently, ~NNW-SSE compression, with a shear component, during D_3 formed the F_3 buckle folds with the NE-trending L_3. The combination of these events resulted in the present-day nonconical noncylindrical F_2 folds with a curviplanar S_2 within the Type 3 interference F_3 fold.

5.1.3 Fold-related fabrics & metamorphic grade

Winged porphyroclasts, tension gashes, and S-C and S-C' type fabrics are examples of shear-sense indicators found in the study area. The majority of these structures suggests a top-to-the-east shear direction. Sigmoidal en-échelon extension vein arrays are robust structures for interpreting shear kinematics (Lisle 2013). A set of extension gashes was found in the metatexite at locality 0033B (Fig. 20B), the direction of their vein tips (S-shaped) suggested translation of the upper vein tip was sinistral — top-to-the-WNW shear. Flanking folds in the garnet amphibolite also suggest top-to-the-WNW shear-sense (Fig. 24). This implies that the garnet amphibolite lens at this locality and along this general strike, was overturned possibly syn-kinematically with D_3 shearing.

Net structures in this study are the result of progressive subsimple shear during steady-state flow (rotating x-axis of the strain ellipsoid), which stretched out the competent mafic tectonic lenses. These structures are formed from synthetic and antithetic extensional shear bands connected with stromatic (foliation-parallel) leucosomes. At early stages of development, leucocratic stringers (boudin necks) are positioned orthogonal or at oblique angles to the S_2 (strong anisotropic plane). As deformation proceeds, the oblique leucocratic stringers decrease their angle with the S_2 towards zero (Fig. 32). When time is set as an independent variable, progressive subsimple shear will rotate the x-axis of the strain ellipsoid such that it aligns with the S_2, expressed mathematically with the kinematic vorticity number (Wk; Fossen & Tikoff 1998). Hence the stromatic leucosomes align parallel to the S_2 and act as transport channels in liaison with the oblique leucocratic stringers, to shunt melt from the rock. The oblique leucosomes are relatively thick, suggesting melt movement is guided by a pressure gradient towards the dilatant sites. Melt is then transferred (drained) out of the system along channel-like stromatic leucosomes (Sawyer 2001; Guenina & Sawyer 2003). The thinnest leucosomes are not as well interconnected and may reflect older channels. With increasing melt fraction, strain is favorably redistributed into the softer dilatant boudin necks and stromatic leucosomes from the competent melanosome (Vigneresse & Tikoff 1999). Eventually, when a high melt fraction has been extracted out, the boudin becomes a competent, dehydrated, residuum.

5.2 Petrology

5.2.1 Amphibolites

Overview

Smooth grain contacts forming triple junctions is found throughout the garnet-poor and garnet amphibolites. This suggests the present mineral assemblages (M_3) are generally in textural equilibrium with the most recent deformation event (D_3). Prograde assemblages are not preserved. Some disequilibrium microtextures have developed in microdomains. The following sections will address some of the observations.

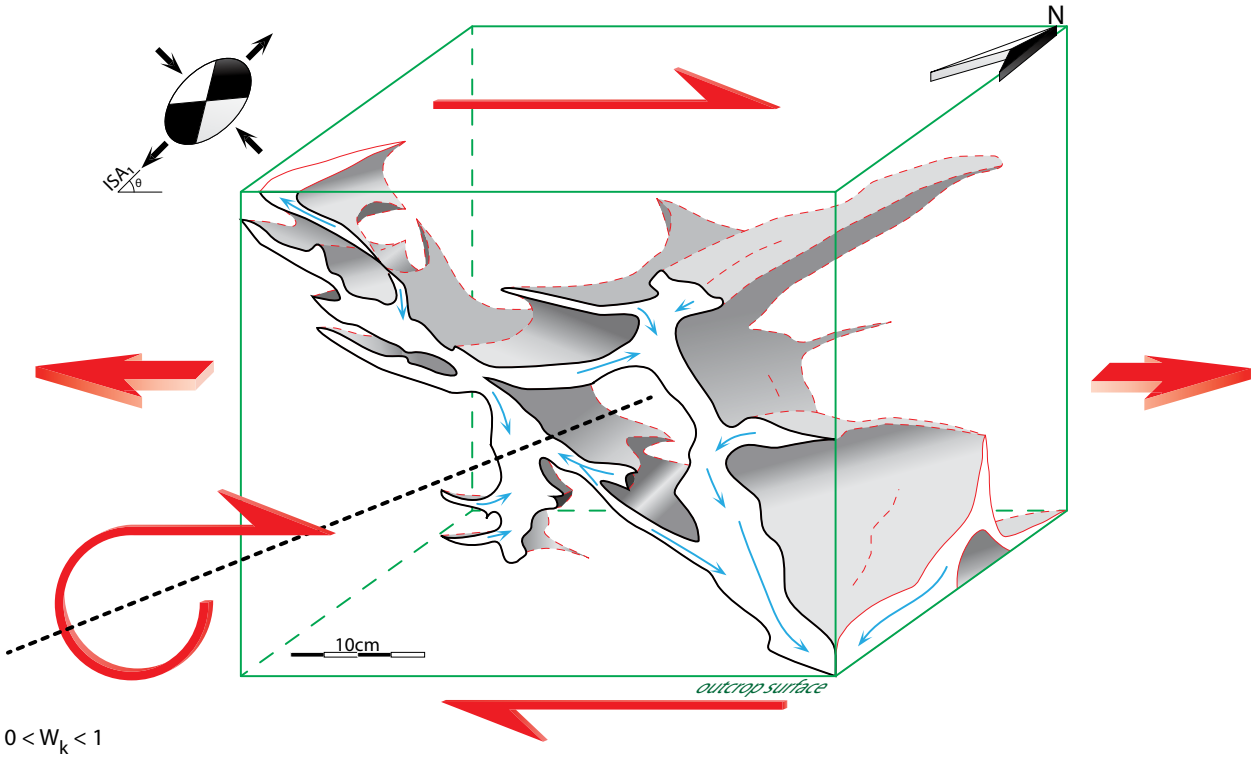

Fig. 32. Illustrative block diagram of the net migmatite observed at locality 0103 (Fig. 25). Veins are interconnected channels in 3-dimensions, segregating and transporting the anatactic melt (blue arrows) along pressure gradients out of the system. Pressure gradients are dependent of non-coaxial deformation (coeval pure shear + simple shear components). The kinematic vorticity vector (W_k) is $W_k = 0$ for pure shear; $W_k = 1$ for simple shear.

Mineral assemblage - garnet-poor amphibolite

Hornblende, plagioclase, quartz, clinopyroxene, Fe-Ti oxides, and biotite, with rare garnets, compose a typical mineral assemblage for the upper amphibolite to granulite facies in metamorphosed mafic rocks. Depending on the bulk rock chemistry, these minerals are in equilibrium over a wide range; ~700-850 °C and ~9-14 kbar (based on a pseudosection for a different study from De Paoli et al. 2012). Garnet is subordinate and therefore it is likely that the stable mineral assemblage excludes garnet, thus the field extends down to ~600 °C and ~4 kbar. Plagioclase, hornblende, quartz, clinopyroxene, and biotite all share common contacts and form triple junctions. Garnet and Fe-Ti oxide appear in disequilibrium and are further discussed. Prograde assemblages are not preserved.

Mineral assemblage - garnet amphibolite

Hornblende, garnet, plagioclase, quartz, clinopyroxene, Fe-Ti oxide, and biotite is again, a typical mineral assemblage for the upper amphibolite to granulite facies. Here the modal proportion of garnet is much higher, thus the stability field is limited to ~700-850 °C and ~9-14 kbar (after De Paoli et al. 2012). Orthopyroxene is found forming coronas around clinopyroxene and Fe-Ti oxide. This implies the rock traveled through the orthopyroxene-bearing stability field during decompression, but did not reach equilibrium. At ~825 °C and 10 kbar, orthopyroxene is stable in a trivarient field (after De Paoli et al. 2012).

Garnet fringes around Fe-Ti oxides

A low modal proportion of garnet characterizes the garnet-poor amphibolite and mafic dykes in which, locally, garnets form fringes around Fe-Ti oxide with a moat of plagioclase separating garnet from the Fe-Ti oxide; orthopyroxene is absent (Figs. 26C & 31A). Similar garnet fringes around Fe-Ti oxides characterize the migmatized metagabbros in the Lewisian Complex, NW Scotland (Savage & Sills 1980; Johnston & White 2011). This microtexture is presumably a late stage retrograde reaction during isobaric cooling (Savage & Sills 1980), although the strong localization of these garnet fringes, which occur solely around Fe-Ti oxides containing intergrown lamellae may be the result of prograde or retrograde reactions (Johnston & White 2011; personal communication, Möller 2013).

Zoning patterns in garnet – garnet amphibolite

In general, Ca-enriched garnet cores are partially attributed to the transition of Ca-plagioclase to Na-plagioclase during prograde metamorphism, from amphibolite to granulite (and/or eclogite) facies (Spear 1993; Pattison 2003). Therefore decreasing grossular content from core to rim in zoning profiles is typical for mafic rocks that experienced high-pressure environments (O'Brien 1997, 2003).

Garnet composition profiles for the Säm study are generally flat. Both the Fe- and Mg-content in the garnet

profiles show small decreases from rim-core-rim whilst the Mn-content remains constantly low and flat. The Ca-content profile shows the most curvature, with the maximum located in the garnet core and the minimum in the rim. Flat garnet zoning patterns are attributed to re-equilibrium at high temperatures (Spear, 1993; Hartel & Pattison 1996). Fe^{2+}, Mg^{2+}, and Mn^{2+} volume diffusion is faster than that of Ca^{2+} because of the size of the effective ionic radius (Schwandt et al. 1996; Vielzeuf et al. 2007).

Plagioclase in clinopyroxene blasts & melt textures – both amphibolites

Patch and nebulite migmatites often contain large, coarse, dark, forest-green clinopyroxene blasts in plagioclase-dominated leucosomes (Fig. 14A). Johnston et al. (2012) reported similar peritectic clinopyroxene blasts that grew in response to decompression from high-medium pressures, however they did not provide microtextural details. Hartel & Pattison (1996) also took note of garnet and diopside within both the leucosome and mesosome, and suggested it was indicative of a stable mafic assemblage within leucocratic domains. For the Säm amphibolites, it is believed that the microtexture consisting of plagioclase blebs inside clinopyroxene is the result of dehydrated amphibole reacting with plagioclase and quartz (incongruent melting). Amphibole may: a) dehydrate directly to clinopyroxene and a melt phase, or b) amphibole may release some vapour. The vapour + amphibole and plagioclase will react to produce garnet and clinopyroxene (Wolf & Wyllie 1991; 1994).

Experimental results at constant moderate pressure (10 kbar) with increasing temperature and field studies show that a mafic amphibolite consisting of plagioclase and hornblende will begin to react around ~750-850 °C to form a stepwise-series of products, which may include: melt, clinopyroxene, secondary hornblende, garnet, and orthopyroxene (Wolf & Wyllie 1994; Sawyer et al. 2011). Trondhjemite-tonalite melts are achieved with the incongruent dehydration melting of an amphibolite rock, achieved by the following reaction:

Hbl + Pl ± Qtz = Cpx + Grt + trondhjemite-tonalite melt ± Opx (1)

(Hartel & Pattison 1996). Feldspar compositions from the leucosomes are plotted in Fig. 35. It may be possible to track the evolution of the melt composition with increasing *P-T*.

Correlating experimental results from Wolf & Wyllie (1991) with microtextures observed in the Säm rocks, their figure 9 representing the microtextures at 1000 °C appears texturally similar to this study's clinopyroxenes (e.g. Figs. 26D-E & 27B-E). In both Wolf & Wyllie (1991) and this study, clinopyroxene contains many blebby inclusions of plagioclase, hornblende and some orthopyroxene. Wolf & Wyllie (1991) did not report on Fe-Ti oxides, and therefore are assumed to be absent in the experiment, unlike the Säm amphibolites. The experimental results suggests clinopyroxene grew from the melt at ≥925 °C & 10 kbar. This temperature appears rather high, however modern modeling techniques using internally consistent thermodynamic datasets with THERMOCALC to produce *P-T* and *P-X* pseudosections show that biotite can be stable up to ~940 °C at 12 kbar (Di Paoli et al. 2012). Orthopyroxene inclusions in clinopyroxene and thin orthopyroxene coronas preserved around clinopyroxene and Fe-Ti oxide suggest the garnet amphibolite traveled through *P-T* conditions of ~825 °C and ~10 kbar, possibly during exhumation.

In comparison, the mafic dyke (locality 0046; Figs. 31A-C) shows a peak or near-peak assemblage containing both clinopyroxene and orthopyroxene with plagioclase, hornblende, and ilmenite ± garnet. This similarly suggests a *P-T* estimate of around ~825 °C and ~10 kbar (based on a pseudosection for a different study from De Paoli et al. 2012).

Creating *P-T* and *P-X* pseudosections to constrain the metamorphism for the Säm area would be desirable for future research, however a) there has yet to be established a robust thermodynamic model for mafic rocks, b) the greater volume of melt will provide erroneous results, and c) high cation diffusion rates at granulite facies allows the propensity for minerals to re-equilibriate upon cooling.

High surface-to-volume ratios of quartz and plagioclase forming irregular shapes with low- to high- "apparent" dihedral angles in the pore space between solid grains (intercumulus texture) is interpreted as melt (Figs. 27G-H; after Wolf & Wyllie 1991; Hartel & Pattison 1996; Sawyer 2001; Holness & Sawyer 2008; Johnston et al. 2013). Preserving this melt texture would possibly require a heterogeneous cooling rate, such that initial slow cooling of the rock would promote an equant granoblastic plagioclase and quartz matrix, followed by a transition to an accelerated cooling rate towards the final stages of crystallization. Therefore the last melt before passing the solidus formed an irregular geometry with a high

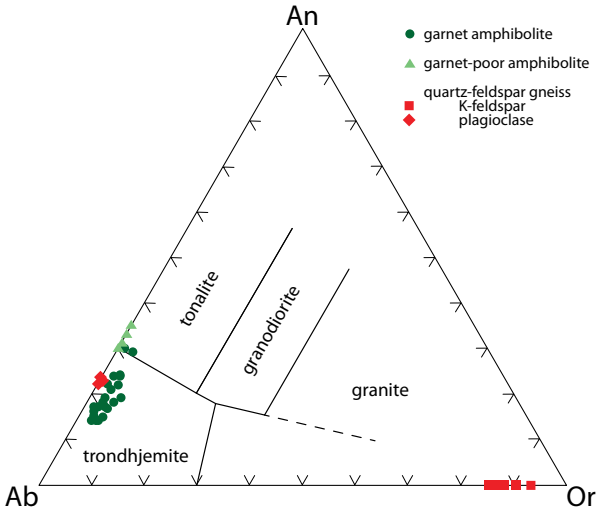

Fig. 33. Normative feldspar classification of leucosomes according to Barker (1979). Compositions are from samples SM12-0019 (garnet-poor amphibolite), SM12-0026B-1 (garnet amphibolite), and SM12-0032-1 (quartz-feldspar gneiss).

surface-to-volume ratio and low- to high- "apparent" dihedral angles. Sub-solidus crystallographic modification is minimal (after Holness et al. 2012). This melt texture is representative of textural inequilibrium and is indicative of an unstable environment inhibiting a) interfacial energy reduction, and b) nucleation and growth in a small pore spaces (Holness & Sawyer 2008; Holness et al. 2012).

5.2.3 Sillimanite-bearing quartz-feldspar gneiss

Sillimanite-bearing quartz-feldspar gneisses exposed at various localities throughout the Eastern Segment, are *very* briefly mentioned in several studies (Hubbard 1975; Johansson et al. 1991; Andersson et al. 1999). These rocks along with sillimanite-absent quartz-feldspar gneisses form a sequence of rocks that are believed to be supracrustal in origin (C. Möller, personal communication 2013). It is unlikely that the occurrence of sillimanite is due to metasomatic processes from fluid infiltration causing base-cation leaching (after Vernon 1987; Wintsch & Andrews 1988), or due to "stress-induced solution transfer" promoting syn-deformation sillimanite-growth along shear zones (after Musumeci 2002). The original peraluminous bulk rock composition favoured sillimanite at high grade metamorphism. It must be noted, the original bulk rock composition has been greatly altered after anatexis, with presumably some unknown volume of melt-loss. These paragneisses, the quartz-feldspar and sillimanite-bearing quartz-feldspar gneisses, were intruded by an extensive network of pegmatite dykes, of which they share a common deformation history. These dykes also presumably altered the original bulk rock chemistry.

The sillimanite-bearing quartz-feldspar gneisses possess a bulk rock composition that is favourable for a variety of polymineral assemblages at different *P-T* conditions, unlike the other two felsic rocks in this study, which are primarily composed of quartz, K-feldspar and plagioclase. The appearance (and absence) of marker minerals such as K-feldspar, sillimanite, cordierite, kyanite, and orthopyroxene for the sillimanite-bearing quartz-feldspar gneiss constrain the stability field to a particular metamorphic grade. Quartz, K-feldspar, plagioclase, biotite, sillimanite, garnet, and Fe-Ti oxide all form common contacts with triple junctions throughout the samples, and is therefore interpreted as the stable mineral assemblage that experienced D_3. These minerals were perhaps stable at *P-T* conditions of ~650-850 °C and ~3-10 kbar, depending on the bulk rock composition (based on pseudosections for different studies from Guilmette et al. 2011; Cubley & Pattison 2012).

The occurrence of kyanite in the sillimanite-bearing quartz-feldspar gneiss (Fig. 30G) suggests either a) the rock achieved equilibrium along the univariant line, or b) the prograde path traversed through the kyanite stability field before entering into the sillimanite field with increasing temperature. The latter hypothesis is more reasonable, for kyanite is relatively rare and thus it likely pseudomorphed into sillimanite along the prograde *P-T-t* path.

Interestingly, Fig. 30G also shows a mineral appearing as cordierite around garnet with sillimanite, biotite, quartz, and K-feldspar. Cordierite is commonly formed from high-temperature anatectic melts at medium to low pressures, and is the reaction product between sillimanite, dehydrated biotite and a melt (Spear 1993):

$$\text{Sil} + \text{Bt} = \text{Grt} + \text{Crd} + \text{Kfs} + \text{L} \qquad (2)$$

Sillimanite inclusions in cordierite partially enveloping garnet suggests decompression reactions ≤5 kbar from higher pressure (as indicated by the kyanite). The coexistence of K-feldspar in the microdomain restricts reaction (2) to high temperatures (Spear 1993).

6 Tectonic implications

6.1 Correlating deformation phases with metamorphic conditions

Petrological analyses show the Säm ortho- and paragneisses contain high-pressure mineral assemblages, followed by high-temperature assemblages, and finally retrograde amphibolite facies overprinting, reflecting exhumation along a clockwise *P-T-t* metamorphic path. Acknowledging that the youngest structures are best preserved in high-grade gneiss terranes, it is most efficient to form correlations between deformation phases and metamorphic conditions in reverse order.

The net migmatites observed in the garnet amphibolite are related to deformation and metamorphic conditions. Melt channels crosscut the S_1 // S_2 foliation, whilst thinner net migmatites align subparallel with the foliations. The segregated anatectic melt which was draining out from the mafic tectonic lens through the migmatite network channels, guided by a pressure gradient established during D_2 and/or D_3 folding, formed at granulite facies conditions. Anatexis is confirmed in thin section from the intercumulus melt texture within the mesocratic domains, which is defined by quartz and plagioclase crystals with a high surface-to-volume ratio hence forming irregular shapes in the pore space between solid grains.

Both the pegmatite dykes and the paragneisses show folds created during D_3 and D_2. However, it is somewhat more difficult to establish if the dykes also share the D_1, or if the pegmatite intruded along S_1 foliations post-D_1. The broad, NE-SW trending, Class 1C F_3 buckle folds were formed from a NNW-SSE compressional force with a NE-SW shear component that tightened and stretched the isoclinal F_2 folds. The sillimanite-bearing quartz-feldspar mineral assemblage shows that high-pressure was achieved in the Säm area, interpreted the occurrence of a mineral appearing as kyanite during D_2. This was followed by high-temperature *P-T* conditions and then decompression during D_3. The fact that the mineral assemblage is textually stable along S_2 foliations that were subsequently refolded during D_3 throughout Säm suggests D_2 and D_3 were created during one metamorphic event.

6.2 Differences and similarities to other parts of the Eastern Segment

Throughout the southern parts of the Eastern Segment, regional kinematic shear-sense including the majority of the Säm area is top-to-the-east or top-to-the-NE (Möller & Söderlund 1997; Möller et al. 1997; Möller et al. 2007). Folds around Säm are also of similar character to those found in the Eastern Segment; large-scale F_3 folds are generally upright to overturned, have a wavelength in the order of kilometers, and have undulating fold axes, whilst asymmetrical, tight, isoclinal F_2 folds often have isolated hinges and boudinage limbs (Möller et al. 2007; Tual et al. 2013). Penetrative D_3 and D_2 overprinting *usually* results in D_1 being interpreted as simply a deformation phase forming a gneissic S_1 foliation (Larson et al. 1986) — similarly interpreted in the current study.

Approximately 40 km to the east of Säm, near the town of Ätran, is the fold closure of an isoclinal, non-cylindrical, east-plunging fold nappe that extruded eclogitized crust towards the Fennoscandian foreland (Möller et al. 2013). Structures described herein for the Säm area, hold similar characteristics. The deformation history of these two study areas may therefore share commonalities. Situated between Säm and Ätran, lies the ~10 km wide Ullared Deformation Zone (UDZ), which is syn-kinematic to the emplacement of this eclogite-bearing fold nappe (D_3). The UDZ accommodated a significant amount of strain during extrusion, however strain may have also affected rocks further west.

The NNW-SSE compression and the SW-NE shearing experienced in the Säm area forming the regionally characteristic deformation style at peak orogenesis, was directly related to: (1) the emplacement of the eclogite nappe, which flattened (Type 0 interference pattern), sheared, and transposed the similar-shape, isoclinal F_2 folds to their present NNE trend, and (2) the close proximity of Säm area to the Mylonite Zone, which acted as a rigid boundary during extrusion, such that rocks between Ätran and the Mylonite zone were compressed on a N-S trend. The limited space buckled and refolded the F_2 folds to form Type 3 interference, NE-plunging, open, Class 1C F_3 folds (Fig. 34). Therefore, the D_3 event experienced around Ätran during extrusion of the eclogite, was similarly experienced to the west, around Säm.

7 Conclusions

Detailed structural, petrological, and microstructural analyses on the Säm polyphase fold of the high-grade orthogneiss and paragneiss sequence in the Eastern Segment of the Sveconorwegian orogen have produced the following results:

(1) A collection of garnet amphibolite lenses outlines an ~5 km^2 polydeformed structure. F_2 folds are NNE-SSW trending, upright to recumbent isoclinal folds with sharp, angular, and often isolated hinges and thinned, stretched, and boudinage limbs. Near the NE quadrant of the study area, the F_2 axial trace begins to curve; striking from NNE-SSW to NNW-SSE trends, thereby forming the map-scale Type 3 interference pattern. It is interpreted the D_3 event refolded the F_2 folds into broad, open, Class 1C F_3 folds. This D_3 event formed a Type 0 interference pattern with the F_2 folds in the F_3 limbs, and a Type 3 interference pattern with the F_2 folds in the F_3 hinge.

(2) Upper amphibolite to granulite facies was achieved in the garnet amphibolite. The earliest assemblages preserved found plagioclase inclusions in clinopyroxene and orthopyroxene had formed coronas around clinopyroxene and Fe-Ti oxides, indicative of high temperatures ~800-850 °C at ~10 kbar. The texturally equilibrated mineral assemblage consists of garnet + clinopyroxene + plagioclase + quartz + hornblende + Fe-Ti oxides, and is found stable at *P-T* conditions of ~700-800 °C and ~9-14 kbar.

(3) The sillimanite-bearing quartz-feldspar gneiss showed a clockwise *P-T-t* evolution. A single grain of kyanite is believed to have been found, suggesting the paragneiss had travelled through the relatively higher pressure, kyanite stability field; possibly during D_2. A stable mineral assemblage containing quartz, K-feldspar, plagioclase, biotite, sillimanite, garnet, and Fe-Ti oxide suggest *P-T* conditions of ~650-850 °C and ~3-10 kbar. Cordierite was found reacting with garnet in the presence of K-feldspar, which suggested D_3 decompression of ≤5 kbar occurred at high temperatures (≥650 °C).

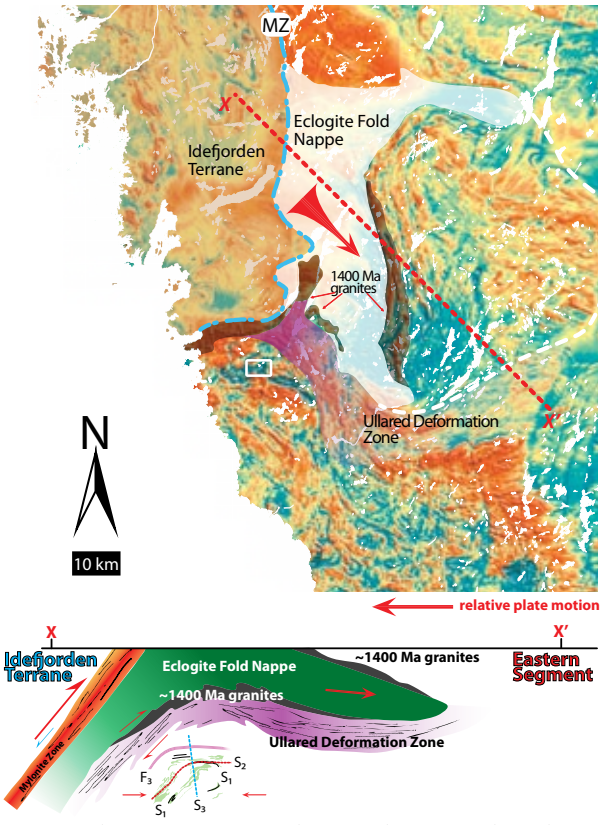

Fig. 34. Airborne magnetic anomaly map with corresponding schematic tectonic extrusion model for the eclogite fold nappe, and its relationship with folding found in the footwall (e.g. this study; Modified after Möller et al. 2013).

8 Acknowledgements

First and foremost, I would like to express my sincere gratitude to Charlotte Möller. Her time, patience, and fruitful discussions have been much appreciated over these past months. Jenny Andersson is also thanked for her comments, but also for her description of the rocks around Obbhult — I will not repeat! As well, if it were not for sharing a chairlift on that bitter cold, snowy day in Whitefish, Montana 2010 with Brendan Dyck, this adventure would never have blossomed. This MSc project is an integral part of the research project funded by a grant # 60-1655/2009 from the Geological Survey of Sweden to C. Möller.

The TRANSCAND excursion led by David Gee, was truly an inspirational experience; David, Bjarne and Matthew to name a few, told me some fantastic stories of where geology had taken them. Friends and peers from all around the world; Calgary, Australia, Brazil, Netherlands, Germany, and of course Sweden, are thanked. Life is better with company! The culmination of these post-secondary studies is partly due to my stubbornness of never settling for less; to set higher standards, and then to surpass them. This stubbornness was instilled into my soul partly from a high school Precalculus Mathematics teacher. Each week he would say "M. Stephen, qu'est-ce que vous avez reçu sur ta quizze de la semaine passée? Faites tes devoirs!" My parents and brother are also partly to thank for this stubbornness; even if I came home with a good grade, "best in the class", there was always room to improve. As well, I never thank them enough for moving to Calgary after I completed high school in Winnipeg. We always loved the mountains, however I never imagined studying rocks. Finally, possibly most importantly, the one person that says very little but means probably the most, is my dog, the Whisk.

9 References

Alsop, G.I., 1992: Progressive deformation and the rotation of contemporary fold axes in the Ballybofey Nappe, north-west Ireland. *Geological Journal 27*, 71-283.

Alsop, G.I., & Holdsworth, R.E., 2012: The three dimensional shape and localisation of deformation within multilayer sheath folds. *Journal of Structural Geology 44*, 110-128. doi: 10.1016/j.jsg.2012.08.015

Andersson, J., Söderlund, U., Cornell, D., Johansson, L. & Möller, C., 1999: Sveconorwegian (Grenvillian) deformation, metamorphism and leucosome formation in SW Sweden, SW Baltic Shield: constraints from a Mesoproterozoic granite intrusion. *Precambrian Research 98*, 151-171.

Andersson J, Möller C., & Johansson, L., 2002: Zircon geochronology of migmatite gneisses along the Mylonite Zone (S Sweden): a major Sveconorwegian terrane boundary in the Baltic Shield. *Precambrian Research 114*, 121-147. doi: 10.1016/S0301-9268(01)00220-0

Arslan, A., Passchier, C.W. & Kohn, D., 2008: Foliation boudinaged. *Journal of Structural Geology 30*, 291-309. doi: 10.1016/j.jsg.2007.11.004

Barker, F., 1979: Trondhjemite: Definition, environment and hypotheses of origin. *In* Barker, F. (ed.): *Trondhjemites Dacites and Related Rocks*. Elsevier, Amsterdam. pp 1-12.

Bell, T.H., 1978: Progressive deformation and reorientation of fold axes in a ductile mylonite zone: the Woodroffe thrust. *Tectonophysics 44*, 285-320.

Bingen, B., Nordgulen, Ø. & Giulio, V., 2008: A four-phase model for the Sveconorwegian orogeny, SW Scandinavia. *Norwegian Journal of Geology 88*, 43-72.

Bingen, B., Skår, Ø., Marker, M., Sigmond, E.M.O., Nordgulen, Ø., Ragnhildstveit, J., Mansfield, J., Tucker, R.D. & Liégois, J.-P., 2005: Timing of continental building in the Sveconorwegian orogen, SW Scandinavia. *Norwegian Journal of Geology 85*, 87-116.

Bogdanova, S.V., Bingen, B., Gorbatschev, R., Kheraskova, T.N., Kozlov, V.I., Puchkov, V.N. & Volozh, Y.A., 2008: The East European Craton (Baltica) before and during the assembly of Rodinia, *Precambrian Research 160*, 23-45. doi: 10.1016/j.precamres.2007.04.024

Brander, L. & Söderlund, U., 2009: Mesoproterozoic (1.47–1.44 Ga) orogenic magmatism in Fennoscandia; Baddeleyite U–Pb dating of a suite of massif-type anorthosite in S. Sweden. *International Journal of Earth Sciences 98*, 499-516. doi: 10.1007/s00531-007-0281-0

Cardozo, N. & Allmendinger, R.W., 2013: Spherical projections with OSXStereonet. *Computers and Geosciences 51*, 193-205. doi: 10.1016/j.cageo.2012.07.021

Carreras, J., Druguet, E. & Griera, A., 2005: Shear zone-related folds. *Journal of Structural Geology 27*, 1229-1251. doi:10.1016/j.jsg.2004.08.004

Cubley J.F. & Pattison, D.R.M., 2012: Metamorphism and deformation of the Grand Forks complex: implications for the exhumation history of the Shuswap core complex, southern British Columbia. *Canadian Journal of Earth Sciences 49*, 1329-1363. doi:10.1139/e2012-066

Dalziel, I.W.D., 1997: Neoproterozoic-Paleozoic geography and tectonics: Review, hypothesis, environmental speculation. *GSA Bulletin 109*, 16-42.

De Paoli, M.C., Clarke, G.L. & Daczko, N.R., 2012: Mineral equilibria modeling of the granulite-eclogite transition: Effects of whole-rock composition on metamorphic facies type-assemblages. *Journal of Petrology 53*, 949-970. doi:10.1093/petrology/egs004

Ellis, M. & Watkinson, A.J., 1987: Orogen-parallel extension and oblique tectonics: The relation between stretching lineations and relative plate motions, *Geology 15*, 1022-1026.

Evans, B., Renner, J. & Hirth, G., 2001: A few remarks on the kinetics of static grain growth in rocks. *International Journal of Earth Sciences 90*, 88-103.

Fossen, H. & Tikoff, B., 1998: Extended models of transpression and transtension, and application to tectonic settings. *In*: Holdsworth, R.E., Strachan, R.A. & Dewey, J.E. (eds.): *Continental, Transpressional, and Transtensional Tectonics*. Geological Society, London, Special Publications, 135, 15-33.

Gorbatschev, R. & Bogdanova, S., 1993: Frontiers in the Baltic Shield. *Precambrian Research 64*, 3-21.

Goscombe, B.D., Passchier, C.W. & Hand, M., 2004: Boudinage classification: end-member boudin types and modified structures. *Journal of Structural Geology 26*, 739-763. doi: 10.1016/j.jsg.2003.08.015

Guernina, S. & Sawyer, E.W., 2003: Large-scale melt-depletion in granulite terranes: an example from the Archean Ashuanipi Subprovince of Quebec. *Journal of Metamorphic Geology 21*, 181-201. doi: 10.1046/j.1525-1314.2003.00436.x

Guilmette, C., Indares, A. & Hébert, R., 2011: High-pressure anatectic paragneisses from the Namche Barwa, Eastern Himalayan Syntaxis: Textural evidence for partial melting, phase equilibria modeling and tectonic implications. *Lithos 124*, 66-81. doi:10.1016/j.lithos.2010.09.003

Harlov, D.E., Kerkhof, A.V.D. & Johansson L., 2013: The Varberg-Torpa Charnockite-Granite Association, SW Sweden: Mineralogy, petrology and fluid inclusion chemistry. *Journal of Petrology 54*, 3-40. doi: 10.1093/petrology/egs060

Hartel, T.H.D. & Pattison, D.R.M., 1996: Genesis of the Kapuskasing (Ontario) migmatitic mafic granulites by dehydration melting of amphibolite: the importance of quartz to reaction progress. *Journal of Metamorphic Geology 14*, 591-611.

Hawthorne, F.C., Oberti, R., Harlow, G.E. Maresch, W.V., Martin, R.F., Schumacher, J.C. & Welch, M.D., 2012: Nomenclature of the amphibole supergroup. *American Mineralogist 97*, 2031-2048. doi: 10.2138/am.2012.4276

Hoffman, P. F., 1988: United Plates of America, The birth of a craton: Early Proterozoic assembly and growth of Laurentia. *Annual review of Earth and Planetary Sciences 16*, 543-603.

Holness, M.B., Humphreys M.C.S, Sides, R., Helz, R.T. & Tegner, C., 2012: Toward an understanding of disequilibrium dihedral angles in mafic rocks. *Journal of Geophysical Research 117*, B06207. doi:

10.1029/2011JB008902

Holness, M.B. & Sawyer, E.W., 2008: On the pseudomorphing of melt-filled pores during the crystallization of migmatite. *Journal of Petrology 49*, 1343-1363. doi: 10.1093/petrology/egn028

Hubbard, F.H., 1975: The Precambrian crystalline complex of southwestern Sweden. The geology and petrogenetic development of the Varberg Region. *Geologiska Föreningen i Stockholm Förhandlingar 97*, 223-236.

Hubbard, F.H., 1989: The geochemistry of Proterozoic lower-crustal depletion in southwest Sweden. *Lithos 23*, 101-113.

Högdahl, K., Andersson, U.B. & Eklund, O. (eds.), Andersson, U.B., Högdahl, K., Gorbatschev, R., Nyström, J.-O., Wikström, A., Sjöström, H., Bergman, S., Ahl, M., Mansfield, J., Wahlgren C.-H., Stephens, M.B., Claeson, D.T., Eklund, O., Lundqvist, T., Öhlander, B., Smeds, S.-A., Sundblad, K., 2004: *The Transscandinavian Igneous Belt (TIB) in Sweden: a review of its character and evolution*. Geological Survey of Finland, Special Paper 37, Espoo, 123 pp.

Johansson, L. & Kullerud, L., 1993: Late Sveconorwegian metamorphism and deformation in southwestern Sweden. *Precambrian Research 64*, 347-360.

Johansson, L., Lindh, A. & Möller, C., 1991: Late Sveconorwegian (Grenville) high-pressure granulite facies metamorphism in southwest Sweden. *Precambrian Research 9*, 283-292.

Johansson, Å., 2009: Baltica, Amazonia and the SAMBA connection – 1000 million years of neighbourhood during the Proterozoic?. *Precambrian Research 175*, 221-234. doi: 10.1016/j.precamres.2009.09.011

Johnson, T.E., Fischer, S. & White, R.W., 2013: Field and petrographic evidence for partial melting of TTG gneisses from the central region of the mainland Lewisian complex, NW Scotland. *Journal of Geological Society, London, 170*, 319-326. doi: 10.1144/jgs2012-096

Johnson, T.E., Fischer, S., White, R.W., Brown, M. & Rollinson H.R., 2012: Archaean intracrustal differentiation from partial melting of metagabbro: Field and geochemical evidence from the Central Region of the Lewisian Complex, NW Scotland. *Journal of Petrology 53*, 2115-2138. doi: 10.1093/petrology/egs046

Johnston, T.E. & White, R.W., 2011: Phase equilibrium constraints on conditions of granulite-facies metamorphism at Scourie, NW Scotland. *Journal of the Geological Society 168*, 147-158. doi: 10.1144/0016-76492010-069

Kretz, R., 1983: Symbols for rock-forming minerals. *American Mineralogist 68*, 277-279.

Larson, S.Å., Stigh, J. & Tullborg, E.L., 1986: The deformation history of the Eastern part of the southwest Swedish gneiss belt. *Precambrian Research 31*, 237-257.

Leake, B.E., Woolley, A.R., Arps, C.E.S., Birch, W.D., Gilbert, M.C., Grice, J.D., Hawthorne, F.C., Kato, A., Kisch, H.J., Krivovichev, V.G. Linthout, K., Laird, J., Mandarino, J.A., Maresch, W.V., Rock, N.M.S., Schumacher, J.C., Smith, D.C., Stephenson, N.C.N., Ungaretti, L., Whittaker, E.J.W. & Youzhi, G., 1997: Nomenclature of amphiboles: Report of the subcommittee on amphiboles of the international mineralogical association, commission on new minerals and mineral names. *The Canadian Mineralogist 35*, 219-246.

Li, Z.X., Bogdanova, S.V., Collins, A.S., Davidson, A., De Waele, B., Ernst, R.E., Fitzsimmons, I.C.W., Fuck, R.A., Gladkochub, D.P., Jacobs, J., Karlstrom, K.E., Lu, S., Natapov, L.M., Pease, V., Pisarevsky, S.A., Thrane, K. & Vernikovsky, V., 2008: Assembly, configuration, and break-up history of Rodinia: A synthesis. *Precambrian Research 160*, 179-210. doi: 10.1016/j.precamres.2007.04.021

Lisle, R.J., 2013: Shear zone deformation determined from sigmoidal tension gashes. *Journal of Structural Geology 50*, 35-43. doi: 10.1016/j.jsg.2012.08.002

Lundqvist, I., 2008: Berggrundskartan 5B Varberg NO, skala 1:50000. *Sveriges geologiska undersökning* K 105.

Marshak S. & Mitra, G., 1988: *Basic methods of structural geology*. Prentice-Hall Publishers, Englewood Cliffs, New Jersey, 448 pp.

Morimoto, N., Fabries, J., Ferguson, A.K., Ginzburg, I.V., Ross, M., Seifert, F.A., Zussman, J., Aoki, K. & Gottardi, G., 1988: Nomenclature of pyroxenes. *American Mineralogist 73*, 1123-1133.

Musumeci, G., 2002: Sillimanite-bearing shear zones in syntectonic leucogranite: fluid-assisted brittle–ductile deformation under amphibolite facies conditions. *Journal of Stuctural Geology 24*, 1491-1505. doi: 10.1016/S0191-8141(01)00153-5

Möller, C., 1998: Decompressed eclogites in the Sveconorwegian (–Grenvillian) orogen of SW Sweden: petrology and tectonic implications. *Journal of metamorphic Geology 16*, 641-656.

Möller, C., 1999: Sapphirine in SW Sweden: a record of Sveconorwegian (-Grenvillian) late-orogenic tectonic exhumation. *Journal of Metamorphic Geology 17*, 127-141.

Möller, C., Andersson, J., Dyck, B. & Lundin, I.A., 2013: An eclogite exhumation channel in the Sveconorwegian orogen. *In*: EGU General Assembly 2013, April 7-12, 2013 in Vienna, Austria. Vol. 15, EGU2013-6409

Möller, C., Andersson, J., Lundqvist, I. & Hellström, F.A., 2007: Linking deformation, migmatitic formation and zircon U-Pb geochronology in polymetamorphic gneisses, Sveconorwegian province, Sweden. *Journal of Metamorphic Geology 25*, 727-750. doi: 10.1111/j.1525-1314.2007.00726.x

Möller, C., Andersson, J., Söderlund, U. & Johansson, L., 1997: A Sveconorwegian deformation zone (system?) within the Eastern Segment, Sveconorwegian orogen of SW Sweden - a first report. *GFF 119*, 73-78.

Möller, C. & Söderlund, U., 1997: Age constraints on the regional deformation within the Eastern Segment, S. Sweden: Late Sveconorwegian granite dyke intrusion and metamorphic-deformational relations. *GFF 119*, 1-12.

O'Brien, P.J., Kröner, A., Jaeckel, P., Hegner, E., Zelazniewicz, A. & Krysa., R., 1997: Petrological and isotopic studies on Palaeozoic high-pressure granulites, Góry Sowie Mts, Polish Sudetes. *Journal of Petrology 38*, 433-456.

O'Brien, P.J. & Rötzler, J., 2003: High-pressure granulites: formation, recovery of peak conditions and implications for tectonics. *Journal of Metamorphic Geology 21*, 3-20. doi: 10.1046/j.1525-1314.2003.00420.x

Page, L.M., Möller, C. & Johansson, L., 1996: $^{40}Ar/^{39}Ar$ geochronology across the Mylonite Zone and the Southwestern Granulite Province in the Sveconorwegian Orogen of S Sweden. *Precambrian Research 79*, 239-259.

Passchier, C.W. & Trouw, R.A.J., 2005: *Microtectonics*. Springer, Heidelberg, 153pp.

Pattison, D.R.M., 2003: Petrogenetic significance of orthopyroxene-free garnet + clinopyroxene + plagioclase ± quartz-bearing metabasites with respect to the amphibolite and granulite facies. *Journal of Metamorphic Geology 21*, 21-34. doi: 10.1046/j.1525-1314.2003.00415.x

Pesonen, L.J., Elming, S.-Å., Mertanen, S., Pisarevsky, S., D'Agrella-Filho, M.S., Meert, J.G., Schmidt, P.W., Abrahamsen, N. & Bylund, G., 2003: Palaeomagnetic configuration of continents during the Proterozoic. *Technophysics 375*, 289-324. doi: 10.1016/S0040-1951(03)00343-3

Piazolo, S. & Passchier C. W., 2002: Controls on lineation development in low to medium grade shear zones: a study from the Cap de Creus peninsula, NE Spain. *Journal of Structural Geology 24*, 25-44. doi: 10.1016/S0191-8141(01)00045-1

Ramberg, H., 1955: Natural and experimental boudinage and pinch-and-swell structures. *The Journal of Geology 63*, 512-526.

Ramsay, J.G., 1967: *Folding and fracturing of Rocks*. McGraw-Hill Book Co., New York, 568 pp.

Savage, D. & Sills, J.D., 1980: High pressure metamorphism in the Scourian of NW Scotland: Evidence from garnet granulites. *Contributions to Mineralogy and Petrology 74*, 153-163.

Sawyer, E.W., 2001: Melt segregation in the continental crust: distribution and movement of melt in anatectic rocks. *Journal of Metamorphic geology 19*, 291-309.

Sawyer, E.W., 2008: Atlas of Migmatites. *Canadian Mineralogist*, Special Publication 9, 371 pp.

Sawyer, E.W., Cesare, B. & Brown, M., 2011: When the continental crust melts. *Elements 7*, 229-234. doi: 10.2113/gselements.7.4.229

Schwandt, C.S., Cygan, R.T. & Westrich, H.R., 1996: Ca self-diffusion in grossular garnet. *American Mineralogist 81*, 448-451.

Searle, M.P. & Alsop, G.I. 2007: Eye-to-eye with a mega sheath fold: A case study from Wadi Mayh, northern Oman Mountains. *Geology 35*, 1043-1046. doi: 10.1130/G23884A.1

Spear, F. S., 1993. M*etamorphic phase equilibria and pressure-temperature-time paths*, 799 pp. Mineralogical Society of America Monograph. Washington.

Söderlund, U., Jarl, L.-G., Persson, P.-O., Stephens, M.B. & Wahlgren,

C.-H., 1999: Protolith ages and timing of deformation in the eastern, marginal part of the Sveconorwegian orogen, southwestern Sweden. *Precambrian Research 94*, 29-48.

Söderlund, U., Möller, C., Andersson, J., Johansson, L. & Whitehouse, M., 2002: Zircon geochronology in polymetamorphic gneisses in the Sveconorwegian orogen: ion microprobe evidence for 1.46-1.42 and 0.98-0.96 Ga reworking. *Precambrian Research 113*, 193-225.

Söderlund, U., Isachen, C.E., Bylund, G., Heaman, L.M., Patchett, P.J., Vervoot, J.D. & Andersson U.B., 2005: U-Pb baddeleyite ages and Hf, Nd isotope chemistry constraining repeated mafic magnetism in the Fennoscandian Shield from 1.6 to 0.9 Ga. *Contrabutions to Mineral Petrology 150*, 174-194. doi: 10.1007/s00410-005-0011-1

Söderlund, U., Karlsson, C., Johansson, L. & Larsson, K., 2008: The Kullaberg peninsula – a glimpse of the Proterozoic evolution of SW Fennoscandia. *GFF 130*, 1-10. doi: 10.1080/11035890801301001

Tohver, E., van der Pluijm, B.A., Van der Voo, R., Rizzotto, G. & Scandolara, J.E., 2002: Paleogeography of the Amazon craton at 1.2 Ga: early Grenvillian collision with the Llano segment of Laurentia. *Earth and Planetary Science Letters 199*, 185-200. doi: 10.1016/S0012-821X(02)00561-7

Tual, L., Möller, C. & Pinan-Llamas, A., 2013: Deformation and metamorphism in an eclogite-bearing shear zone within the Sveconorwegian Orogen, Sweden. *In EGU General Assembly 2013*, April 7-12, 2013 in Vienna, Austria. Vol. 15, EGU2013-5725

Vernon, R.H., 1987: Growth and concentration of fibrous sillimanite related to heterogeneous deformation in K-feldspar-sillimanite metapelites. *Journal of Metamorphic Geology 5*, 51-68.

Vielzeuf, D., Baronnet, A., Perchuk, A.L., Laporte, D. & Baker, M.B., 2007: Calcium diffusivity in alumino-silicate garnets: an experimental and ATEM study. *Contributions to Mineralogy and Petrology 154*, 157-170. 10.1007/s00410-007-0184-x

Vigneresse, J.L. & Tikoff, T., 1999: Strain partitioning during partial melting and crystallizing felsic magmas. *Technophysics 312*, 117-132.

Viola, G., Henderson, I.H.C., Bingen, B. & Hendriks, B.W.H., 2011: The Grenvillian-Sveconorwegian orogeny in Fennoscandia: Back-thrusting and extensional shear along the "Mylonite Zone". *Precambrian Research 189*, 368-388. doi:10.1016/j.precamres.2011.06.005

Viola, G. & Mancktelow, N.S., 2005: From XY tracking to buckling: axial plane cleavage fanning and folding during progressive deformation. *Journal of Structural Geology 27*, 409-417. doi: 10.1016/j.jsg.2004.10.011

Wahlgren, C.-H., Cruden, A.R. & Stephens, M.B., 1994: Kinematics of a major fan-like structure in the eastern part of the Sveconorwegian orogen, Baltic Shield, south-central Sweden. *Precambrian Research 70*, 67-91.

Wang, X.-D. & Lindh, A., 1996: Temperature-pressure investigation of the southern part of the Southwest Swedish Granulite Region. *European Journal of Mineralogy 8*, 51-67.

Wintsch, R.P. & Andrew, M.S. 1988: Deformation induced growth of sillimanite: "Stress" minerals revisited. *Journal of Geology 96*, 143-161.

Wolf, M.B. & Wyllie, P.J., 1991: Dehydration-melting of solid amphibolite at 10 kbar: Textural development, liquid inter-connectivity and applications to the segregation of magmas. *Mineralogy and Petrology 44*, 151-179.

Wolf, M.B. & Wyllie, P.J., 1994: Dehydration-melting of amphibolite at 10 kbar: the effects of temperature and time. *Contributions to Mineralogy and Petrology 115*, 369-383.

Appendix

Table A1. Localities referred to in the text

location	coordinates		lithology with key features	thin section
	SWEREF 99 TM	WGS84		
0001	N6337914 / E0344243	N57°09.479' / E012°25.483'	folded garnet-poor amphibolite	x
0002	N6337882 / E0344431	N57°09.466' / E012°25.672'	garnet-poor amphibolite	x
0005	N6337911 / E0344320	N57°09.479' / E012°25.560'	quartz-feldspar gneiss with folded pegmatite veins	
0007	N6337730 / E0344423	N57°09.383' / E012°25.669'	quartz-feldspar gneiss	
0012	N6337690 / E0344387	N57°09.361' / E012°25.635'	quartz-feldspar gneiss	
0019	N6337916 / E0344431	N57°09.484' / E012°25.670'	garnet-poor amphibolite with large Cpx & Hbl porphyroblast	x
0026A	N6338306 / E0344593	N57°09.751' / E012°25.816'	quartz-feldspar gneiss with large garnet porphyroblasts	x
0026B	N6338430 / E0344647	N57°09.752' / E012°25.873'	migmatized garnet amphibolite	x
0029	N6338693 / E0344802	N57°09.914' / E012°26.013'	garnet amphibolite with corona or mantle texture	
0031	N6338403 / E0344570	N57°09.749' / E012°25.787'	sillimanite-bearing quartz-feldspar gneiss	
0032	N6338443 / E0344591	N57°09.771' / E012°25.809'	sillimanite-bearing quartz-feldspar gneiss	x
0033B	N6338270 / E0344765	N57°09.681' / E012°25.988'	migmatized garnet amphibolite	x
0046	N6338930 / E0343631	N57°10.014' / E012°24.839'	mafic dykes in charnockitic orthogneiss	x
0047	N6338896 / E0343714	N57°09.998' / E012°24.922'	charnockitic orthogneiss	x
0048B	N6338826 / E0343801	N57°09.961' / E012°25.012'	quartz-feldspar gneiss	x
0049B	N6338871 / E0343971	N57°09.988' / E012°25.180'	mafic dykes crosscutting a quartz-feldspar gneiss	
0050	N6338053 / E0344262	N57°09.557' / E012°25.502'	sillimanite-bearing quartz-feldspar gneiss	x
0050C	N6338097 / E0344293	N57°09.579' / N012°25.527'	folded quartz-feldspar gneiss	
0054E	N6337993 / E0344180	N57°09.570' / E012°25.511'	sillimanite-bearing quartz-feldspar gneiss	x
0062A	N6338090 / E0343517	N57°09.559' / E012°24.757'	quartz-feldspar gneiss crosscut by aplite dikes	x
0068C	N6337604 / E0343817	N57°09.304' / E012°25.073'	garnet-poor amphibolite	
0074	N6337228 / E0343674	N57°09.098' / E012°24.946'	isoclinal folded pegmatites in a quartz-feldspar gneiss	
0076	N6337212 / E0343532	N57°09.087' / E012°24.806'	chevron folded pegmatite in a quartz-feldspar gneiss	
0077A	N6337249 / E0343488	N57°09.106' / E012°24.761'	folded pegmatite in a quartz-feldspar gneiss	x
0077C	N6337223 / E0343449	N57°09.091' / E012°24.723'	calc-silicate lens	x
0080	N6337086 / E0344635	N57°09.041 / E012°25.904'	protomylonitic pegmatite in a quartz-feldspar gneiss	x
0081G	N6336631 / E0344764	N57°08.798' / E012°26.048'	δ porphyroclast in a quartz-feldspar gneiss	
0082B	N6336607 / E0344798	N57°08.787' / E012°26.083'	isoclinal folded quartz-feldspar gneiss	
0086A	N6338105 / E0344961	N57°09. 599' / E012°26.188'	sillimanite-bearing quartz-feldspar gneiss	x
0086B	N6338138 / E0344968	N57°09.614' / E012°26.195'	quartz-feldspar gneiss with large garnet porphyroblasts	x
0095B	N6338205 / E0344673	N57°09.645' / E012°25.899'	garnet amphibolite with parallel trending leucocratic veinlets	
0098A	N6338129 / E0344612	N57°09.602' / E012°25.842'	mylonitized quartz-feldspar gneiss	
0099A	N6338106 / E0344597	N57°09.587' / E012°25.828'	isoclinal folded quartz-feldspar gneiss	
0100	N6338442 / E0344589	N57°09.770' / E012°25.814'	subvertical quartz-feldspar gneiss	
0103	N6337340 / E0344622	N57°09.178' / E012°25.881'	migmatized garnet amphibolite	x
0105	N6336975 / E0344698	N57°08.983' / E012°25.970'	folded garnet-poor amphibolite	
0107	N6338214 / E0343345	N57°09.622' / E012°24.583'	migmatized garnet amphibolite	x
Q03	N6338633 / E0342375	N57°09.908' / E012°23.492'	mylonitized quartz-feldspar gneiss	x

Table A2. Representative analyses of SM12-0019 --- garnet-poor amphibolite

		clinopyroxene				amphibole		plagioclase			
		Core	Core	Core	Core	Core	Core	Core	Core	Core	Core
Compound weight %	SiO_2	51.13	51.18	52.12	53.00	42.66	41.15	58.99	58.49	61.03	59.71
	TiO_2	-	-	-	-	0.51	0.55	-	-	-	-
	Al_2O_3	4.18	4.18	2.97	1.57	11.94	11.80	24.92	25.38	25.47	25.00
	Cr_2O_3	-	-	-	-	-	-	-	-	-	-
	FeO	7.97	8.00	6.91	6.74	13.84	13.46	-	-	-	-
	MnO	-	0.66	0.81	0.84	-	0.71	-	-	-	-
	MgO	12.42	12.47	13.88	14.12	13.36	13.53	-	-	-	-
	CaO	22.77	22.52	22.95	22.75	11.39	11.43	6.84	7.59	7.18	6.64
	Na_2O	1.54	1.51	1.12	1.35	1.55	1.53	7.77	7.77	7.95	7.99
	K_2O	-	-	-	-	1.40	1.40	-	-	-	-
	Li_2O	-	-	-	-	-	-	-	-	-	-
	H_2O	-	-	-	-	2.04	2.02	-	-	-	-
	Total	100.28	100.52	100.76	100.37	99.62	98.69	98.52	99.23	101.63	99.34
cations (corrected)	Si	1.877	1.878	1.903	1.941	6.259	6.114	2.668	2.636	2.675	2.676
	Ti	-	-	-	-	0.056	0.061	-	-	-	-
	Al	0.193	0.181	0.128	0.068	^{iv}1.741 ^{vi}0.324	^{iv}1.886 ^{vi}0.180	1.328	1.348	1.316	1.321
	Cr	-	-	-	-	-	-	-	-	-	-
	Fe^{3+}	0.162	0.170	0.145	0.147	1.021	1.238	-	-	-	-
	Fe^{2+}	0.082	0.075	0.066	0.060	0.677	0.424	-	-	-	-
	Mn	-	0.021	0.025	0.026	-	0.089	-	-	-	-
	Mg	0.680	0.682	0.756	0.771	2.922	2.997	-	-	-	-
	Ca	0.896	0.885	0.898	0.893	1.790	1.819	0.331	0.367	0.337	0.319
	Na	0.110	0.107	0.079	0.096	0.441	0.441	0.681	0.679	0.676	0.694
	K	-	-	-	-	0.242	0.265	-	-	-	-
	Li *	-	-	-	-	-	-	-	-	-	-
	X_{Fe} †	0.108	0.099	0.080	0.072	0.188	0.127				
								symplectite		leucosome	
		Jd_6	Jd_6	Jd_4	Jd_3			Or_0	Or_0	Or_0	Or_0
		En_{41}	En_{42}	En_{44}	En_{45}			Ab_{67}	Ab_{65}	Ab_{67}	Ab_{69}
		Fs_5	Fs_5	Fs_4	Fs_4			An_{33}	An_{35}	An_{33}	An_{31}
		Wo_{54}	Wo_{53}	Wo_{52}	Wo_{51}						
		diopside				calcic-amphibole		andesine			

Stoichiometry is calculated on the basis of 6 oxygens for clinopyroxene, 23 for amphiboles, and 8 for plagioclase.

Table A3. Representative analyses of SM12-0026B-1 --- garnet amphibolite

		garnet				clinopyroxene		orthopyroxene		plagioclase				amphibole				biotite	
Compound weight %		Core	Rim	Core	Rim	Core	Core	Core	Core	Core	Rim	Core	Core	Core	Rim	Core	Core	Core	Core
	SiO_2	40.11	39.17	39.01	38.56	50.75	49.68	50.75	50.67	66.55	62.69	60.08	59.49	43.32	42.20	40.59	46.51	39.49	38.06
	TiO_2	-	-	-	-	-	0.40	-	-	-	-	-	-	2.41	2.42	2.16	0.49	2.45	5.89
	Al_2O_3	22.04	21.67	21.90	21.57	2.22	3.68	1.29	1.23	23.12	24.49	24.63	25.17	11.97	12.87	13.06	6.00	11.77	15.53
	Cr_2O_3	-	-	-	-	-	-	-	-	-	-	-	-	-	-	-	-	-	-
	FeO	22.39	25.17	24.29	26.50	9.60	9.73	24.68	25.80	-	-	-	-	15.42	14.77	13.91	9.23	14.59	12.12
	MnO	-	0.83	0.63	0.84	-	-	-	-	-	-	-	-	-	-	-	-	-	-
	MgO	6.06	6.35	6.33	6.26	13.59	12.26	20.59	20.04	-	-	-	-	11.64	11.02	11.81	11.36	11.03	13.95
	CaO	10.39	6.69	8.18	6.48	21.52	21.40	0.42	0.48	3.26	4.93	5.50	6.49	11.46	11.58	10.90	18.28	10.91	-
	Na_2O	-	-	-	-	0.70	1.17	-	-	10.89	9.59	9.10	8.38	2.12	2.19	2.51	1.34	1.83	0.34
	K_2O	-	-	-	-	-	-	-	-	0.72	0.53	0.51	0.62	1.34	1.59	1.35	-	1.60	8.45
	Li_2O	-	-	-	-	-	-	-	-	-	-	-	-	-	-	-	-	1.78	0.00
	H_2O	-	-	-	-	-	-	-	-	-	-	-	-	2.06	2.03	2.00	1.95	4.09	4.06
	Total	100.99	99.88	100.34	100.21	98.38	98.32	97.73	98.22	104.54	102.23	99.82	100.15	102.13	100.81	98.80	95.16	99.55	98.40
cations (corrected)																			
	Si	3.05	3.039	3.005	2.991	1.914	1.876	1.951	1.947	2.825	2.732	2.689	2.659	6.293	6.236	6.076	7.136	5.785	5.616
	Ti	-	-	-	-	-	0.011	-	-	-	-	-	-	0.263	0.269	0.243	0.057	0.270	0.654
	Al	1.98	1.982	1.988	1.972	0.099	0.164	0.058	0.056	1.157	1.258	1.299	1.326	^{iv} 1.707 ^{vi} 0.343	^{iv} 1.764 ^{vi} 0.478	^{iv} 1.924 ^{vi} 0.380	^{iv} 0.864 ^{vi} 0.221	^{iv} 2.032 ^{vi} 0.000	^{iv} 2.384 ^{vi} 0.317
	Cr	-	-	-	-	-	-	-	-	-	-	-	-	-	-	-	-	-	-
	Fe^{3+}	0.000	0.000	0.003	0.046	0.125	0.147	0.040	0.050	-	-	-	-	0.425	0.154	0.575	0.000	0.0789	0.066
	Fe^{2+}	1.421	1.629	1.562	1.673	0.178	0.160	0.754	0.779	-	-	-	-	1.448	1.672	1.166	1.184	1.751	1.434
	Mn	-	0.055	0.041	0.055	-	-	-	-	-	-	-	-	-	-	-	-	-	-
	Mg	0.688	0.735	0.727	0.724	0.768	0.690	1.180	1.148	-	-	-	-	2.521	2.428	2.635	2.598	2.409	3.069
	Ca	0.848	0.556	0.675	0.539	0.870	0.866	0.017	0.020	0.148	0.230	0.264	0.311	1.784	1.833	1.748	3.005	1.712	-
	Na	-	-	-	-	0.051	0.086	-	-	0.896	0.810	0.790	0.726	0.597	0.628	0.728	0.399	0.520	0.097
	K	-	-	-	-	-	-	-	-	0.039	0.029	0.029	0.035	0.248	0.300	0.258	-	0.299	1.590
	Li *	-	-	-	-	-	-	-	-	-	-	-		-	-	-	-	1.050	0.000
	X_{Fe} †	0.688	0.698	0.682	0.698	0.189	0.188	0.390	0.404	-	-	-	-	0.365	0.408	0.307	0.313	0.419	0.318
		zoned		unzoned		relict cpx		inside relict cpx		leucosome		symplectite							
						Jd_2	Jd_5	Jd_0	Jd_0										
		Alm_{48}	Alm_{56}	Alm_{52}	Alm_{56}	En_{42}	En_{40}	En_{61}	En_{59}	Or_3	Or_2	Or_3	Or_3						
		Sps_0	Sps_2	Sps_2	Sps_2	Fs_{10}	Fs_9	Fs_{39}	Fs_{40}	Ab_{83}	Ab_{76}	Ab_{73}	Ab_{68}						
		Prp_{23}	Prp_{24}	Prp_{24}	Prp_{24}	Wo_{48}	Wo_{51}	Wo_0	Wo_1	An_{14}	An_{22}	An_{24}	An_{29}						
v		Grs_{29}	Grs_{18}	Grs_{22}	Grs_{18}	diopside		enstatite		oligoclase				calcic-amphibole					

* see Tindle & Webb (1990) for the parameters pertaining to the Li_2O calculations

† $X_{Fe} = Fe^{2+}/[Fe^{2+} + Mg]$

Alm = $Fe^{2+}/[Fe^{2+} + Mg + Ca + Mn]$; Sps = $Mn/[Mn + Fe^{2+} + Mg + Ca]$; Pyp = $Mg/[Mg + Fe^{2+} + Ca + Mn]$; Grs = $Ca/[Ca + Fe^{2+} + Mg + Mn]$

Or = $K/[K + Na + Ca]$; Ab = $Na/[Na + K + Ca]$; An = $Ca/[Ca + K + Na]$

Stoichiometry is calculated on the basis of 12 oxygens for garnet, 6 for clinopyroxene and for orthopyroxene, 8 for plagioclase, 23 for amphibole, and 22 for biotite.

Table A4. Representative analyses of SM12-0032-1 --- sillimanite-bearing quartz-feldspar gneiss

		garnet				biotite		K-feldspar		plagioclase			monazite‡	
		Core	Core	Core	Rim	Core	Core	Core	Core	Core	Core		Core	Core
compound weight %	SiO_2	37.02	37.14	37.51	38.43	37.52	36.85	64.91	64.37	63.22	61.51	P_2O_5	30.06	29.58
	TiO_2	-	-	-	-	3.47	5.47	-	-	-	-	SiO_2	-	-
	Al_2O_3	21.70	21.47	21.90	22.20	16.93	16.76	19.56	19.09	24.88	23.69	ThO_2	5.35	5.88
	Cr_2O_3	-	-	-	-	-	-	-	-	-	-	UO_2	-	-
	FeO	28.84	28.24	28.94	28.36	11.74	15.78	-	-	-	-	Y_2O_3	-	-
	MnO	1.48	1.20	1.40	1.42	-	-	-	-	-	-	La_2O_3	18.73	17.18
	MgO	8.06	8.88	9.00	9.27	17.26	13.59	-	-	-	-	Ce_2O_3	33.65	33.86
	CaO	1.00	1.04	1.20	1.03	-	-	-	-	5.42	4.78	Pr_2O_3	-	-
	Na_2O	-	-	-	-	-	-	1.57	1.38	9.54	9.34	Nd_2O_3	10.39	11.49
	K_2O	-	-	-	-	10.13	10.10	15.37	15.29	-	-	Sm_2O_3	0.87	-
	Li_2O*	-	-	-	-	-	-	-	-	-	-	Gd_2O_3	-	-
	H_2O	-	-	-	-	4.15	4.13	-	-	-	-	Tb_2O_3	-	-
												Dy_2O_3	-	-
												CaO	0.71	-
	Total	98.10	97.97	99.95	100.71	101.20	102.68	101.41	100.13	103.06	99.32		99.76	97.99
cations (corrected)	Si	2.931	2.929	2.902	2.944	5.423	5.353	2.955	2.967	2.727	2.748			
	Ti	-	-	-	-	0.377	0.598	-	-	-	-			
	Al	2.025	1.996	1.997	2.004	^{iv}2.577 ^{vi}0.308	^{iv}2.647 ^{vi}0.222	1.050	1.037	1.265	1.247			
	Cr	-	-	-	-	-	-	-	-	-	-			
	Fe^{3+}	0.114	0.146	0.200	0.108	0.010	0.013	-	-	-	-			
	Fe^{2+}	1.795	1.717	1.673	1.709	1.409	1.904	-	-	-	-			
	Mn	0.099	0.080	0.092	0.092	-	-	-	-	-	-			
	Mg	0.951	1.044	1.038	1.059	3.719	2.943	-	-	-	-			
	Ca	0.085	0.088	0.099	0.085	-	-	-	-	0.250	0.229			
	Na	-	-	-	-	-	-	0.139	0.123	0.798	0.809			
	K	-	-	-	-	1.868	1.871	0.893	0.899	-	-			
	Li*	-	-	-	-	-	-	-	-	-	-			
	X_{Fe}	0.654	0.622	0.612	0.617	0.276	0.394							
				unzoned										
		Alm_{61}	Alm_{59}	Alm_{57}	Alm_{58}			Or_{87}	Or_{88}	Or_0	Or_0			
		Sps_3	Sps_3	Sps_4	Sps_3			Ab_{13}	Ab_{12}	Ab_{76}	Ab_{78}			
		Prp_{33}	Prp_{36}	Prp_{36}	Prp_{36}			An_0	An_0	An_{24}	An_{22}			
		Grs_3	Grs_2	Grs_3	Grs_3									

‡ N.B. There are no reference samples for the REE at the Dept. of Geology at Lund University, and the detection limit of the SEM-EDS at the Dept. of Geology cannot resolve the peaks at these higher energies. This is just a tentative analysis for preliminary identification purposes.

* see Tindle & Webb (1990) for the parameters pertaining to the Li_2O calculations
† $X_{Fe} = Fe^{2+}/[Fe^{2+} + Mg]$
Alm = $Fe^{2+}/[Fe^{2+} + Mg + Ca + Mn]$; Sps = $Mn/[Mn + Fe^{2+} + Mg + Ca]$; Pyp = $Mg/[Mg + Fe^{2+} + Ca + Mn]$; Grs = $Ca/[Ca + Fe^{2+} + Mg + Mn]$
Or = $K/[K + Na + Ca]$; Ab = $Na/[Na + K + Ca]$; An = $Ca/[Ca + K + Na]$

Stoichiometry is calculated on the basis of 12 oxygens for garnet, 22 for biotite, 8 for both K-feldspar and plagioclase.

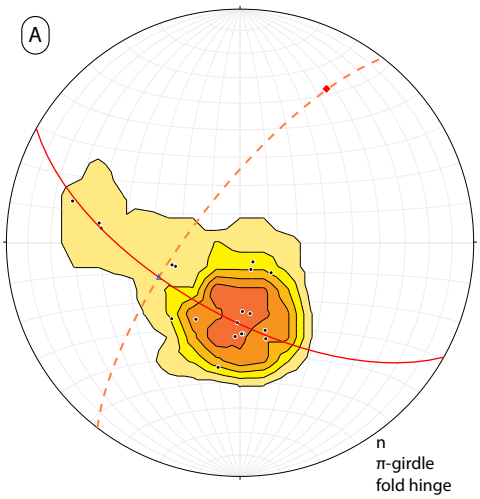

n = 19
π-girdle = 119/65
fold hinge = 25/029
interlimb angle = 97° (180-83)
axial plane = 216/74

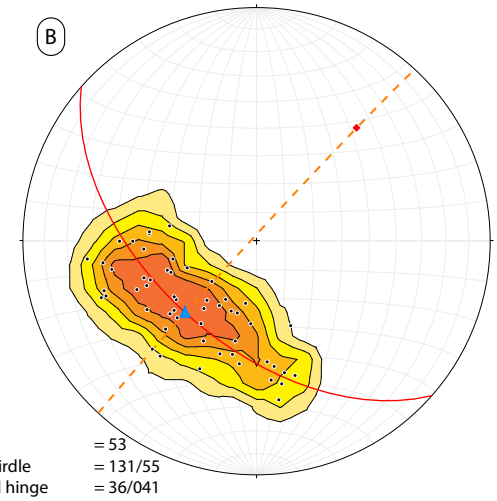

n = 53
π-girdle = 131/55
fold hinge = 36/041
interlimb angle = 105° (180-75)
axial plane = 223/88

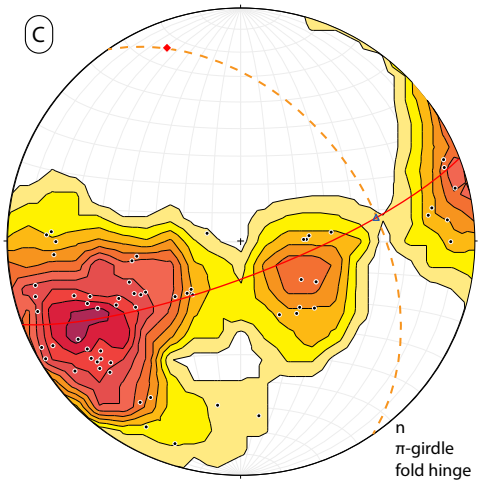

n = 63
π-girdle = 243/02
fold hinge = 88/135
axial plane = 325/43

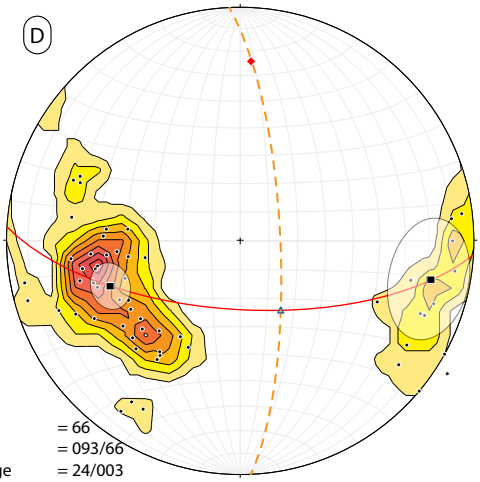

n = 66
π-girdle = 093/66
fold hinge = 24/003
interlimb angle = 66° (180-114)
axial plane = 357/76
mean vectors = 41/251
= 18/102

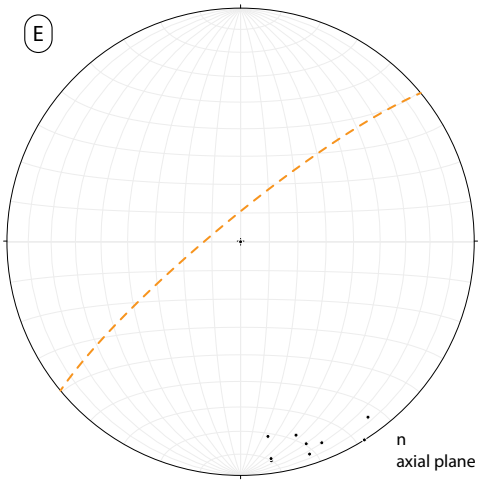

n = 9
axial plane = 230/82

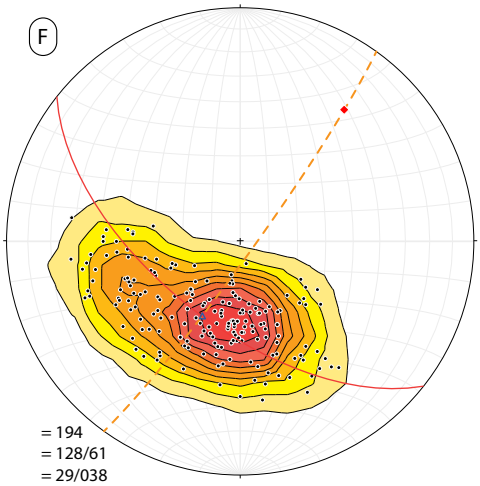

n = 194
π-girdle = 128/61
fold hinge = 29/038
interlimb angle = 95°
axial plane = 050/82

fold axis
interlimb midpoint
π-girdle
axial planar surface
mean vector

Kamb contour interval

high density — low density

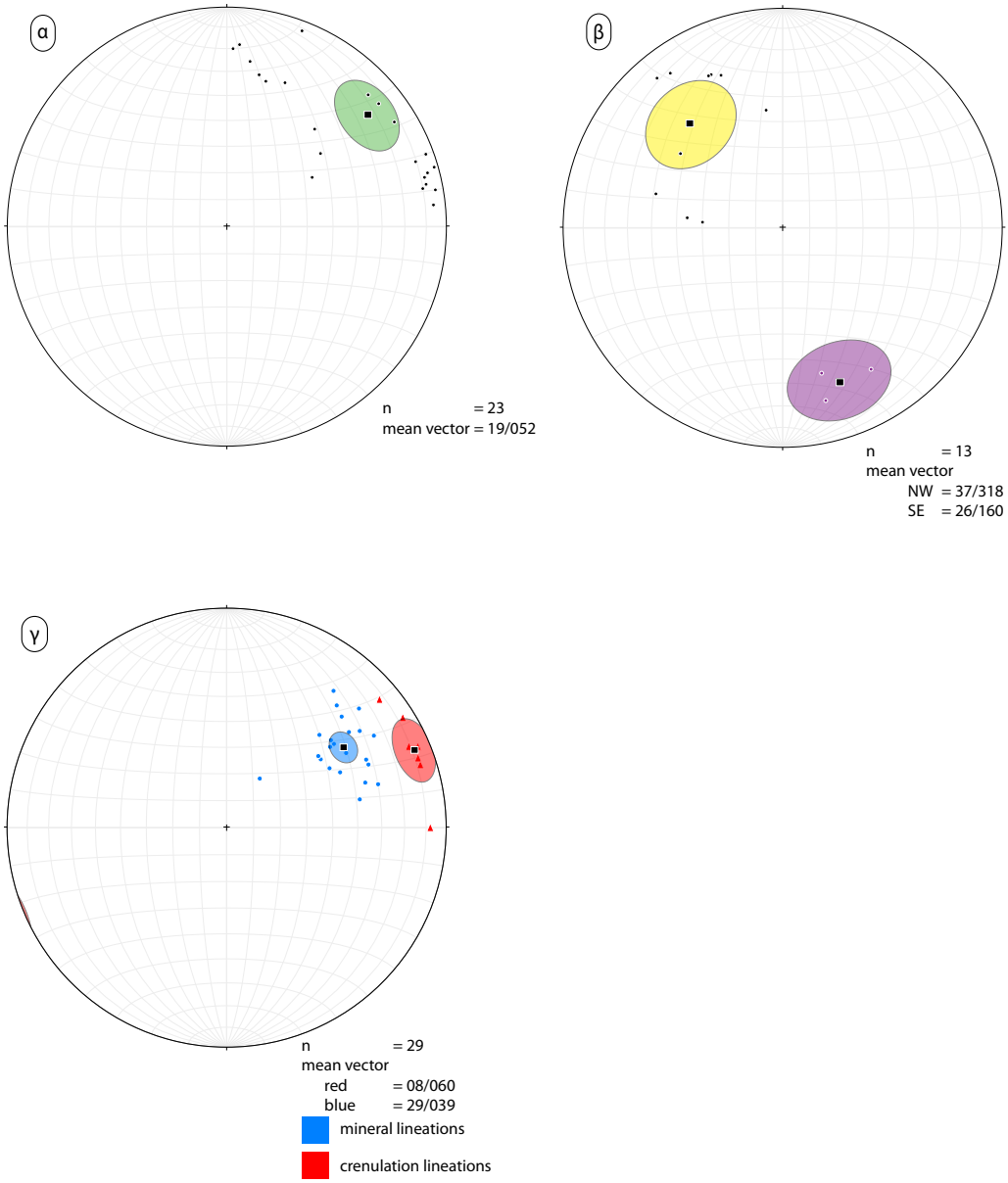

Fig. A1. Poles taken from foliation plane measurements, and lineation measurements from various localities. Data plotted onto lower hemisphere equal area stereonet using OSXStereonet. (*A*) foliation planes in Gammelgård defining the F_2 and F_3; (*B*) foliation planes in Torsgården defining the F_3; (*C*) overturned foliation planes defining the F_3; (*D*) steeply dipping foliation planes (isoclinal F_2) along the F_3 limb around Krokmossen & Svartemossen; (*E*) object lineations (aggregate & grain lineations) plotted with trace lineations (crenulation lineations defined from the axes of cuspate-lobate folds) defining the F_2 fold axis in Torsgården; (*F*) select foliation S_2 measurements throughout the study area defining the F_3 phase. Each stereonet is Kamb contoured as multiples of uniform distribution. (α) object lineations orientated parallel to the F_3 fold axis found throughout the study area, (β) object lineations orientated NW-SE found throughout the study area, and (γ) object lineations (blue) with trace lineations (axes of cuspate-lobate folds; red) around Torsgården. For further explanation on stereonets in general, the reader is directed to Marshak & Mitra (1988).

Tidigare skrifter i serien "Examensarbeten i Geologi vid Lunds universitet":

318. Younes, Hani, 2012: Carbon isotope chemostratigraphy of the Late Silurian Lau Event, Gotland, Sweden. (45 hp)
319. Weibull, David, 2012: Subsurface geological setting in the Skagerrak area – suitability for storage of carbon dioxide. (15 hp)
320. Petersson, Albin, 2012: Förutsättningar för geoenergi till idrottsanläggningar i Kallerstad, Linköpings kommun: En förstudie. (15 hp)
321. Axbom, Jonna, 2012: Klimatets och människans inverkan på tallens etablering på sydsvenska mossar under de senaste århundradena – en dendrokronologisk och torvstratigrafisk analys av tre småländska mossar. (15 hp)
322. Kumar, Pardeep, 2012: Palynological investigation of coal-bearing deposits of the Thar Coal Field Sindh, Pakistan. (45 hp)
323. Gabrielsson, Johan, 2012: Havsisen i arktiska bassängen – nutid och framtid i ett globalt uppvärmningsperspektiv. (15 hp)
324. Lundgren, Linda, 2012: Variation in rock quality between metamorphic domains in the lower levels of the Eastern Segment, Sveconorwegian Province. (45 hp)
325. Härling, Jesper, 2012: The fossil wonders of the Silurian Eramosa Lagerstätte of Canada: the jawed polychaete faunas. (15 hp)
326. Qvarnström, Martin, 2012: An interpretation of oncoid mass-occurrence during the Late Silurian Lau Event, Gotland, Sweden. (15 hp)
327. Ulmius, Jan, 2013: P-T evolution of paragneisses and amphibolites from Romeleåsen, Scania, southernmost Sweden. (45 hp)
328. Hultin Eriksson, Elin, 2013: Resistivitets-mätningar för avgränsning av lak-vattenplym från Kejsarkullens deponis infiltrationsområde. (15 hp)
329. Mozafari Amiri, Nasim, 2013: Field relations, petrography and 40Ar/39Ar cooling ages of hornblende in a part of the eclogite-bearing domain, Sveconorwegian Orogen. (45 hp)
330. Saeed, Muhammad, 2013: Sedimentology and palynofacies analysis of Jurassic rocks Eriksdal, Skåne, Sweden. (45 hp)
331. Khan, Mansoor, 2013: Relation between sediment flux variation and land use patterns along the Swedish Baltic Sea coast. (45 hp)
332. Bernhardson, Martin, 2013: Ice advance-retreat sediment successions along the Logata River, Taymyr Peninsula, Arctic Siberia. (45 hp)
333. Shrestha, Rajendra, 2013: Optically Stimulated Luminescence (OSL) dating of aeolian sediments of Skåne, south Sweden. (45 hp)
334. Fullerton, Wayne, 2013: The Kalgoorlie Gold: A review of factors of formation for a giant gold deposit. (15 hp)
335. Hansson, Anton, 2013: A dendroclimatic study at Store Mosse, South Sweden – climatic and hydrologic impacts on recent Scots Pine (*Pinus sylvestris*) growth dynamics. (45 hp)
336. Nilsson, Lawrence, 2013: The alteration mineralogy of Svartliden, Sweden. (30 hp)
337. Bou-Rabee, Donna, 2013: Investigations of a stalactite from Al Hota cave in Oman and its implications for palaeoclimatic reconstructions. (45 hp)
338. Florén, Sara, 2013: Geologisk guide till Söderåsen – 17 geologiskt intressanta platser att besöka. (15 hp)
339. Kullberg, Sara, 2013: Asbestkontamination av dricksvatten och associerade risker. (15 hp)
340. Kihlén, Robin, 2013: Geofysiska resistivitetsmätingar i Sjöcrona Park, Helsingborg, undersökning av områdets geologiska egenskaper samt 3D modellering i GeoScene3D. (15 hp)
341. Linders, Wictor, 2013: Geofysiska IP-undersökningar och 3D-modellering av geofysiska samt geotekniska resultat i GeoScene3D, Sjöcrona Park, Helsingborg, Sverige. (15 hp)
342. Sidenmark, Jessica, 2013: A reconnaissance study of Rävliden VHMS-deposit, northern Sweden. (15 hp)
343. Adamsson, Linda, 2013: Peat stratigraphical study of hydrological conditions at Stass Mosse, southern Sweden, and the relation to Holocene bog-pine growth. (45 hp)
344. Gunterberg, Linnéa, 2013: Oil occurrences in crystalline basement rocks, southern

Norway – comparison with deeply weathered basement rocks in southern Sweden. (15 hp)

345. Peterffy, Olof, 2013: Evidence of epibenthic microbial mats in Early Jurassic (Sinemurian) tidal deposits, Kulla Gunnarstorp, southern Sweden. (15 hp)
346. Sigeman, Hanna, 2013: Early life and its implications for astrobiology – a case study from Bitter Springs Chert, Australia. (15 hp)
347. Glommé, Alexandra, 2013: Texturella studier och analyser av baddeleyitomvandlingar i zirkon, exempel från sydöstra Ghana. (15 hp)
348. Brådenmark, Niklas, 2013: Alunskiffer på Öland – stratigrafi, utbredning, mäktigheter samt kemiska och fysikaliska egenskaper. (15 hp)
349. Jalnefur Andersson, Evelina, 2013: En MIFO fas 1-inventering av fyra potentiellt förorenade områden i Jönköpings län. (15 hp)
350. Eklöv Pettersson, Anna, 2013: Monazit i Obbhult-komplexet: en pilotstudie. (15 hp)
351. Acevedo Suez, Fernando, 2013: The reliability of the first generation infrared refractometers. (15 hp)
352. Murase, Takemi, 2013: Närkes alunskiffer – utbredning, beskaffenhet och oljeinnehåll. (15 hp)
353. Sjöstedt, Tony, 2013: Geoenergi – utvärdering baserad på ekonomiska och drifttekniska resultat av ett passivt geoenergisystem med värmeuttag ur berg i bostadsrättsföreningen Mandolinen i Lund. (15 hp)
354. Sigfúsdóttir, Thorbjörg, 2013: A sedimentological and stratigraphical study of Veiki moraine in northernmost Sweden. (45 hp)
355. Månsson, Anna, 2013: Hydrogeologisk kartering av Hultan, Sjöbo kommun. (15 hp)
356. Larsson, Emilie, 2013: Identifying the Cretaceous–Paleogene boundary in North Dakota, USA, using portable XRF. (15 hp)
357. Anagnostakis, Stavros, 2013: Upper Cretaceous coprolites from the Münster Basin (northwestern Germany) – a glimpse into the diet of extinct animals. (45 hp)
358. Olsson, Andreas, 2013: Monazite in metasediments from Stensjöstrand: A pilot study. (15 hp)
359. Westman, Malin, 2013: Betydelsen av raka borrhål för större geoenergisystem. (15 hp)
360. Åkesson, Christine, 2013: Pollen analytical and landscape reconstruction study at Lake Storsjön, southern Sweden, over the last 2000 years. (45 hp)
361. Andolfsson, Thomas, 2013: Analyses of thermal conductivity from mineral composition and analyses by use of Thermal Conductivity Scanner: A study of thermal properties in Scanian rock types. (45 hp)
362. Engström, Simon, 2013: Vad kan inneslutningar i zirkon berätta om Varbergscharnockiten, SV Sverige. (15 hp)
363. Jönsson, Ellen, 2013: Bevarat maginnehåll hos mosasaurier. (15 hp)
364. Cederberg, Julia, 2013: U-Pb baddeleyite dating of the Pará de Minas dyke swarm in the São Francisco craton (Brazil) – three generations in a single swarm. (45 hp)
365. Björk, Andreas, 2013: Mineralogisk och malmpetrografisk studie av disseminerade sulfider i rika och fattiga prover från Kleva. (15 hp)
366. Karlsson, Michelle, 2013: En MIFO fas 1-inventering av förorenade områden: Kvarnar med kvicksilverbetning Jönköpings län. (15 hp)
367. Michalchuk, Stephen P., 2013: The Säm fold structure: characterization of folding and metamorphism in a part of the eclogite-granulite region, Sveconorwegian orogen. (45 hp)

LUNDS UNIVERSITET

Geologiska institutionen
Lunds universitet
Sölvegatan 12, 223 62 Lund